



저작자표시-비영리-변경금지 2.0 대한민국

이용자는 아래의 조건을 따르는 경우에 한하여 자유롭게

- 이 저작물을 복제, 배포, 전송, 전시, 공연 및 방송할 수 있습니다.

다음과 같은 조건을 따라야 합니다:



저작자표시. 귀하는 원저작자를 표시하여야 합니다.



비영리. 귀하는 이 저작물을 영리 목적으로 이용할 수 없습니다.



변경금지. 귀하는 이 저작물을 개작, 변형 또는 가공할 수 없습니다.

- 귀하는, 이 저작물의 재이용이나 배포의 경우, 이 저작물에 적용된 이용허락조건을 명확하게 나타내어야 합니다.
- 저작권자로부터 별도의 허가를 받으면 이러한 조건들은 적용되지 않습니다.

저작권법에 따른 이용자의 권리는 위의 내용에 의하여 영향을 받지 않습니다.

이것은 [이용허락규약\(Legal Code\)](#)을 이해하기 쉽게 요약한 것입니다.

[Disclaimer](#)

공학박사학위논문

**Adjoint-Based Design Optimization
of Vortex Generator
for Three-Dimensional
Internal and External Viscous Flows**

매개변수 기반의 민감도 해석을 적용한
와류 발생 장치 최적 설계

2013 년 2 월

서울대학교 대학원

기계항공공학부

이 준 석

Adjoint-Based Design Optimization of Vortex Generator for Three-Dimensional Internal and External Viscous Flows

매개변수 기반의 민감도 해석을 적용한
와류 발생 장치 최적 설계

지도교수 김 종 암

이 논문을 공학박사학위 논문으로 제출함
2012 년 12 월

서울대학교 대학원
기계항공공학부
이 준 석

이준석의 공학박사 학위논문을 인준함
2012 년 12 월

위 원 장 : _____

부위원장 : _____

위 원 : _____

위 원 : _____

위 원 : _____

Abstract

This study focused on an adjoint-based design optimization of vortex generators for the performance improvement of an aircraft. Among the several components of the aircraft, the applications of this study included the internal flow of an S-shaped subsonic inlet (S-duct), the RAE M2129, and the external flow of a wing-body configuration, the DLR-F6. To improve these components and to validate the proposed design approach on both of internal and external flows, the vortex generators were installed inside the S-duct and on the wing upper surface. Then they were independently optimized with five design parameters per each vortex generator. For the purpose of truly optimal design, each vortex generator should be independently treated by fully reflecting local flow patterns near the vortex generators.

To increase the efficiency of flow analysis and design, the source term model of the vortex generator, the BAY model, was employed. The original BAY model did not reflect a small change in position, so it had difficulties in differentiation for sensitivity analysis of the vortex generator. The BAY model, therefore, was modified into a differentiable BAY model by taking into account a small volume change.

For the optimal design mentioned above, each vortex generators must be dealt with independently; thus, a large number of design variables were considered. Because the gradient-based design optimization using the discrete adjoint approach has an advantage in that the number of design variables is independent of the computational cost, a sensitivity analysis with respect to the design variables was performed by using the adjoint variable method including the original/differentiable BAY model.

For the RAE M2129, the design of vortex generators was performed to minimize the distortion coefficient while maintaining the baseline total pressure recovery ratio by adopting the proposed gradient-based design process that included the source term model. A total of five design cases were conducted to achieve 3 objectives; validating the proposed design approach, obtaining the optimized vortex generators, and confirming their enhanced performance. Through the proposed design process, the performance of the target inlet was remarkably improved, showing that the distortion coefficient decreases well over 70% while maintaining the total pressure recovery ratio.

For the DLR-F6 wing-body aircraft, the parametric study and the design study relating to the vortex generator were performed to increase the ratio of lift to drag by removing the junction vortex. To check the flow characteristics of the wing-

body junction and to confirm the effects of the vortex generator on the junction vortex, a total of nine parametric studies were conducted first, and a baseline configuration of design was determined based on this results. As a result of the parametric study, the lift to drag ratio of DLR-F6 increases by over 2~4% under the same flight conditions. After carrying out the optimization of the vortex generators, the junction vortex was shrunk and weakened, and the performance of the DLR-F6 improved over 5% without any additional components what can be a cause of weight increase except the vortex generators.

Keywords: Computational Fluid Dynamics, Aerodynamic Design Optimization, Adjoint Variable Method, Vortex Generator, BAY Model, RAE M2129 subsonic S-shaped offset inlet, DLR-F6 wing-body configuration.

Student number: 2006-20974

Name: Yi, JunSok

Table of Contents

Abstract	i
Table of Contents	iv
Nomenclature	ix
List of Tables	xii
List of Figures	xiii
Chapter I Introduction	1
1.1 Research Objective	1
1.2 Research Background	1
1.3 Computational Fluid Dynamics	5
1.4 Aerodynamic Design Optimization	7
1.5 Sensitivity Analysis	10
1.6 Vortex Generator and Source Term Model	12
1.7 Internal Flow Design (S-shaped Offset Inlet)	13
1.8 External Flow Design (Wing-Body Configuration)	15
Chapter II Flow Analysis	18
2.1 Governing Equations	18
2.2 Turbulence Models	20
2.2.1 The original $k-\omega$ model	20
2.2.2 The Transformed $k-\varepsilon$ Model	21
2.2.3 The Standard Menter's $k-\omega$ Shear Stress Transport (SST) Model	22
2.2.4 The Menter's $k-\omega$ SST Model from 2003 ($k-\omega$ SST- 2003)	24

2.3	Spatial Discretization	25
2.3.1	Roe’s Flux Difference Splitting.....	26
2.3.2	RoeM Scheme	28
2.3.3	Higher Order Spatial Accuracy	30
2.3.4	Compact Scheme for Viscous Fluxes.....	31
2.4	Time Integration.....	33
2.5	Parallelization of Flow Solver	35
2.6	Overset (Chimera) Grid Technique.....	35
2.6.1	Pre-process of Overset Grid Technique.....	36
2.6.2	Flow analysis with Overset Grid Technique	38
2.6.3	Post-process of Overset Grid Technique	38
2.7	Validation of Flow Solver	38
2.7.1	Case I: RAE 2822 Airfoil (Infinite Wing).....	39
2.7.2	Case II: NLR 7301 Airfoil with Flap (Infinite Wing)	43
2.7.3	Case III: DPW-W1	45
Chapter III Sensitivity Analysis		52
3.1	Finite Difference Method.....	52
3.2	Complex Step Derivative Method	52
3.3	Direct Differentiation Method	54
3.4	Discrete Adjoint Method.....	55
3.5	Overset Adjoint Boundary Condition	57
3.6	BFGS method.....	58
Chapter IV Vortex Generator		60
4.1	BAY Model	60
4.2	Differentiable BAY Model.....	62
4.3	Design Strategy Using VG Source Term Model.....	65
4.4	Sensitivity Analysis with Differentiable BAY Model.....	67

Chapter V	RAE M2129 S-Duct	71
5.1	RAE M2129 S-shape Subsonic Offset Inlet	71
5.1.1	Geometric Information.....	71
5.1.2	Performance Coefficients for Subsonic Inlet	72
5.1.3	Previous Vortex Generator Study in an S-Duct.....	73
5.2	Flow Analysis and Flow Solver Verification	74
5.2.1	Grid Topology and Boundary Condition.....	75
5.2.2	Validation of Flow Solver with the Source Term Model	76
5.3	Flow Characteristics of S-Duct.....	82
5.4	Design Approach.....	84
5.4.1	Optimization Technique, Objective Function, and Design Range	84
5.4.2	Validation of Adjoint Solver with VG Source Term Model	86
5.5	Design Cases	88
5.6	Design Results	89
5.6.1	Case 1: Design by BAY Model with Geometric Parameters	89
5.6.2	Case 2: Design by Differentiable BAY Model with Geometric Parameters	92
5.6.3	Case 3: Design by Differentiable BAY Model with Positional Parameters	94
5.6.4	Case 4: Complete Design by Differentiable BAY Model	95
5.6.5	Case 5: Additional Design from Different Initial Condition.....	102

5.7	Flow Characteristics of S-Duct with Optimized VG Configuration and Discussion.....	103
Chapter VI DLR-F6 Aircraft		106
6.1	DLR-F6 Wing-Body Configuration.....	106
6.1.1	Geometric Information.....	106
6.1.2	Performance Coefficient for Aircraft	107
6.1.3	Previous Vortex Generator Study for Aircraft.....	108
6.2	Flow Analysis of DLR-F6.....	109
6.2.1	Grid Topology and Overset Structure	110
6.2.2	Flow Analysis of DLR-F6 without VG.....	111
6.3	Flow Characteristics of DLR-F6 and Junction Vortex.....	115
6.4	Parametric Study.....	118
6.4.1	Case 1: Position, Wing Upper Surface	120
6.4.2	Case 2: Position, Body Surface	122
6.4.3	Case 3: Angle of Incidence, Wing Upper Surface.....	125
6.4.4	Case 4: Angle of Incidence, Body Surface.....	129
6.4.5	Case 5: Angle of Incidence, Body Surface, Front Side	131
6.4.6	Case 6: Position, Body Surface, Under Wing	132
6.4.7	Case 7: Coupling, Position, Wing Upper Surface	134
6.4.8	Case 8: Coupling, Position, Body Surface	137
6.4.9	Case 9: Number, Wing Upper Surface	139
6.4.10	Discussion of Parametric Study	141
6.5	Design Approach.....	142
6.6	Design Results	144
6.6.1	Design Case 1: From Wing VG.....	144
6.6.2	Design Case 2: From ‘Body VG’	148

6.7	Flow Characteristics of DLR-F6 with Optimized VG Configurations and Discussion	151
Chapter VII Concluding Remarks.....		154
7.1	Summary	154
7.2	Future Works	156
References	157
Appendix A	Parallel Algorithm.....	169
Appendix B	Verification of BAY type model	174
국문 초록	183

Nomenclature

$C_{airfoil}$	=	chord length of sectional airfoil
C_D	=	Drag coefficient
C_L	=	lift coefficient
C_M	=	moment coefficient
C_{mean}	=	mean aerodynamic chord length
C_P	=	pressure coefficient
c_{VG}	=	chord length
D	=	design variable vector $(c_{VG}, h_{VG}, \alpha_{VG}, X_{VG}, \beta_{VG})^T$
$DC\theta$	=	distortion coefficient
F	=	objective function
h_{VG}	=	blade height
k	=	turbulent kinetic energy
L/D	=	ratio lift to drag
PR	=	total pressure recovery ratio
p	=	pressure
Q	=	flow variable vector $(\rho, \rho u, \rho v, \rho w, e, k, \omega)^T$
Q_p	=	primitive variable vector $(\rho, u, v, w, p, k, \omega)^T$
R	=	residual of the governing equations

\vec{u}	=	velocity vector $(u, v, w)^T$
u	=	x -directional velocity
VG	=	vortex generator
v	=	y -directional velocity
W	=	weight
w	=	z -directional velocity
X	=	coordinates of computational mesh
X_{VG}	=	sector location or x -directional location
α	=	angle of attack
α_{VG}	=	angle of incidence
β_{VG}	=	spacing angle or y/z -directional location
θ	=	circumferential angle
Λ	=	adjoint variable
ρ	=	density
ω	=	turbulent dissipation rate

Subscripts

cl	=	centerline
E	=	energy
ef	=	engine face
i	=	cell index

in = inlet entrance
 M = momentum
t = total state value

List of Tables

Table 1	Freestream conditions for RAE 2822 airfoil.....	39
Table 2	Freestream conditions for NLR 7301 airfoil with flap.....	44
Table 3	Reference quantities for DPW-W1.....	45
Table 4	Freestream conditions for DPW-W1.....	45
Table 5	Comparison of wing performance coefficients in multi-block.....	47
Table 6	Comparison of wing performance coefficients in overset grid.....	49
Table 7	Matrix of CFD-Designed Vortex Generator Installations.	74
Table 8	High Mass Flow Rate (HMFR) Condition of RAE M2129.....	75
Table 9	Design parameters and their range.....	86
Table 10	Validation results: adjoint variable method vs. complex step method.....	87
Table 11	Design results: Distortion coefficient and total pressure recovery ratio.	105
Table 12	VG condition: Case 1.....	120
Table 13	VG condition: Case 2.....	123
Table 14	VG condition: Case 3.....	126
Table 15	VG condition: Case 4.....	129
Table 16	VG condition: Case 5.....	131
Table 17	VG condition: Case 6.....	133
Table 18	VG condition: Case 7.....	134
Table 19	VG condition: Case 8.....	137
Table 20	VG condition: Case 9.....	139
Table 21	VG configurations for optimization.....	139
Table 22	Design parameters and its range.	143

List of Figures

Figure 1	Three phase of aircraft design.....	2
Figure 2	Strategy of aerodynamic design optimization.....	8
Figure 3	Cell indexes in two-dimensional grid.	26
Figure 4	Flow analysis steps by using overset grid technique.....	36
Figure 5	Shape and grid of RAE 2822 airfoil.....	40
Figure 6	History of $L2$ norm density residual.....	41
Figure 7	Pressure contours near the airfoil.....	41
Figure 8	Pressure coefficients on the airfoil section.....	42
Figure 9	Convergence of the lift on the airfoil with iterations.	42
Figure 10	Convergence of the drag on the airfoil with iterations.....	42
Figure 11	Shape and grids of NLR 7301 airfoil with flap.....	43
Figure 12	Pressure coefficient of NLR 7301 airfoil with flap.....	44
Figure 13	Shape and surface meshes of DPW-W1.....	46
Figure 14	Pressure contour of DPW-W1 (Multi-block).	47
Figure 15	Pressure coefficient of DPW-W1 at $y/span = 42\%$ (multi-block).	48
Figure 16	Overset grid system of DPW-W1.....	49
Figure 17	Reconstructed surface meshes of DPW-W1.	50
Figure 18	Pressure contour of DPW-W1 (overset).....	50
Figure 19	Pressure coefficient of DPW-W1 at $y/span = 42\%$ (overset).	51
Figure 20	Directional definition of vortex generator.....	61
Figure 21	Volume calculation of BAY model.....	63
Figure 22	Limitation of BAY model in small positional change.....	63
Figure 23	Volume calculation of differentiable BAY model.	64
Figure 24	Virtual thickness of vortex generator for differentiable BAY	

	model.	64
Figure 25	Geometric schematic of the RAE M2129.	72
Figure 26	Overall grid distribution.	76
Figure 27	Validation of flow solver with/without BAY model (distortion coefficient).	77
Figure 28	Validation of flow solver with/without BAY model (total pressure recovery ratio).	77
Figure 29	Flow pattern of S-duct without vortex generator.	78
Figure 30	Position of VG170 configuration and flow pattern near vortex generators.	79
Figure 31	Total pressure recovery contour along S-duct without VG configuration.	79
Figure 32	Total pressure recovery contour along S-duct with VG170 configuration.	80
Figure 33	Validation of flow solver with BAY model and differentiable BAY model (distortion coefficient).	81
Figure 34	Validation of flow solver with BAY model and differentiable BAY model (total pressure recovery ratio).	81
Figure 35	Flow characteristics of S-duct without vortex generator.	82
Figure 36	Flow characteristics of S-duct with VG170 configuration.	83
Figure 37	Geometric schematic of the vortex generator installed in S- duct and related parameters.	86
Figure 38	History of objective function: Design by BAY model (first design).	89
Figure 39	Design result: Designed VG shape and angle of incidence.	90
Figure 40	Comparison of distortion patterns: First design and two sub- designs of first design.	91
Figure 41	Total pressure recovery contour along S-duct with designed	

	VG configuration (first design).....	92
Figure 42	History of objective function: Design by differentiable BAY model (second design).	93
Figure 43	Design result: Designed VG shape and angle of incidence (second design).	93
Figure 44	History of objective function: Design with positional design parameters (third design).	94
Figure 45	Design result: Location of each VG (third design).	95
Figure 46	History of objective function: Complete design.	96
Figure 47	Design result: Optimized VG shape.....	96
Figure 48	Design result: Location of optimized VG.	97
Figure 49	Design result: Optimized VG installed in S-duct (complete design).	97
Figure 50	Comparison of distortion patterns: Second design, third design, and complete design.	99
Figure 51	Total pressure recovery contour along S-duct with optimized VG configuration (complete design).....	99
Figure 52	Sensitivity information of baseline (complete design).....	101
Figure 53	Off-Design condition test.	101
Figure 54	History of objective function: Design from different initial condition (additional design).	102
Figure 55	Flow characteristics of S-duct with designed VG configuration.	103
Figure 56	Design result: Comparison of mixing flow patterns at engine face.	104
Figure 57	Geometric schematic of DLR-F6 model [83].	107
Figure 58	Grid topology of DLR-F6.	110
Figure 59	Surface grid distribution.....	111

Figure 60	Lift coefficient curve.....	112
Figure 61	Comparison of drag coefficient ($C_L=0.5$).....	113
Figure 62	Pressure contour of DLR-F6.....	113
Figure 63	Shape and size of junction vortex.	114
Figure 64	Pressure contour near the junction vortex.....	117
Figure 65	Pressure contour far from the junction vortex.....	117
Figure 66	Parameters and its ranges.....	120
Figure 67	Parametric study Case 1: Comparison of C_L and C_D	121
Figure 68	Parametric study Case 1: Comparison of C_L and L/D	121
Figure 69	Parametric study Case 1: Junction vortex and high-pressure region on the trailing edge.	122
Figure 70	Parametric study Case 2: Comparison of C_L and C_D	123
Figure 71	Parametric study Case 2: Comparison of C_L and L/D	124
Figure 72	Parametric study Case 2: Junction vortex and high-pressure region on the trailing edge.	125
Figure 73	Parametric study Case 3: Comparison of C_L and C_D	126
Figure 74	Parametric study Case 3: Comparison of C_L and L/D	127
Figure 75	Parametric study Case 3: Shape of junction vortex with negative angle VGs.	128
Figure 76	Parametric study Case 3: Shape of junction vortex with positive angle VGs.....	128
Figure 77	Parametric study Case 4: Comparison of C_L and C_D	129
Figure 78	Parametric study Case 4: Comparison of C_L and L/D	130
Figure 79	Parametric study Case 4: Flow direction.	130
Figure 80	Parametric study Case 5: Comparison of C_L and C_D	132
Figure 81	Parametric study Case 5: Comparison of C_L and L/D	132
Figure 82	Parametric study Case 6: Comparison of C_L and C_D	133
Figure 83	Parametric study Case 6: Comparison of C_L and L/D	134

Figure 84	Parametric study Case 7: Comparison of C_L and C_D	135
Figure 85	Parametric study Case 7: Comparison of C_L and L/D	136
Figure 86	Parametric study Case 7: Junction vortex and high-pressure region on the trailing edge.	136
Figure 87	Parametric study Case 8: Comparison of C_L and C_D	138
Figure 88	Parametric study Case 8: Comparison of C_L and L/D	138
Figure 89	Parametric study Case 8: Flow direction with VG of rear side.	139
Figure 90	Parametric study Case 9: Comparison of C_L and C_D	140
Figure 91	Parametric study Case 9: Comparison of C_L and C_D	140
Figure 92	History of objective function: Design from ‘Wing VG’.	145
Figure 93	Design Case 1: Designed VG and pressure contour.....	146
Figure 94	Design Case 1: Designed VG and their shapes and positions.....	146
Figure 95	Sensitivity information of baseline (Design Case 1).....	147
Figure 96	Drag polar: Design from ‘Wing VG’.	147
Figure 97	History of objective function: Design from ‘Body VG’.	149
Figure 98	Design Case 2: Designed VG and pressure contour.....	149
Figure 99	Design Case 2: Designed VG and their shapes and positions.....	150
Figure 100	Sensitivity information of baseline (Design Case 2).....	150
Figure 101	Pressure coefficient of DLR-F6 at $y/span = 15\%$	151
Figure 102	Pressure coefficient of DLR-F6 at $y/span = 23.9\%$	152
Figure 103	Small size junction vortex (Design Case 1).	153
Figure 104	Large size junction vortex (Design Case 2).	153

This page is blank

Chapter I

Introduction

1.1 Research Objective

This study focused on the design of Vortex Generator (VG) installed in an S-shaped offset inlet and on an aircraft wing-body surface. For the VG design, a new design strategy was proposed by adopting the Gradient Based Optimization Method (GBOM) and the VG source term model. The development and improvement of the efficient, robust, and accurate flow analysis code and adjoint-based sensitivity analysis code, which are the essential components of the proposed VG design, was another objective of this research.

1.2 Research Background

For decades, many researchers and engineers have tried to develop and to improve an aircraft in terms of flight distance, efficiency, speed, control, and so forth. For these objectives, they have attempted to improve an external performance of aircraft, to design internal aerodynamic parts, to develop a high-efficient muscular engine, and to invent several flow control devices and high-lift devices. Owing to these efforts, many of the recently developed aircrafts satisfied both of high efficiency and high performance.

Aircraft design processes can be classified into three major phase: conceptual design, preliminary design, and detail design, as illustrated in Fig. 1. In the conceptual design, delegates of the designer group and the sponsor of the aircraft

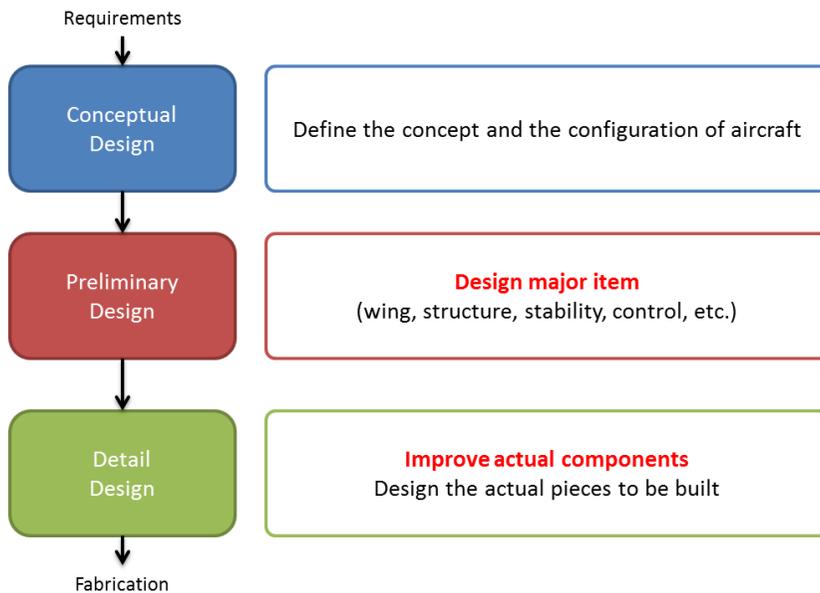


Figure 1 Three phase of aircraft design.

development project decide the configuration arrangement, size, weight, and overall performance of aircraft. In the preliminary design phase, engineers and researchers analyze and design the portion of the area of their expertise, such as aerodynamics, structures, stability, and control system. The definition of the external aerodynamic shape is actually finalized in the preliminary design because aerodynamic design plays a leading role in the aircraft design; therefore, Aerodynamic Shape Optimization (ASO) with Computational Fluid Dynamics (CFD) generally belongs to this phase. After the preliminary design, the detail design is performed in order to make the decision for entering full-scale development and to design actual pieces for fabrication of the aircraft [1, 2].

From the airfoil shape design as an early stage of aerodynamic shape design, several parts of aircraft, such as a wing planform, a turbine blade, and overall shapes of aircraft configuration are designed at the preliminary phase. In past days, these designs were generally performed by considering massive experimental data, and by depending on an engineer's experience and intuition. Since the early 1990s,

however, many researchers of aerodynamics have been interested in the application of numerical optimization techniques to these aerodynamic shape designs [2-12]. Nowadays, the extension of the optimization technique to Multi-Disciplinary Optimization (MDO) has been discussed and adopted by some engineers [13-16].

The increased computing power contributes the prosperity of the design optimization. The computational time cost, however, remains as a serious problem because the external aerodynamic shape design that consumes large computing costs has to be finished before its deadline. Because this deadline is only few months in industry, the design optimization is hard to be adopted fully for all conditions in the preliminary design phase. To overcome this limitation, researchers assumed the complex geometry as a simple one, which is quite an effective way to design an aircraft but there are some problems. The most serious problem is that the manufactured aircraft is hard to achieve the originally determined target performance because the performance of the aircraft can be easily changed when the simplified geometry re-transforms to the actual complex geometry.

Although designed components of aircraft need to be re-designed after the preliminary phase in order to obtain the target performance, the external aerodynamic shape should be fixed after the determination. This study, therefore, focused on the extra component for complementing the gaps between the actual performance and the target performance. There are many devices that can be adopted on the fixed external aerodynamic shape, and the design of these components can be shifted to the detail design phase in spite of the preliminary phase. The most popular one is a flow control device.

A flow control device is classified by two types: (1) an active flow control device which needs extra power for driving, and (2) a passive flow control device that is only installed on the surface without additional power. Because the extra power for the active flow control device is difficult to be considered in the aerodynamic optimization, a passive flow control device was chosen for this study.

The selected one was a Vortex Generator (VG). A VG improves the aerodynamic performance by suppressing the detrimental effects caused by adverse pressure gradient, boundary-layer separation, and shock-boundary-layer interaction [17]. Among the several types of VG, the thin-plate type VG was adopted and designed to improve the aircraft.

The subsonic S-shaped offset inlet, the Royal Aircraft Establishment intake Model 2129 (RAE M2129), was the first application of this study. As in the case of aircraft using the buried-type engine, the aircraft engine face is not directly connected to the freestream. Furthermore, the flow entering into the engine inlet is misaligned to the engine face because of geometric constraints, such as engine position and airframe structure. As a result, the inlet geometry is usually an S-shape, which is called the S-shaped inlet or the S-duct. The shape of S-duct is determined in the preliminary design and many previous researchers focused on the optimization of S-duct shape. Many detrimental flow characteristics, however, occurred in the designed S-duct. The key aerodynamic feature in the S-duct is the flow separation that originates from the S-shaped geometry itself. This flow separation is a major source of the non-uniformity of the incoming flow moving toward the engine face, thereby leading to the deterioration of the engine efficiency. The VGs, therefore, have been applied and optimized to deliver uniform flow to the engine face [18].

The second application is the wing-body configuration. The junction vortex that occurred on the DLR-F6 wing-body configuration is highlighted. The junction vortex, which has various names, such as a corner separation of junction, a separation bubble, and the other names, is one of the reasons for the difficulties in making accurate prediction about the aircraft performance. For this reason, the DLR-F6 wing-body geometry was augmented at the 3rd AIAA Drag Prediction Workshop (DPW-III) [19], with two types of side-of-body fairing designed by Vassberg *et al.* [20] used to decrease the complexity of the flow physics in the wing-

body junction. By adopting these fairings, the drag prediction was successfully performed because the junction vortex completely disappeared. Moreover, some results of the wing-body fairing configuration showed that the same lift coefficient can be obtained at a lower angle-of-attack than the wing-body without fairing configuration. This result indicates that the junction vortex decreases the lift force, and the designed fairing is useful enough to increase the performance of aircraft. Additional fairings, however, increase the weight of the aircraft, which can decrease the maximum range of flying even if the ratio of lift to drag (L/D) is same. The design of these fairings has to be performed in the preliminary design before freezing the external aerodynamic shape. The development of the junction vortex, however, is hard to predict in the wing design, so extra time is needed to check the performance of aircraft and the development of junction vortex during the wing design process, which is very time-consuming work. From this perspective, this study focused on the elimination of the junction vortex of the DLR-F6 aircraft without adding any additional geometric parts, like the fairings. To achieve this goal, the thin-plate type VGs were applied and optimized once again to increase the performance of aircraft [21].

1.3 Computational Fluid Dynamics

To predict the performance of an aircraft accurately, various research in the field of Computational Fluid Dynamics (CFD) has been performed. The research included grid technique, spatial discretization scheme, turbulence model, high-order technique, time integration scheme, parallel technique, and so forth.

There are two kinds of standard grid type: structured grid and unstructured grid. The structured grid has many advantages on the accuracy and the code development, but it is very difficult to conform a single block to a complicated geometry. To overcome this limitation, multi-block, patched, and overset grid techniques were

developed and have been popularly adopted. The high-lift device (flap, slat, etc.) and the wing-body configuration are typical examples of complex geometry, which grids must be generated by using the multi-block and/or the overset grid technique. The overset grid is more efficient in complex geometry, but this technique has to define the connectivity information between overlapping blocks before the flow analysis. Because the connectivity must provide accurate information for the efficiency and accuracy of the flow analysis, many improved method were developed. PEGASUS 5 [22] developed by the National Aeronautics and Space Administration (NASA) is a state-of-the-arts pre-processor for overset grid technique, which include several advanced overset technique, such as automated hole cutting, overlap optimization, a projection scheme for fixing small discretization errors in overset surfaces, and so forth. These techniques were selectively adapted to the pre-processor that developed in this study.

To develop a high-fidelity flow analysis code, Reynolds Averaged Navier-Stokes (RANS) equation is considered as a governing equation. Although the analysis using Large Eddy Simulation (LES) and Direct Numerical Simulation (DNS) can provide a more reliable solution, huge computational cost is needed for these simulations. Because the actual aircraft design process cannot provide enough time, as mentioned above, relatively a fast approach is chosen, which is RANS based flow analysis. For a spatial discretization, Roe's Flux Difference Splitting (FDS) scheme [23] and Advection Upstream Splitting Method (AUSM) [24] are employed for the approximate solution, and more advanced methods, such as RoeM scheme [25], AUSM+ scheme [26], and AUSMPW+ scheme [27] are also adopted to simulate accurately a wide scoop of flow from subsonic to supersonic. To simulate turbulent flow, the transformed $k-\varepsilon$ model [28], Wilcox's $k-\omega$ model [29, 30], and two versions of Menter's $k-\omega$ Shear Stress Transport (SST) model [28, 31] composed of two transport equations of the turbulent kinetic energy and the dissipate rate are employed. In order to obtain higher order spatial accuracy, a

Monotone Upstream-centered Scheme for Conservation Laws (MUSCL) [32] and the Multi-dimensional Limiting Process (MLP) [33] approaches are adopted to flow analysis. For a time integration, the upwind and the TVD Runge-Kutta [34] explicit methods and the Yoon's Lower Upper Symmetric Gauss Seidel (LU-SGS) [35] implicit methods are adopted to solve the governing equations efficiently. To simulate time-accurate unsteady flows, a dual time stepping method is implemented.

The pre-processor and the flow analysis code are parallelized by using the Message Passing Interface (MPI) library to utilize several types of parallel clusters. Because the previously established parallelizing structure, developed and used by Kim [5], Ko [36], and Lee [6] have great loss of time in complex systems with a large number of interface, a new message passing structure was developed and generalized. The new structure was adapted to the pre-processor, flow solver, and all other codes used in this study.

1.4 Aerodynamic Design Optimization

Aerodynamic design optimization is performed with six steps, as illustrated in Fig. 2. At first, the designer has to define the target and the objective of the design study. The design might be a wing design for decreasing a drag, a duct design for supplying uniform flow to the engine face, a flow control device design to eliminate detrimental problems developed by target shape itself, and so forth. After the determination of the target and objectives, flow characteristics have to be discovered by a flow analysis by CFD and/or an experimental study. For this step, a high-fidelity and efficient flow solver is required for the computation of pressure distribution and for calculating aerodynamic performance, such as lift, drag, moment, pressure recovery, and distortion, all of which are used as an objective function to be minimized or maximized. In this stage, the research to discover the reasons of the detrimental problems should be enthusiastically performed, and the

research to find a way to remove these problems is also conducted. Moreover, the possible candidates of design variable are collected, and the effect of these variables on the target problem is also briefly identified in this stage. Sensitive variables of candidates are distinguished by parametric study to determine which variables become the final design variables. Depending on the number of design variables and the characteristic of design space, the numerical optimization method is selected, and then the design is performed. After conducting the design, the optimized shape or condition has to be validated on the whole range of operating conditions, which is called off-design condition test. If the optimized one is acceptable in whole operating range, the aerodynamic design optimization is finished.

As shown in Figure 2, the optimization method used for the aerodynamic design optimization can be classified into two types; the Gradient Based Optimization Method (GBOM) and the non-gradient based optimization method. The goals of these two methods are the same: to find the optimum value of the objective function.

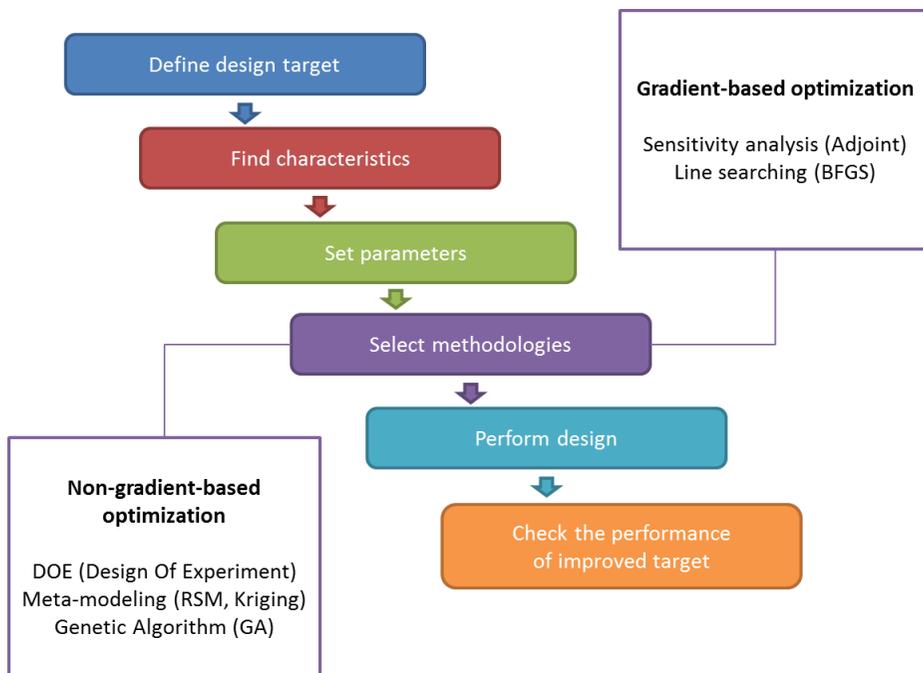


Figure 2 Strategy of aerodynamic design optimization.

However, the design approach is certainly different. In the case of the GBOM, the optimum is found by using the sensitivity derivatives of the objective function with respect to each design variable. The calculation of sensitivity information is the most important part of this approach, and finding the search direction and determining the one-dimensional step size are essential components of the optimization. Although the GBOM has advantages on the good convergence characteristics to the optimum, the found optimum can be trapped in the local optimum when the design space is composed of highly complex, non-linear functions. This characteristic is dependent on the fact that the GBOM do not predict overall shape of the objective function in the design space.

On the other hands, non-gradient based optimization can find the global optimum in defined design space by using the global optimization technique (gradient-free optimization technique), such as Genetic Algorithm (GA), Evolutionary Algorithm (EA), Simulated Annealing (SA), and so forth. These methods are based on the meta-modeling or other direct optimization techniques, which do not require the sensitivity information. Meta-modeling techniques, such as the Response Surface Model (RSM), the kriging model, and the neural network depict the design space approximately via a linear or non-linear function by calculating the sample point of the defined design space. The sample point is defined by Design of Experimental (DOE) based statistical methods, such as a Central Composite Design (CCD), Latin Hypercube Sampling (LHS), and so forth. The accuracy of this approach is seriously affected by the selection of sample points and the type of models that are used to predict the design space. The non-gradient based optimization is very useful, but there is a heavyweight disadvantage in that there is a lack of flexibility in the number of design variables. This approach, therefore, may treat maximum 5~7 design variables in the aerodynamic design optimization.

In this study, the VGs installed in the S-duct and on the wing surface were

designed. For the purpose of truly optimal design, several VGs should be independently treated by fully reflecting local flow patterns, which was the main objective of the present study. From this perspective, the GBOM was adapted to consider the large number of design variables in order to compose each VG shape separately.

1.5 Sensitivity Analysis

Traditionally, sensitivity derivatives for GBOM with respect to the design variable may be obtained by the Finite Difference Method (FDM). Because FDM is quite simple and can be easily implemented, the method is convenient for all kinds of design problems. The accuracy of FDM, however, depends on the step size for calculating the differences of functional value. Moreover, the FDM is too expensive in computational time cost to compute the function value with a large number of design variables in the aerodynamic design field [4-7].

Martines *et al.* suggested the complex step derivative method derived from the Cauchy-Riemann relation [37]. The accuracy of the sensitivity is independent of the step size, and this method can also be easily implemented. The computational time cost, however, is still high because this method has to calculate a complex number and treat each design variable separately.

The direct differentiation method [38] is another way to obtain the sensitivity information. This method yields sensitivity information by directly differentiating the governing equation, either Euler or Navier-Stokes equation in the aerodynamic design optimization. The method is very useful when the number of design variables is smaller than that of the objective function and constraints. In the aerodynamic fields, however, the term of the flow variables differentiated by design variables is included, and the calculation of this term is very time-consuming work.

To eliminate the term coupled with flow variable in the direct differentiation

method, Jameson *et al.* adopted the control theory [39]. In the control theory, the gradient is calculated by solving the adjoint equation; ergo this method is named the Adjoint Variable (AV) method. In spite of the direct differentiation method, the AV method is useful when the number of design variables is higher than that of the objective function and constraints. The cost for obtaining the sensitivity derivatives of the objective function with respect to each design variable is essentially independent of the number of design variables. This method is quite flexible and efficient in the design of aerodynamic external shape. Jameson [40] first applied the AV method in the continuous manner to the transonic flow, and this method currently has become extremely popular in aerodynamic shape optimization.

There are two ways to deal with the adjoint equation: the continuous and the discrete approaches. The governing equations are differentiated with respect to the design variables before the equations are discretized in the continuous approach, but the discrete adjoint approach is directly applying the control theory to the discretized governing equations. The derivatives obtained by using these two approaches are almost identical, but a small level of truncation error may exist. The discrete approach is highly intuitive and can be easily implemented. This approach can be advantageous in the sense that the derivatives obtained are consistent with complex step derivatives regardless of the computational cell size. Moreover, the discrete approach has an advantage of wide applicability to various problems even in the turbulent flows because the continuous approach requires a complete set of adjoint equations for the governing equations and the boundary conditions to be discretized. Specifically, the turbulent boundary condition is exceedingly difficult to be discretized, but the continuous approach has been popularly adopted for various design problems [40-42]. This approach has been adopted because the continuous approach is so efficient that the time cost of sensitivity analysis is almost the same as that of the flow analysis even if the number of design variables is large or small. A more detailed comparison of these two approaches was conducted by Nadarajah

and Jameson [43].

As mentioned above, the present study focused on treating several VG independently, a process that needs a large number of design variables; therefore, the AV method was quite valuable in the present study. To implement the VG source term model (discussed in the next section) easily to the AV solver, the discrete adjoint approach was applied as a method of sensitivity analysis.

1.6 Vortex Generator and Source Term Model

The Vortex Generator (VG) is a highly useful passive flow control device, and several VG shapes and sizes are available. The vane type of VG is a popular one and can be classified with various shapes such as the thin-plate type, the airfoil type, the triangle type, and so forth. Among the several shapes, the thin-plate type is popularly adopted because of its simplicity. The thin-plate type VG has been adopted for supplying extra energy by making small vortices induced by pressure differences between the front and rear surface of VG. The thin-plate type VG also guides flow direction parallel to the tangential direction of the VG. The small size of VG swallowed up by the boundary layer has a large influence on the extra energy while the large size of the VG is focused on guiding the flows.

Previous researchers first approached the topic of VG analysis by using a large number of computational grids, which is a fully gridded analysis. Because this analysis is extremely inefficient and hard to be analyzed, Wendt [44], Bender *et al.* [45], and Jirásek [46] modeled a thin-plate VG as a mathematical source term. Wendt [44] developed a model by calculating the strength of the shedding vortex, but it still requires a large number of grid points for accurate computational analysis. Bender *et al.* [45] developed a Bender-Anderson-Yagle (BAY) model by reflecting the lift force generated by the VG and applying it to the Navier-Stokes equation, which is the most popular source term model. Also, Jirásek [46] developed the

jBAY model for an edge-based unstructured flow solver by modifying the BAY model.

From the view point of a sensitivity analysis for GBOM, however, the original BAY model should be modified because this model is formulated with the whole volume of each computational cell that is crossed by the VG. This approach cannot reflect a small amount of positional change within a computational cell because one cell has only one source term value. Moreover, it is impossible to obtain the gradient information at an interface between the cells where the VG is crossed and not crossed, which causes the discontinuous source term value at the contacted two cells. Because of these problems, the gradient information at an interface and in a one cell cannot be calculated accurately. A differentiable BAY model was thus developed in this study by taking into account a small positional change (or a small volume change) in order to provide more accurate sensitivity information for gradient evaluation. The detail information about a differentiable BAY model is presented in Chapter. 4.

1.7 Internal Flow Design (S-shaped Offset Inlet)

As an internal flow case, the S-shaped subsonic offset inlet was considered. Because the S-shaped inlet shows the detrimental problems originated from the S-shape, researchers have shown interest in measuring the performance of the inlet. There are two parameters usually considered for the inlet: the distortion coefficient and the total pressure recovery ratio. The distortion coefficient represents the non-uniformity of the flow which may pull the compressor stall or the structural problem of the fan blade, both of which would have serious detrimental effects on the turbine engine. The total pressure recovery ratio is a gauge of the inlet efficiency measured in front of the compressor blade (the same as the engine face) [47-49].

The geometry used for flow analysis and design optimization is the RAE M2129,

an S-shaped diffusing subsonic offset inlet (S-duct) in which a strong flow separation is observed on the starboard side. The RAE M2129 geometry was introduced by the AGARD group in the 1990s [50]. Subsequently, many researchers have analyzed the flow characteristics of the S-duct. May *et al.* [51] produced computational results in a series of Aircraft Research Association (ARA) reports, in which the flow characteristics with high and low mass flow rates were examined by using several two-equation turbulence models. Since then, many researchers, such as Abrahamsen, Anderson, Kral, Menzies, Chevalier, and Dudek, have investigated the S-duct flows by using CFD analysis or wind tunnel experiments [49, 52-56].

As advanced research, for decades researchers have shown interests in controlling the flow distortion and the total pressure recovery ratio inside an inlet. One way to enhance the flow quality is to design the inlet shape so that the total pressure loss and flow distortion decreased simultaneously. For example, Lee and Kim [57] and Lee *et al.* [10] redesigned the shape of the S-duct and that of the boundary-layer-ingestion (BLI) inlet by applying the discrete adjoint approach. They demonstrated that the designed geometry maintains better performance even in off-design conditions; however, the geometric constraints of the shape design, such as fixed length, fixed curvature, and fixed inlet radius, make it difficult to implement a designed shape in the manufacturing stage.

The other way to enhance the flow quality inside the S-duct is to employ additional flow control devices, such as a vortex generator (VG), jet actuator, or Gaussian bump. Among the available flow control devices, the VG has been widely adopted to improve flows in the S-shaped inlet in many computational and experimental studies. For example, Anderson and Gibb [58] installed VGs on the expansion region of the duct to diminish the flow distortion. Dudek [59] also applied a VG to three kinds of duct geometries, such as a straight pipe, and to both a transitioning and a circular S-duct diffuser to investigate the effectiveness of device. Through the CFD analysis with the BAY model and experiments, Anderson and

Gibb [60] presented several designed VG configurations. In addition, an analysis and a design work to find optimal VG was carried out by Jirásek [61].

Until recently, the design of experiments (DOE) method has been mainly adopted for designing VGs. Jirásek [61] designed VGs with five design variables by using the jBAY model. Allan *et al.* [62] designed the height and angle of attack of the gridded VGs to minimize the flow distortion of a BLI offset inlet. Lee and Liou [63] designed an axial position of the gridded VGs installed in a BLI inlet to minimize the flow distortion and to maximize the total pressure recovery simultaneously. One of the known drawbacks of the DOE-based design is the lack of flexibility in the number of design variables; thus, the same design condition has to be imposed on all VGs. For the purpose of truly optimal design, however, each VG had to be independently treated by fully reflecting local flow patterns.

From this perspective, a high-fidelity VG design framework that handles each VG independently by adopting the BAY model and the differentiable BAY model for reducing computation cost by exploiting the benefits of the adjoint-based approach is proposed. First, three designs are performed by using the BAY model to demonstrate the validity of the proposed design framework. Then, a total of four design cases are conducted by using the differentiable BAY model to create the optimized VG shapes for the RAE M2129 S-duct [18].

1.8 External Flow Design (Wing-Body Configuration)

As an external flow case, the wing-body configuration is considered. For decades, many researchers have been interested in the performance prediction of aircraft. One of the efforts in the aerodynamic field is the Drag Prediction Workshop (DPW) conducted by the American institute of Aeronautics and Astronautics (AIAA). Since 2001, the workshop has been held several times and many research groups have participated. The participants and the committees have tried to assess the state-of-

the-art of Computational Fluid Dynamics (CFD) Reynolds Averaged Navier-Stokes (RANS) solvers in order to predict the lift and drag of industry relevant aircraft configuration, focusing principally on drag calculations [19, 64-67]. The committee provided several complex geometries: DLR-F4 wing-body configuration, DLR-F6 wing-body-nacelle-pylon configuration with/without two types of fairing, two types of simple wing named DPW-W1 and DPW-W2, and Common Research Model (CRM). Among these geometries, DLR-F6 wing-body configuration without fairing [68] introduced in the DPW-II and DPW-III was selected as the target geometry for this study.

The participants of DPW-II had difficulties in making accurate predictions about the aircraft performance coefficient, such as lift, drag, and momentum coefficients. They considered that one of the reasons for the difficulties is a junction vortex. They tried to eliminate this problem by adopting two types of side-of-body fairing, designed by Vassberg *et al.* [20], to decrease the complexity of the flow physics of the wing-body junction. Because this approach is readily acceptable, the drag prediction of DLR-F6 wing-body with fairing configuration was successfully performed, so the junction vortex completely disappeared at the DPW-III [19, 20, and 66]. One additional advantage to removing the junction vortex is that the same lift coefficient can be obtained at a lower angle-of-attack than the wing-body without fairing configuration [19, 20, and 66]. Additional fairings, however, increase the weight of the aircraft, which decreases the maximum range of flying, even if the ratio of lift to drag (L/D) is the same; thus, this additional advantage is not positive proof of an increase in the performance of the aircraft.

From this perspective, this study focused on the elimination of the junction vortex of the DLR-F6 aircraft without adding any additional geometric parts, like the fairing. One of the available ways to eliminate a junction vortex without weight increase is to install a flow control device. Among several kinds of device, a thin-plate type VG was adopted to control the stress-induced secondary flows on the

wing which is similar to the junction vortex, and to delay flow separations in high angle-of-attack and/or low speed [19, 20, and 66]. Because this application is an extension study of the design of the VG inside an S-duct, the validation of design strategy is not a vital element, but previous research that install the VG to the wing-body junction in order to diminish junction vortex does not exist; therefore, the parametric study to observe the influence of the VG to the junction must be performed. Nine cases of parametric study were conducted by changing the number, shape, angle, and position parameters of the VG. After the parametric study, three cases of design were conducted to obtain the optimized VG shape to eliminate the junction vortex [21].

Chapter II

Flow Analysis

2.1 Governing Equations

The governing equation is the three-dimensional compressible Navier-Stokes equation, which can be written in the conservative law form as follows:

$$\frac{\partial \rho}{\partial t} = \frac{\partial}{\partial x_j} (\rho u_j) \quad (2.1)$$

$$\frac{\partial}{\partial t} (\rho u_i) + \frac{\partial}{\partial x_j} (\rho u_j u_i) = -\frac{\partial p}{\partial x_i} + \frac{\partial \hat{\tau}_{ij}}{\partial x_j} \quad (2.2)$$

$$\frac{\partial \rho e_t}{\partial t} + \frac{\partial}{\partial x_j} (\rho u_j e_t) = -\frac{\partial p u_j}{\partial x_i} + \frac{\partial}{\partial x_j} [u_i \hat{\tau}_{ij} - q_j] \quad (2.3)$$

where e_t represents the total energy, and the $\hat{\tau}_{ij}$ are composed of molecular and Reynolds stresses, defined as follows:

$$\hat{\tau}_{ij} = 2\mu(S_{ij} - \frac{1}{3}S_{kk}\delta_{ij}) + \tau_{ij} \quad (2.4)$$

$$\tau_{ij} = 2\mu_t(S_{ij} - \frac{1}{3}S_{kk}\delta_{ij}) - \frac{2}{3}\rho k\delta_{ij} \quad (2.5)$$

$$S_{ij} = \frac{1}{2} \left(\frac{\partial u_i}{\partial x_j} + \frac{\partial u_j}{\partial x_i} \right) \quad (2.6)$$

where $\hat{\tau}_{ij}$ is the summation of laminar and turbulent stresses, and τ_{ij} is the

turbulent stress term. The velocity strain rate tensor is represented by S_{ij} , and k is the turbulent kinetic energy. The quantity μ is the molecular viscosity determined by the Sutherland law, and μ_t is the turbulent eddy viscosity. Note that the Boussinesq approximation is assumed to introduce Eq. 2.5. The total heat flux rate q_j is defined as

$$q_j = -\left(\frac{\gamma}{\gamma-1}\right)\left(\frac{\mu}{\text{Pr}} + \frac{\mu_t}{\text{Pr}_t}\right)\frac{\partial T}{\partial x_j} \quad (2.7)$$

where γ is the ratio of specific heats, and the variables Pr and Pr_t are the laminar and turbulent Prandtl numbers, respectively.

The perfect gas equation of state is introduced to the pressure as

$$p = \rho(\gamma-1)\left(e - \frac{1}{2}u_i u_i\right) \quad (2.8)$$

The three-dimensional compressible Navier-Stokes equations are implemented on the flow solver by the non-dimensionalized and coordinate transformed equations. Flow variables are non-dimensionalized by the freestream condition and the characteristic length as noted in the following equations:

$$\begin{aligned} \rho^* &= \frac{\rho}{\rho_\infty}, & u_i^* &= \frac{u_i}{a_\infty}, & e_t^* &= \frac{e_t}{e_{t_\infty}}, & p^* &= \frac{p}{\rho_\infty a^2}, \\ x_i^* &= \frac{x_i}{L}, & t^* &= \frac{t}{L/a_\infty}, & T^* &= \frac{T}{T_\infty} \\ \mu^* &= \frac{\mu}{\mu_\infty}, & \mu_t^* &= \frac{\mu_t}{\mu_\infty} \end{aligned} \quad (2.9)$$

The compressible Navier-Stokes equations can be expressed in general curvilinear coordinates of ξ, η, ζ as seen in the following equation:

$$\frac{1}{J} \frac{\partial Q}{\partial t} = - \left(\frac{\partial}{\partial \xi} (\hat{E} - \hat{E}_v) - \frac{\partial}{\partial \eta} (\hat{F} - \hat{F}_v) - \frac{\partial}{\partial \zeta} (\hat{G} - \hat{G}_v) \right) \quad (2.10)$$

The E , F , and G represent the flux vector of ξ -, η -, ζ -direction, respectively, and the subscript v indicates the viscous flux. The Q vector represents the conservative variables of

$$Q = [\rho, \rho u, \rho v, \rho w, \rho e_t]^T \quad (2.11)$$

For convenience, the superscript *, which means the non-dimensional value, is omitted from the equations.

2.2 Turbulence Models

For an adequate description of turbulent flow field within the framework of a Reynolds Averaged Navier-Stokes (RANS) formulation, Wilcox's original k - ω model [29, 30], transformed k - ε model [28], Menter's standard k - ω Shear Stress Transport (SST) model [28], and Menter's k - ω SST developed in 2003 [31] are employed. These turbulence models are composed of two transport equations of the turbulent kinetic energy k and the dissipate rate ω .

2.2.1 The original k - ω model

The original k - ω model developed by Wilcox *et al.* is as follows:

$$\frac{\partial(\rho k)}{\partial t} + \frac{\partial(\rho k u_j)}{\partial x_j} = \tau_{ij} \frac{\partial u_i}{\partial x_j} - \beta^* \rho \omega k + \frac{\partial}{\partial x_j} \left[(\mu + \sigma_k \mu_t) \frac{\partial k}{\partial x_j} \right] \quad (2.12)$$

$$\frac{\partial(\rho \omega)}{\partial t} + \frac{\partial(\rho \omega u_j)}{\partial x_j} = \rho \frac{\gamma_1}{\mu_t} \tau_{ij} \frac{\partial u_i}{\partial x_j} - \beta_1 \rho \omega^2 + \frac{\partial}{\partial x_j} \left[(\mu + \sigma_\omega \mu_t) \frac{\partial \omega}{\partial x_j} \right] \quad (2.13)$$

with the coefficients of

$$\sigma_{k_1} = 0.5, \sigma_{\omega_1} = 0.5, \beta^* = 0.09, \beta_1 = 0.075, \kappa = 0.41$$

$$\gamma_1 = \beta_1 / \beta^* - \sigma_{\omega_1} \kappa^2 / \sqrt{\beta^*}$$

The turbulent eddy viscosity μ_t is defined as the ratio of turbulent kinetic energy to the dissipation rate as

$$\mu_t = \rho k / \omega \quad (2.14)$$

2.2.2 The Transformed k - ε Model

The standard k - ε model is transformed into a k - ω formulation by using the relation of $\varepsilon = 0.09\omega k$. There are two differences between the transformed formulation and the original formulation. The first difference is that a small diffusion term is neglected by adding the cross-diffusion term appearing in the ω equation, and the other different point is the modeling parameters.

$$\frac{\partial(\rho k)}{\partial t} + \frac{\partial(\rho k u_j)}{\partial x_j} = \tau_{ij} \frac{\partial u_i}{\partial x_j} - \beta^* \rho \omega k + \frac{\partial}{\partial x_j} \left[(\mu + \sigma_{k_2} \mu_t) \frac{\partial k}{\partial x_j} \right] \quad (2.15)$$

$$\begin{aligned} \frac{\partial(\rho \omega)}{\partial t} + \frac{\partial(\rho \omega u_j)}{\partial x_j} = & \rho \frac{\gamma_2}{\mu_t} \tau_{ij} \frac{\partial u_i}{\partial x_j} - \beta_2 \rho \omega^2 \\ & + \frac{\partial}{\partial x_j} \left[(\mu + \sigma_{\omega_2} \mu_t) \frac{\partial \omega}{\partial x_j} \right] + 2\rho \sigma_{\omega_2} \frac{1}{\omega} \frac{\partial k}{\partial x_j} \frac{\partial \omega}{\partial x_j} \end{aligned} \quad (2.16)$$

where

$$\sigma_{k_2} = 1.0, \sigma_{\omega_2} = 0.856, \beta^* = 0.09, \beta_2 = 0.0828, \kappa = 0.41$$

$$\gamma_2 = \beta_2 / \beta^* - \sigma_{\omega_2} \kappa^2 / \sqrt{\beta^*}$$

2.2.3 The Standard Menter's k - ω Shear Stress Transport (SST) Model

The k - ω SST model is a hybrid turbulence model that combines the merits of k - ω and k - ε models by adopting an adequate blending function F_1 . As it is well known, the k - ω model shows excellent accuracy in the boundary layer even though the solution is sensitive to the freestream condition of k and ω . On the other hand, the k - ε model can obtain a good solution on the free shear layer and outer region, but it is instable near the wall. These two models, the k - ε model and the k - ω model, therefore, are integrated to solve accurately and robustly the turbulence flow not only the near wall region but also the outer region. The blending function F_1 is set to be one in the near wall region and to be zero at far away from the wall surface. The combined equations are

$$\frac{\partial(\rho k)}{\partial t} + \frac{\partial(\rho k u_j)}{\partial x_j} = P - \beta^* \rho \omega k + \frac{\partial}{\partial x_j} \left[(\mu + \sigma_k \mu_t) \frac{\partial k}{\partial x_j} \right] \quad (2.17)$$

$$\begin{aligned} \frac{\partial(\rho \omega)}{\partial t} + \frac{\partial(\rho \omega u_j)}{\partial x_j} = & \rho \frac{\gamma}{\mu_t} P - \beta \rho \omega^2 + \frac{\partial}{\partial x_j} \left[(\mu + \sigma_\omega \mu_t) \frac{\partial \omega}{\partial x_j} \right] \\ & + 2\rho(1 - F_1)\sigma_{\omega_2} \frac{1}{\omega} \frac{\partial k}{\partial x_j} \frac{\partial \omega}{\partial x_j} \end{aligned} \quad (2.18)$$

Each of the constants are defined by a blend of an inner constant of the k - ω model that is marked with the subscript 1 and outer constant of the k - ε model, which is marked with the subscript 2, via

$$\Phi = F_1 \Phi_1 + (1 - F_1) \Phi_2 \quad (2.19)$$

where Φ represents the constant of Eqs. 2.12-13 and 2.15-16. Additional functions and limiters are given by

$$P = \tau_{ij} \frac{\partial u_i}{\partial x_j} \quad (2.20)$$

$$F_1 = \tanh(\arg_1^4) \quad (2.21)$$

$$\arg_1 = \min \left[\max \left(\frac{\sqrt{k}}{\beta^* \omega d}, \frac{500\nu}{\omega d^2} \right), \frac{4\rho\sigma_{\omega_2} k}{CD_{k\omega} d^2} \right] \quad (2.22)$$

$$CD_{k\omega} = \max \left[2\rho\sigma_{\omega_2} \frac{1}{\omega} \frac{\partial k}{\partial x_j} \frac{\partial \omega}{\partial x_j}, 10^{-20} \right] \quad (2.23)$$

$$\mu_t = \frac{\rho a_1 k}{\max[a_1 \omega, \Omega F_2]} \quad (2.24)$$

$$F_2 = \tanh(\arg_2^2) \quad (2.25)$$

$$\arg_2 = \max \left(2 \frac{\sqrt{k}}{\beta^* \omega d}, \frac{500\nu}{\omega d^2} \right) \quad (2.26)$$

by letting d be the distance to the cell center point from the nearest wall and Ω be the vorticity magnitude. The summary of the constants are the following:

$$\begin{aligned} \gamma_1 &= \beta_1 / \beta^* - \sigma_{\omega_1} \kappa^2 / \sqrt{\beta^*}, & \gamma_2 &= \beta_2 / \beta^* - \sigma_{\omega_2} \kappa^2 / \sqrt{\beta^*} \\ \sigma_{k_1} &= 0.85, & \sigma_{k_2} &= 1.0, & \sigma_{\omega_1} &= 0.5, & \sigma_{\omega_2} &= 0.856 \\ \beta^* &= 0.09, & \beta_1 &= 0.075, & \beta_2 &= 0.0828, & \kappa &= 0.41 \\ a_1 &= 0.31 \end{aligned}$$

Note that it is generally recommended to employ the production limiter, which replaces the term of P in the k -equation Eq. 2.17 by:

$$P = \min(P, 20\beta^* \rho \omega k) \quad (2.27)$$

The boundary conditions and freestream values are given as follows:

$$\frac{U_\infty^2}{10^5 \text{Re}_L} < k_{farfield} < \frac{U_\infty^2}{10 \text{Re}_L} \quad (2.28)$$

$$\frac{U_\infty}{L_{farfield}} < \omega_{farfield} < \frac{10U_\infty}{L_{farfield}} \quad (2.29)$$

$$k_{wall} = 0 \quad (2.30)$$

$$\omega_{wall} = \frac{60\mu}{\beta_1 \rho (\Delta d)^2} \quad (2.31)$$

The $L_{farfield}$ is the approximate length of the computational farfield domain from the wall, and a freestream turbulent viscosity μ_t has a value between 10^{-5} and 10^{-2} times the freestream laminar viscosity.

2.2.4 The Menter's $k-\omega$ SST Model from 2003 ($k-\omega$ SST-2003)

The $k-\omega$ SST-2003 has several relatively minor variation from the original SST developed in 1994. The model enhancements cover a modified near wall treatment of the equations, which allows a more flexible grid forms. This advantage reduces the problem of grid induced separation for industrial flow simulations. The changes are in the definition of eddy viscosity and in the production limiter of Eq. 2.24. The magnitude of vorticity in the eddy viscosity is changed to the strain invariant (S) in its definition as follows:

$$\mu_t = \frac{\rho a_1 k}{\max[a_1 \omega, SF_2]} \quad (2.32)$$

where

$$S = \sqrt{2S_{ij}S_{ij}}$$

The production limiter is adopted for the k -equation in the original SST model

but this limiter is expanded to both k - and ω -equations. The limiting constant is also changed from 20 to 10.

$$P = \min\left(P, 10\beta^* \rho \omega k\right) \quad (2.33)$$

Another limiter in the definition of $CD_{k\omega}$, is slightly different in that it uses 10^{-10} rather than 10^{-20} for its second term.

$$CD_{k\omega} = \max\left[2\rho\sigma_{\omega_2} \frac{1}{\omega} \frac{\partial k}{\partial x_j} \frac{\partial \omega}{\partial x_j}, 10^{-10}\right] \quad (2.34)$$

The changed coefficients are:

$$\gamma_1 = \frac{5}{9}, \quad \gamma_2 = 0.44$$

2.3 Spatial Discretization

As shown in Eq. 2.10, the governing equations can be decomposed to the inviscid flux term and to the viscous flux term. The inviscid flux terms in the ξ -, η -, and ζ -directions are discretized with a finite volume method based on the cell-centered approach. The local flux balance of each cell is

$$\begin{aligned} \left(\frac{\partial E}{\partial \xi} + \frac{\partial F}{\partial \eta} + \frac{\partial G}{\partial \zeta}\right)_{i,j,k} &= \tilde{E}_{i+\frac{1}{2},j,k} - \tilde{E}_{i-\frac{1}{2},j,k} \\ &+ \tilde{F}_{i,j+\frac{1}{2},k} - \tilde{F}_{i,j-\frac{1}{2},k} \\ &+ \tilde{G}_{i,j,k+\frac{1}{2}} - \tilde{G}_{i,j,k-\frac{1}{2}} \end{aligned} \quad (2.35)$$

Because Eq. 2.35 is in a central-differenced form and in a non-dissipative by

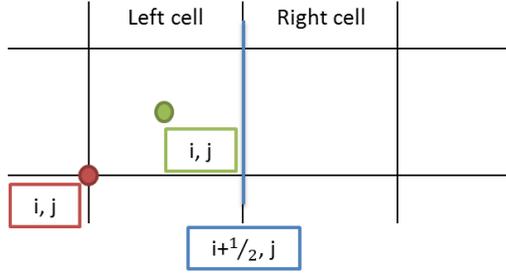


Figure 3 Cell indexes in two-dimensional grid.

itself, the inviscid fluxes should be modified to the cell surface fluxes by explicitly adding the numerical dissipation term as follows:

$$\tilde{E}_{i+\frac{1}{2},j,k} = \frac{1}{2} \left[\hat{E}(Q_i) + \hat{E}(Q_{i+1}) - \left| \hat{A}(Q_i, Q_{i+1}) \right| (Q_{i+1} - Q_i) \right] \quad (2.36)$$

where the matrix $\hat{A}(Q_i, Q_{i+1})$ is the flux Jacobian matrix, and the inviscid flux is upwind-differenced. In this work, two types of flux schemes of Roe's FDS and RoeM are usually used for the spatial discretization.

The two-dimensional indexes are shown in Fig. 3. The grid points are located in the red color vertex, the variables are posed in the cell-center illustrated by the green color, and the fluxes are calculated at the blue edge.

2.3.1 Roe's Flux Difference Splitting

Roe's Flux Difference Splitting (FDS) scheme is based on the approximate solution of the Riemann problem [23]. Instead of solving the exact Riemann problem iteratively, Roe linearized the Jacobian matrix to satisfy the following properties:

- (1) \hat{A} is a linear mapping to \hat{E} in a vector space Q
- (2) \hat{A} satisfies consistency condition, so $\hat{A}(Q, Q) = \hat{A}(Q)$
- (3) \hat{A} has linearly independent eigenvectors and real eigenvalues.

$$(4) \quad \hat{A}(Q_i, Q_{i+1})(Q_{i+1} - Q_i) = \hat{E}_{i+1} - \hat{E}_i \quad \text{for any } Q_i, Q_{i+1}$$

From the condition (4), the linearized flux Jacobian \hat{A} can be expressed in terms of Roe-averaged properties $\bar{\rho}$ and \bar{Q} as

$$\bar{\rho} = \sqrt{\rho_i \rho_{i+1}} \quad (2.37)$$

$$\bar{Q} = \frac{Q_i \sqrt{\rho_i} + Q_{i+1} \sqrt{\rho_{i+1}}}{\sqrt{\rho_i} + \sqrt{\rho_{i+1}}} \quad (2.38)$$

From the eigenmatrix \hat{X} of \hat{A} , the diagonal matrix Λ composed of eigenvalues, and the condition (2), the third term on the right-hand side of Eq. 2.36, are replaced into a vector calculation as

$$\left| \hat{A}(Q) \right| (Q_{i+1} - Q_i) = \left(\hat{X} |\Lambda| \hat{X}^{-1} \right) \hat{X} \hat{\alpha} = \hat{X} |\Lambda| \hat{\alpha} = \hat{\alpha}_k |\lambda_k| \hat{e}_k \quad (2.39)$$

By using these Roe-averaged properties noted with the superscript of -, the flux can be calculated as follows:

$$\tilde{E}_{i+1/2} = \frac{1}{2} \left[\hat{E}(Q_i) + \hat{E}(Q_{i+1}) - \hat{\alpha}_k |\lambda_k| \hat{e}_k \right] \quad (2.40)$$

$$\hat{\alpha}_k |\lambda_k| \hat{e}_k = \begin{bmatrix} \alpha_4 \\ \bar{u} \alpha_4 + \hat{\xi}_x \alpha_5 + \alpha_6 \\ \bar{v} \alpha_4 + \hat{\xi}_y \alpha_5 + \alpha_7 \\ \bar{w} \alpha_4 + \hat{\xi}_z \alpha_5 + \alpha_8 \\ \bar{H} \alpha_4 + (\bar{U} - \hat{\xi}_t) \alpha_5 + \bar{u} \alpha_6 + \bar{v} \alpha_7 + \bar{w} \alpha_8 - \frac{\bar{a}^2}{\gamma - 1} \alpha_1 \\ \alpha_9 \\ \alpha_{10} \end{bmatrix} \quad (2.41)$$

The coefficients of α are

$$\begin{aligned}
\alpha_1 &= |\lambda_1| \left(\Delta\rho - \frac{\Delta p}{\bar{a}^2} \right), & \alpha_2 &= |\lambda_4| \left(\frac{\Delta p + \bar{\rho}\bar{a}\Delta U}{2\bar{a}^2} \right) \\
\alpha_3 &= |\lambda_3| \left(\frac{\Delta p - \bar{\rho}\bar{a}\Delta U}{2\bar{a}^2} \right), & \alpha_4 &= \alpha_1 + \alpha_2 + \alpha_3 \\
\alpha_5 &= \bar{a} (\alpha_2 - \alpha_3), & \alpha_6 &= |\lambda_1| \left(\bar{\rho}\Delta u - \hat{\xi}_x \bar{\rho}\bar{U} \right) \\
\alpha_7 &= |\lambda_1| \left(\bar{\rho}\Delta v - \hat{\xi}_y \bar{\rho}\bar{U} \right), & \alpha_8 &= |\lambda_1| \left(\bar{\rho}\Delta w - \hat{\xi}_z \bar{\rho}\bar{U} \right) \\
\alpha_9 &= |\lambda_1| \bar{\rho}\Delta k, & \alpha_{10} &= |\lambda_1| \bar{\rho}\Delta w
\end{aligned}$$

where

$$\begin{aligned}
\lambda_1 = \lambda_2 = \lambda_3 &= \frac{|\nabla \xi|}{J} \bar{U}, & \lambda_{4,5} &= \frac{|\nabla \xi|}{J} (\bar{U} \pm \bar{a}) \\
\bar{U} = \hat{\xi}_t + \hat{\xi}_x \bar{u} + \hat{\xi}_y \bar{v} + \hat{\xi}_z \bar{w}, & \hat{\xi}_{t,x,y,z} &= \frac{\xi_{t,x,y,z}}{|\nabla \xi|} = \frac{\xi_{t,x,y,z}}{\sqrt{\xi_x^2 + \xi_y^2 + \xi_z^2}} \\
H &= \frac{(e_t + p)}{\rho}
\end{aligned}$$

The flux vectors $\tilde{F}_{j+1/2}$ and $\tilde{G}_{k+1/2}$ respectively on the η - and ζ -directions can be determined with a similar flux calculation.

2.3.2 RoeM Scheme

Although the Roe scheme shows remarkable accuracy, it is hard to distinguish a shock and an expansion discontinuity because the entropy condition is violated. The carbuncle phenomena also suffer the robustness of the original Roe scheme. In order to overcome these problems, Kim *et al.* [25] proposed an improved Roe scheme that is free from the shock instability and preserves the accuracy and efficiency of the original Roe scheme.

The flux can be calculated by

$$\begin{aligned}\tilde{E}_{i+1/2} &= \frac{b_1 \times \hat{E}(Q_i) + b_2 \times \hat{E}(Q_{i+1})}{b_1 - b_2} + \frac{b_1 \times b_2}{b_1 - b_2} \Delta Q^* \\ &\quad - g \frac{b_1 \times b_2}{b_1 - b_2} \times \frac{1}{1 + |\bar{M}|} B \Delta Q\end{aligned}\quad (2.42)$$

$$\Delta Q^* = \Delta \begin{pmatrix} \rho \\ \rho u \\ \rho v \\ \rho w \\ \rho H \end{pmatrix}, \quad B \Delta Q = \left(\Delta \rho - f \frac{\Delta p}{\hat{c}^2} \right) \begin{pmatrix} 1 \\ \bar{u} \\ \bar{v} \\ \bar{w} \\ \bar{H} \end{pmatrix} + \bar{\rho} \begin{pmatrix} 0 \\ \Delta u - \xi_x \Delta U \\ \Delta v - \xi_y \Delta U \\ \Delta w - \xi_z \Delta U \\ \Delta H \end{pmatrix}\quad (2.43)$$

where

$$\bar{M} = \bar{U} / \bar{a}, \quad b_1 = \max(0, \bar{U} + \bar{a}, U_{i+1} + \bar{a}), \quad b_2 = \max(0, \bar{U} - \bar{a}, U_{i-1} + \bar{a})$$

The functions f and g can be expressed by:

$$f = \begin{cases} 1 & , \bar{u}^2 + \bar{v}^2 + \bar{w}^2 = 0 \\ |\bar{M}|^h & , \text{elsewhere} \end{cases},\quad (2.44)$$

$$h = 1 - \min \left(\begin{matrix} P_{i+1/2,j,k}, P_{i,j+1/2,k}, P_{i,j-1/2,k}, P_{i,j,k+1/2}, P_{i,j,k-1/2}, \\ P_{i+1,j+1/2,k}, P_{i+1,j-1/2,k}, P_{i+1,j,k+1/2}, P_{i+1,j,k-1/2} \end{matrix} \right)$$

$$g = \begin{cases} |\bar{M}|^{1 - \min \left(\frac{P_{i,j}, P_{i+1,j}}{P_{i+1,j}, P_{i,j}} \right)} & , \bar{M} = 0 \\ 1 & , \bar{M} \neq 0 \end{cases}\quad (2.45)$$

The differentiation of the flux function becomes more complicated than the original Roe scheme because of the function f considering the 10 cells around the interface.

2.3.3 Higher Order Spatial Accuracy

Monotone Upstream-centered Schemes for Conservation Laws (MUSCL) provide a highly accurate numerical solution for a given system even if the flow fields exhibit shock and the discontinuity phenomena [32]. The MUSCL scheme is adopted as

$$\begin{aligned} q_{i+\frac{1}{2}}^{Left} &= q_i + \frac{1}{4} \left[(1-\kappa) \phi_{i-\frac{1}{2}}^+ (q_i - q_{i-1}) + (1+\kappa) \phi_{i+\frac{1}{2}}^- (q_{i+1} - q_i) \right] \\ q_{i+\frac{1}{2}}^{Right} &= q_{i+1} + \frac{1}{4} \left[(1+\kappa) \phi_{i+\frac{1}{2}}^- (q_{i+1} - q_i) + (1-\kappa) \phi_{i+\frac{3}{2}}^+ (q_{i+2} - q_{i+1}) \right] \end{aligned} \quad (2.46)$$

where q denotes the primitive variables. When a constant $\kappa=1/3$, the order of spatial accuracy is third, and the second order accuracy is achieved with $\kappa=-1, 0, 1$. Specially at $\kappa=1$, it becomes a central difference scheme of the second order. Values of the primitive variables at the cell interface are modified by extrapolation, which cause an oscillation near physical discontinuities. To suppress this overshoot phenomenon of the solution, several limiters can be applied by using a function ϕ .

Because the MUSCL scheme is developed in the one-dimensional approach, it is insufficient to control oscillation near shock discontinuity in two- or three-dimensions. To overcome this limitation, the Multi-dimensional Limiting Process (MLP) [33] is also adopted. The vertex point value is expressed in terms of variations across the cell-interface, and by adopting the multi-dimensional restriction coefficient α , the MLP derives the multi-dimensional limiting function. The MLP scheme is

$$\begin{aligned} q_{i+\frac{1}{2}}^{Left} &= q_i + \frac{1}{2} \phi(r_{Left}) \Delta q_{i-\frac{1}{2}} \\ q_{i+\frac{1}{2}}^{Right} &= q_{i+1} - \frac{1}{2} \phi(r_{Right}) \Delta q_{i+\frac{3}{2}} \end{aligned} \quad (2.47)$$

where

$$\begin{aligned}
r_{Left} &= \frac{\Delta q_{i+1/2}}{\Delta q_{i-1/2}}, & r_{Right} &= \frac{\Delta q_{i+1/2}}{\Delta q_{i+3/2}} \\
\phi(r) &= \max(0, \min(\alpha, \alpha r, \beta)) \\
1 \leq \alpha &\leq \min \left[2, \frac{2 \max(1, r_{Left,j}) (1 + \max(0, \tan \bar{\theta}_{j+1} / r_{Right,j+1}))}{(1 + \tan \tilde{\theta}_j)} \right] \\
\tan \tilde{\theta}_j &= \Delta q_x^+ / \Delta q_y^+, & \tan \bar{\theta}_j &= \Delta q_{i+1/2,j} / \Delta q_{i,j+1/2}
\end{aligned}$$

and $\Delta q_{x,y}^\pm$ is variation from center point to the cell-interface. The coefficient β is the local slope evaluated by a higher order polynomial interpolation, which is determined by the third-order polynomial interpolation as follows:

$$\beta_{Left} = \frac{1 + 2r_{Left,i}}{3}, \quad \beta_{Right} = \frac{1 + 2r_{Right,i+1}}{3} \quad (2.48)$$

, or the fifth-order polynomial interpolation as follows:

$$\begin{aligned}
\beta_{Left} &= \frac{-2/r_{Left,i} + 11 + 24r_{Left,i} - 3r_{Left,i}r_{Left,i+1}}{30} \\
\beta_{Right} &= \frac{-2/r_{Right,i+2} + 11 + 24r_{Right,i+1} - 3r_{Right,i+1}r_{Right,i}}{30}
\end{aligned} \quad (2.49)$$

2.3.4 Compact Scheme for Viscous Fluxes

In order to discretize the viscous flux terms, a second order central differencing is adopted. The followings are the nine components for the three-dimensional case:

$$\begin{aligned}
& \frac{\partial}{\partial \xi} \left(\alpha \frac{\partial q}{\partial \xi} \right), \quad \frac{\partial}{\partial \xi} \left(\alpha \frac{\partial q}{\partial \eta} \right), \quad \frac{\partial}{\partial \xi} \left(\alpha \frac{\partial q}{\partial \zeta} \right), \\
& \frac{\partial}{\partial \eta} \left(\alpha \frac{\partial q}{\partial \xi} \right), \quad \frac{\partial}{\partial \eta} \left(\alpha \frac{\partial q}{\partial \eta} \right), \quad \frac{\partial}{\partial \eta} \left(\alpha \frac{\partial q}{\partial \zeta} \right), \\
& \frac{\partial}{\partial \zeta} \left(\alpha \frac{\partial q}{\partial \xi} \right), \quad \frac{\partial}{\partial \zeta} \left(\alpha \frac{\partial q}{\partial \eta} \right), \quad \frac{\partial}{\partial \zeta} \left(\alpha \frac{\partial q}{\partial \zeta} \right)
\end{aligned} \tag{2.50}$$

where α contains the molecular and turbulent viscosity, the Jacobian, and the metrics of the transformation. The primitive variable is denoted by q .

For example, the non-cross derivative components are discretized by using a compact three-point formula, such as

$$\begin{aligned}
\frac{\partial}{\partial \xi} \left(\alpha \frac{\partial q}{\partial \xi} \right)_{i,j,k} &= \frac{\alpha_{i+1,j,k} + \alpha_{i,j,k}}{2} (q_{i+1,j,k} - q_{i,j,k}) \\
&\quad - \frac{\alpha_{i,j,k} + \alpha_{i-1,j,k}}{2} (q_{i,j,k} - q_{i-1,j,k})
\end{aligned} \tag{2.51}$$

The cross derivative components are discretized by using the following nine-point formula:

$$\begin{aligned}
\frac{\partial}{\partial \xi} \left(\alpha \frac{\partial q}{\partial \eta} \right)_{i,j,k} &= \frac{\alpha_{i+1,j,k} + \alpha_{i,j,k}}{8} \left[(q_{i+1,j+1,k} - q_{i,j+1,k}) - (q_{i+1,j-1,k} - q_{i,j-1,k}) \right] \\
&\quad - \frac{\alpha_{i,j,k} + \alpha_{i-1,j,k}}{8} \left[(q_{i,j+1,k} - q_{i-1,j+1,k}) - (q_{i,j-1,k} - q_{i-1,j-1,k}) \right]
\end{aligned} \tag{2.52}$$

Likewise, the other components can be discretized by the same formula.

2.4 Time Integration

The governing equations of Eq. 2.10 can be represented with the vector of the residuals $R(Q)$ to easily consider the time integrating formulation easily, such as:

$$\frac{1}{J} \frac{\partial Q}{\partial t} = -R(Q) \quad (2.53)$$

In the case of a steady-state calculation, the details of the transient solution are immaterial, and the time stepping scheme may be designed solely to maximize the rate of convergence.

For time-accurate unsteady problems, a dual time stepping method should be employed to adopt an implicit formula. The time derivative term is differenced by using a backward second-order implicit formula and moving it to the right hand side of the equations. When a pseudo time of τ is imposed, then the Eq. 2.53 has the following form:

$$\frac{1}{J} \frac{\partial Q^{n+1,s+1}}{\partial \tau} = -R(Q^{n+1,s+1}) - \frac{3Q^{n+1,s+1} - 4Q^n + Q^{n-1}}{2\Delta t} \quad (2.54)$$

Here the superscript of n denotes the physical time level, and s indicates the pseudo time level. The equation is then discretized in pseudo time using the Euler implicit method and linearized using flux Jacobian. This leads to the large system of linear equations in delta form at each pseudo time step, such as:

$$\left(\frac{I}{J\Delta\tau} + \left[\frac{\partial R}{\partial Q} \right] + \frac{1.5I}{J\Delta t} \right) \Delta Q^{n+1,s} = -R(Q^{n+1,s}) - \frac{3Q^{n+1,s} - 4Q^n + Q^{n-1}}{2J\Delta t} \quad (2.55)$$

For the converged solution of steady-state calculation and the pseudo time solution in unsteady calculation, an implicit time integration scheme can be used. In

this study, the Lower-Upper Symmetric Gauss-Seidel (LU-SGS) scheme [35] is generally used, for it can reduce considerable memory and computing time in three-dimensional computation. The LU-SGS scheme requires only the scalar calculation for matrix inversion.

The left hand side of Eq. 2.53 is inverted approximately as follows:

$$LD^{-1}U\Delta Q = -R(Q) \quad (2.56)$$

where

$$\begin{aligned} L &= \frac{I}{J\Delta t} + \left[\delta_{\xi}^{-} \hat{A}^{+} + \delta_{\eta}^{-} \hat{B}^{+} + \delta_{\zeta}^{-} \hat{C}^{+} - \hat{A}^{-} - \hat{B}^{-} - \hat{C}^{-} \right] \\ D &= \frac{I}{J\Delta t} + \left[\hat{A}^{+} + \hat{B}^{+} + \hat{C}^{+} - \hat{A}^{-} - \hat{B}^{-} - \hat{C}^{-} \right] \\ U &= \frac{I}{J\Delta t} + \left[\delta_{\xi}^{+} \hat{A}^{-} + \delta_{\eta}^{+} \hat{B}^{-} + \delta_{\zeta}^{+} \hat{C}^{-} + \hat{A}^{+} + \hat{B}^{+} + \hat{C}^{+} \right] \\ \hat{A}^{\pm} &= \frac{1}{2} \left(\hat{A} \pm \kappa \left| \max \left(\text{eigenvalue} \left(\hat{A} \right) \right) \right| \right) \end{aligned}$$

Local time stepping is used for the determination of the time step during sub-iteration.

2.5 Parallelization of Flow Solver

In order to consider several large size problems, a generalized parallel algorithm is essential. The parallel algorithm previously developed is quite useful for the problems of simple grid structure. The previous algorithm, however, should be improved because the dead-lock problem can occur when the grid has an O-type structure and the large size interface data which are larger than the buffer size of networking. It also has a big disadvantage on the communication cost when a large number of interfaces are on a line.

A newly designed parallel algorithm, therefore, was developed in this study to increase the efficiency and the convenience of the flow analysis. This algorithm has many advantages on the complex multi-block grid even if the grid direction is twisted and if the large size data passing occurred at the interface. It is also faster than the previous one in any condition. The algorithm is based on the Message Passing Interface (MPI) and successfully tested on many MPI standards, such as MPICH-2, OpenMPI, MS-MPI, MVAPICH2, and so forth. The detail algorithm is presented in Appendix A.

2.6 Overset (Chimera) Grid Technique

When a complex geometry has to be composed by a structured grid, the overset grid technique, also called the chimera grid embedding scheme, is notably useful and increases the efficiency of flow analysis. Because the overset grid technique is one of the widely used grid system for the large scale flow analysis, this grid technique was then applied to the wing-body configuration of this study.

By using the overset grid technique, the flow analysis conducts with the three steps as shown in Fig. 4.

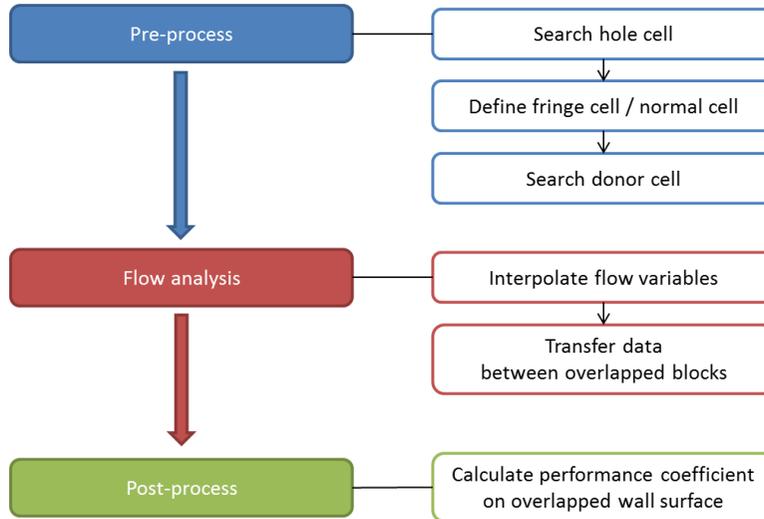


Figure 4 Flow analysis steps by using overset grid technique.

2.6.1 Pre-process of Overset Grid Technique

Because the overlapped blocks for each geometric part are created independently, the connectivity data between the overlapped blocks have to be created before the flow analysis. The whole cells of each block are classified as normal, hole, fringe, and donor cells, and then the connectivity information between the fringe cell and the donor cell is constructed. All of these works performed in the pre-process step.

For the cutting hole, a surface normal vector method [69] is adopted. The normal vector method classifies the cells by where they are located inside of the cutting surface, which is named the hole cell, or outside of the surface. The selected hole cells are excluded from the calculation. The wall surface of the other blocks is usually used as a cutting surface. A more advanced algorithm, such as a ray casting method, a hole-map method, and an object x-ray method, existed [69] and these methods have merits on the complexity and the robustness of grid topology. Although the normal vector based method has one significant restrict condition that hole-cutting surfaces must be convex and closed, this method is very useful in terms

of the simplicity and the convenience. After the hole cutting process is complete, the fringe cells receiving the data from the other block are defined, and the connectivity between the blocks are defined by using a bi-linear interpolation method in a two-dimensional approach or a tri-linear interpolation method in a three-dimensional approach.

Generally, the overset grid system of complex geometries typically has three or more overlapped blocks in the same physical domain, and this region makes the overset connectivity more complex. In this case, one fringe cell has more than one donor candidate cell in other blocks. Because defined connectivity influences the accuracy of flow analysis and because there are huge amount of fringe cells in each block, it is impossible to construct the data structure manually for the connectivity of the overset grid. Thus, the automatic way to find block connectivity is essential, and one of the approaches is the overlap optimization method [22]. This method classifies the donor cell automatically, and it can improve the convergence characteristics and the accuracy of the flow analysis by considering the cell volume ratio and cell aspect ratio between fringe cell and possible donor cells.

In the region where the curved wall surface grids are overlapped with difference distribution, the connectivity cannot be accurately defined because the linearly discretized surface meshes are not aligned exactly. This problem directly influences the accuracy of flow analysis, especially in the viscous flow calculation that depicts the boundary layer. When the curved surface has a concave curvature, the fringe cell point located near the wall lies on the true surface of the body, but it has the cells that do not have legal interpolation stencils. In this case, any of these cells that must be interpolated from the other block would be orphan cells. In the case of a convex curvature, on the other hands, the point of the fringe cell finds the donor cells, but these donor cells are located much farther away from the true wall surface. To correct this problem, the interpolation coefficients and the stencils can be modified by sub-cell Trans Finite Interpolation (TFI) [22, 70]. This method introduces an

error correction term for the distance to the wall for any sub-cell location.

2.6.2 Flow analysis with Overset Grid Technique

In the flow analysis step, donor cells interpolate values by using the constructed interpolation coefficients and transfer these data to the recipient cells in the other blocks in every sub-iteration. The parallel algorithm presented in Section 2.5 is modified and adopted once again, which is also presented in Appendix A.

2.6.3 Post-process of Overset Grid Technique

In order to calculate performance coefficient in the overlapped wall surface, the Spline Boundary Intersecting Grid (S-BIG) scheme [6] was applied. The Zipper grid scheme [71] has been widely adopted but this method is difficult to treat in an adjoint solver for sensitivity analysis, which is mentioned in Chapter III, because the Zipper grid is a kind of block reconstruction technique. Because the S-BIG scheme reconstructs the grids on the cell level, there is no more data interpolation in the overlapped surface. By using the S-BIG scheme, aerodynamic coefficients, such as lift, drag, and moment coefficients, can be calculated in overlapped wall surface.

2.7 Validation of Flow Solver

Because the present flow solver is improved and generalized by the newly designed parallel algorithm, by the state-of-the-art schemes, such as the SST 2003 turbulence model, the MLP higher order scheme, and the overlap optimization, and by the various boundary conditions, the flow solver had to be validated prior to analyzing the target geometry. To validate the flow solver without any interference, the grid and the condition that were previously validated by other researchers are used. From the web-site of the National Program for Applications-oriented Research in CFD (NPARC) alliance CFD verification and validation presented by the National

Aeronautics and Space Administration (NASA) [72], RAE 2822 transonic airfoil and NLR airfoil with flap, which are the conventional validation problems, are adopted as the first and the second validation cases. Because the present flow solver is based on the three-dimensional approach, these airfoils were expanded in a span-wise direction as an infinite wing. For complex geometry, a wing presented by the American Institute of Aeronautics and Astronautics (AIAA) and NASA at the third Drag Prediction Workshop (DPW-III) [19], which is DPW-W1, was analyzed by adopting both multi-block and overset grid approaches. All of these problems were calculated by using the Roe/RoeM scheme and the LU-SGS scheme for steady-state solution.

2.7.1 Case I: RAE 2822 Airfoil (Infinite Wing)

The Royal Aircraft Establishment (RAE) 2822 airfoil [73] transformed to an infinite wing is the first validation case. The geometry has the maximum thickness of 12.1% of chord and a sharp trailing edge, as shown in Fig. 5 (Red line). The grid is a single-block C-type with dimensions of 396 x 65 x 3, which is shown together with the geometry in Fig. 5. The first grid point off the wall is at a distance of $10^{-5} ft.$ from the airfoil surface, and the outer boundary is extended to minimum 20 times of chord length. This case has two freestream conditions that were supplied by NASA and AGARD group, as summarized in Table 1.

Table 1 Freestream conditions for RAE 2822 airfoil.

Case	Mach Number	Temperature (°K)	Angle-of-Attack (deg.)	Reynolds Number
1	0.729	255.56	2.31	6.5 million
2	0.734		2.79	

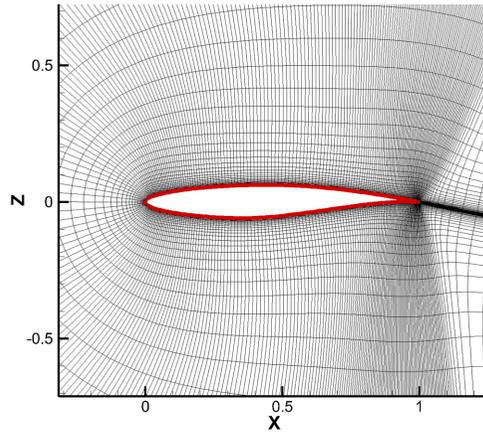
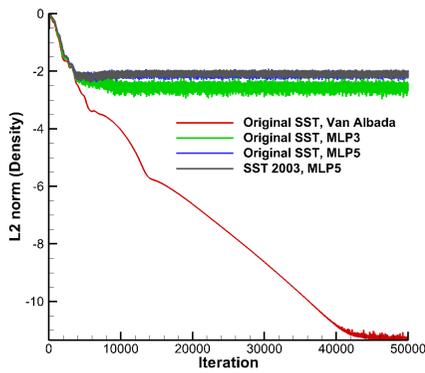


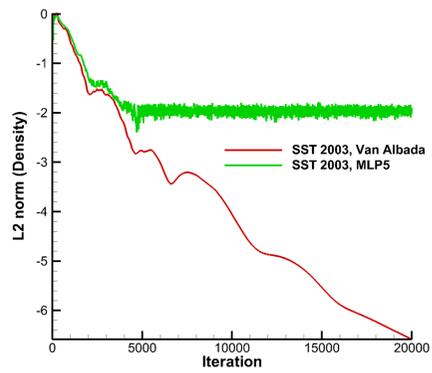
Figure 5 Shape and grid of RAE 2822 airfoil.

Computed results from the standard $k-\omega$ SST and the $k-\omega$ SST-2003 were compared to the experimental data presented by AGARD group [73]. Moreover, the result computed using the MUSCL scheme with the Van Albada limiter and the MLP scheme with MLP3/MLP5 limiters were also compared to the experimental data. The error convergence was checked by the $L2$ norm of density residual, and the computed results converged at less than 10^{-11} order when the MUSCL scheme was adopted even in the standard $k-\omega$ SST and the $k-\omega$ SST 2003. The MLP3 and MLP5 did not converge well with density residual but it is converged well with lift and drag coefficients because the small shock movement occurred while the shock was more accurately captured.

The residual history is shown in Fig. 6. The pressure contour is illustrated in Fig. 7, and the pressure coefficient (C_p) graph is presented in Fig. 8. Figure 9 shows the convergence history of lift and Fig. 10 shows that of drag coefficient. In these figures, the left one is the results of Case 1, and the right one is the results of Case 2.

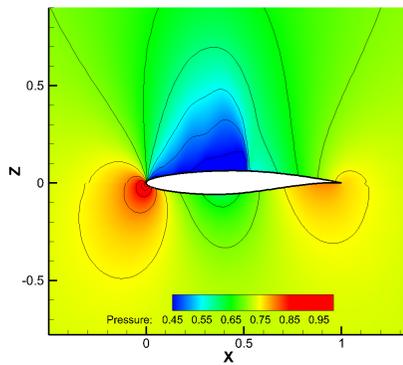


(Case 1)

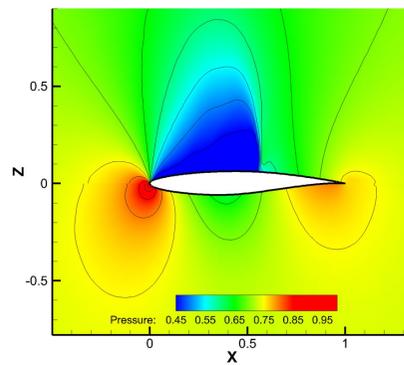


(Case 2)

Figure 6 History of L_2 norm density residual.



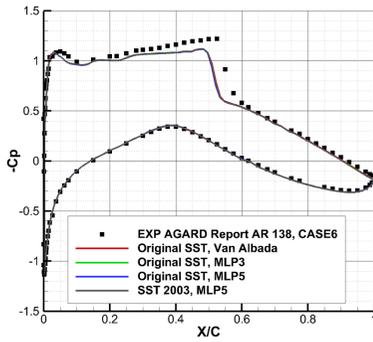
(Case 1)



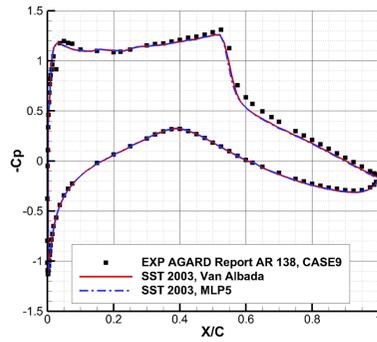
(Case 2)

Figure 7 Pressure contours near the airfoil.

The shock appears on the wing upper surface, and this phenomenon is well captured in both of Cases 1 and 2. The discontinuity of the contour line appears because the variables are plotted with cell-centered value.



(Case 1)



(Case 2)

Figure 8 Pressure coefficients on the airfoil section.

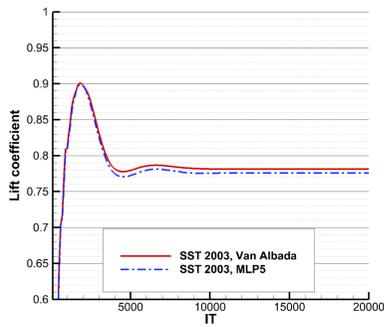
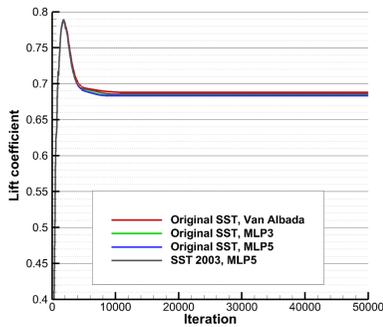


Figure 9 Convergence of the lift on the airfoil with iterations.

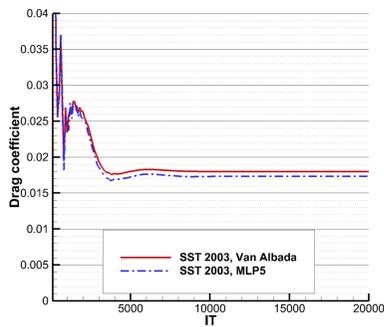
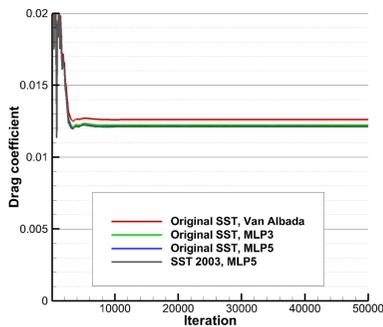


Figure 10 Convergence of the drag on the airfoil with iterations.

The results proved that the multi-block flow solver is well validated, and the higher-order schemes and turbulence models do not heavily influence the accuracy of the result, but convergence characteristics do. Although the C_p curve of Case 1 is

not in agreement with the experimental data, this issue is not a flow solver problem, but the correction of wind-tunnel data was, as proved by the results of the other researchers.

2.7.2 Case II: NLR 7301 Airfoil with Flap (Infinite Wing)

To validate the flow solver with the overset grid technique, National Aerospace laboratory of the Netherlands (NLR) 7301 airfoil was considered with the flap. This problem can validate only basic pre-process techniques for the overset grid technique, except for the advanced pre- and post-processing schemes, such as the overlap optimization, the sub-cell TFI, and the SBIG scheme. This situation occurs because the grid of this problem was composed only two blocks for the airfoil and the flap. Furthermore, the overlapped wall surface did not exist. The airfoil block had dimensions of 205 x 59 x 3, and the flap block had dimensions of 179 x 33 x 3, which were expended from two-dimensional airfoil to three-dimensional infinite wing. Figure 11 shows the two blocks with the overlapping.

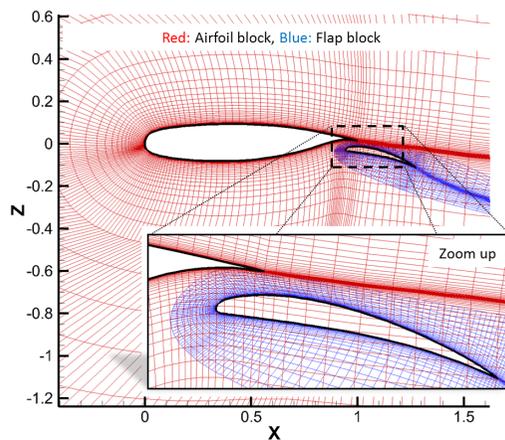


Figure 11 Shape and grids of NLR 7301 airfoil with flap.

The freestream conditions are summarized in Table 2.

Table 2 Freestream conditions for NLR 7301 airfoil with flap.

Mach Number	Temperature (°K)	Angle-of-Attack (deg.)	Reynolds Number
0.2	288.89	10.0	2.83 million

The MUSCL, along with the Van Albada limiter, was used for third order interpolation, and the $k-\omega$ SST-2003 turbulence model was employed for the high-fidelity flow analysis. The flow solver runs before reaching the convergence criteria, which set to -6 order of $L2$ norm in density. The curve of pressure coefficient (C_p) is presented in Fig. 12, as a result, and provides reasonably good agreements with experimental data. Because this problem has incompressible flow physics, the computed results by compressible flow solver could be reach the peak of pressure coefficient located on the leading-edge.

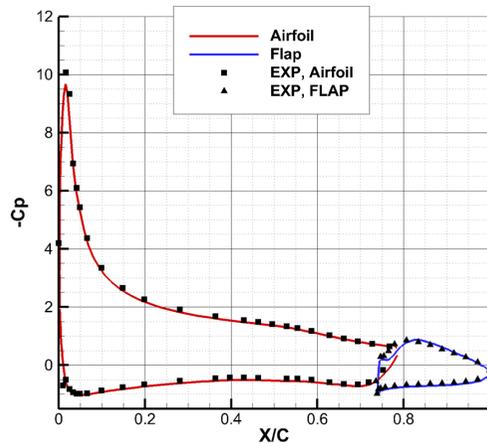


Figure 12 Pressure coefficient of NLR 7301 airfoil with flap.

2.7.3 Case III: DPW-W1

The two wing-alone geometries of DPW-W1/W2 were supplied at DPW-III. Both have a common simple, trapezoidal, planform shape with no leading-edge or trailing-edge breaks. In this study, only the DPW-W1 was considered for verification. The airfoil which applied for DPW-W1 is known as a representative supercritical shape can be found on most modern transport aircraft. Table 3 summarizes its reference quantities in order to calculate lift, drag, and moment coefficients.

Table 3 Reference quantities for DPW-W1.

$S_{ref}/2$ (mm^2)	C_{ref} (mm)	$b/2$ (mm)	AR	X_{ref} (mm)	Y_{ref} (mm)	Z_{ref} (mm)
145,161.0	197.556	762.0	8.0	6847.145	0.0	2226.615

In the DPW-III, the participants were required to provide computed results of the two problems. The first one was calculated at a fixed angle-of-attack (AOA, α) of design condition ($\alpha = 0.5$), and the second problem required drag polar at several proposed AOA. In this study, the design condition, which is summarized in Table 4, was considered for code validation.

Table 4 Freestream conditions for DPW-W1.

Mach Number	Temperature ($^{\circ}K$)	Angle-of-Attack (deg.)	Reynolds Number
0.76	322.22	0.5	5 millions

Because the participants of the workshop presented several types of grids used for verification, the flow solver could be validated with no interference from the grid generation, which meant that the DPW-W1 is very useful for code verification. Among the participants, Sclafani *et al.* [74] and Tinoco *et al.* [75] of the Boeing

Company provided a structured overset grid and a structured multi-block grid, respectively.

The flow analysis using multi-block grid was conducted before considering overset mesh technique. Tinoco *et al.* supports several sizes of grid, which are the coarse grid with a 1.6 million cells, the medium grid with 4.2 million cells, the medium fine grid with 8.6 million cells, and the fine grid with 14.7 million cells. In this study, the coarse grid and the medium grid were chosen because of the computational cost. Although the developed flow solver has a capability for large scale computing that has more than 20 million cells, the computational resource and the physical time for validation are hard to be support a problem that has more 5 million cells, practically. The wing shape and the schematic of the surface meshes are shown in Fig. 13.

The calculated performance coefficients of lift and drag were compared to the Tinoco's result, which is summarized in Table 5. As the size of grid became larger, the performance coefficients were converged to the actual solution. The coarse grid shows a much higher drag coefficient than that of the fine grid in both the calculated results of this study and the Tinoco's results. All of the calculations use $k-\omega$ SST-2003 two-equation model as a turbulence model.

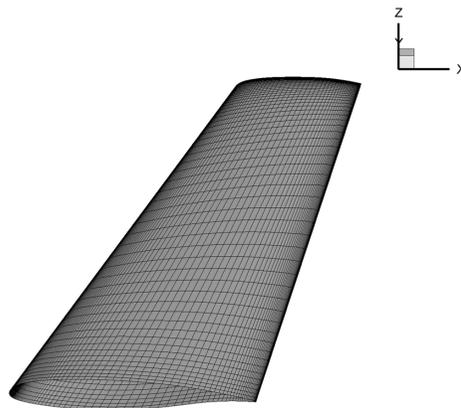


Figure 13 Shape and surface meshes of DPW-W1.

Table 5 Comparison of wing performance coefficients in multi-block.

Grid, Limiter	Lift coefficient	Drag coefficient	Moment coefficient
Coarse, Van Albada	0.46807	0.02106	-0.06713
Coarse, MLP 5	0.46762	0.02015	-0.06572
Medium, Van Albada	0.46788	0.02051	-0.06607
Fine, Tinoco	0.46245	0.01978	-0.06390

At the presentation of DPW-III, Tinoco said that the workshop should be renamed to the grid convergence workshop. It is a witticism illustrating that the accuracy of results is mainly dependent on the grid quality, and it is proved in the computed results shown above in Table 5, along with the results of DPW-III. Furthermore, the higher order solution created by using the MLP scheme on the coarse grid has better results than the solution of the MUSCL scheme with the medium grid, which also emphasizes the important of grid quality.

Figure 14 shows the pressure contour of the wing upper surface and wing section of $y/span = 50\%$. The graph of pressure coefficient at $y/span = 42\%$ is compared in Fig. 15.

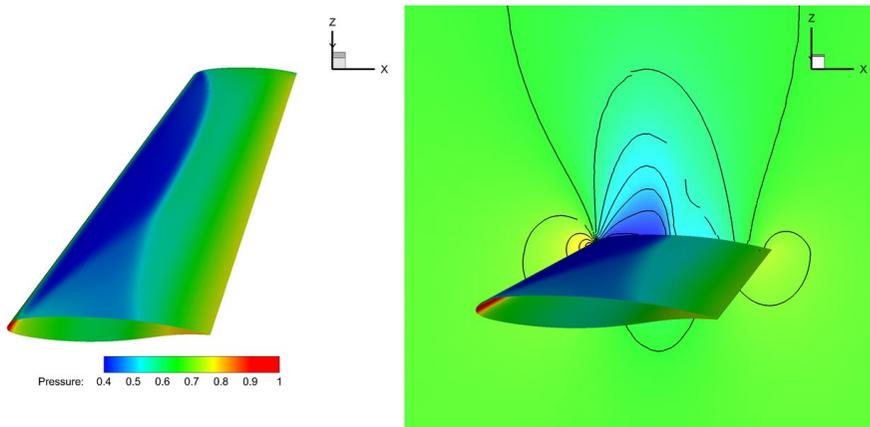


Figure 14 Pressure contour of DPW-W1 (Multi-block).

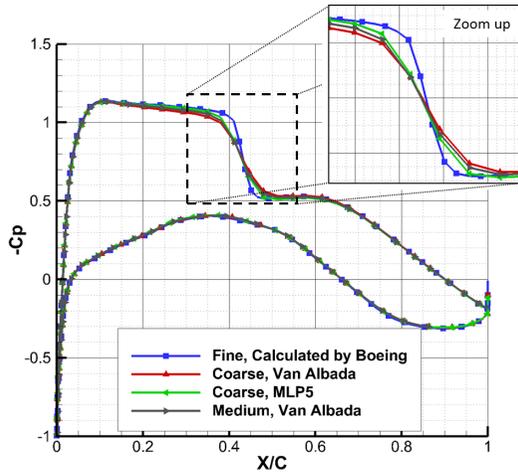


Figure 15 Pressure coefficient of DPW-W1 at $y/\text{span} = 42\%$ (multi-block).

To validate of the overset pre- and post-processor and to validate the flow solver, which has a complex overset connectivity structure, the DPW-W1 was considered once again with the overset grid supported by the Boeing Company, as mentioned above. Sclafani *et al.* provide several sizes of grids: the coarse grid with 1.5 million cells, the medium grid with 5 million cells, the fine grid with 16 million cells, and the extra fine grid with 55 million cells. In this validation case, only the coarse grid could be considered because of the same reason of computational cost that was mentioned above. Figure 16 shows the overall grid system that consisted of five blocks: a global box block, a wing box block, a wing block, a wing-tip block, and a trailing-edge block. Although Sclafani used the Spalart-Allmaras (SA) turbulence model, the validation was processed by $k-\omega$ SST-2003 turbulence model. As a higher order scheme, the MUSCL scheme was employed to preserve the convergence. The computed solution was compared to the result of Sclafani in Table 6.

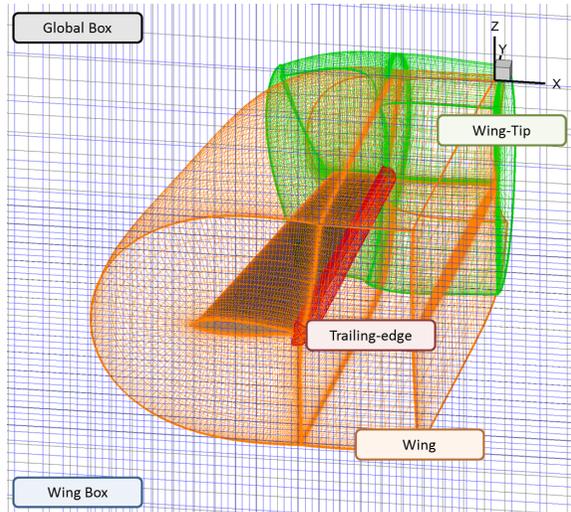


Figure 16 Overset grid system of DPW-W1.

Table 6 Comparison of wing performance coefficients in overset grid.

Grid	Lift coefficient	Drag coefficient	Moment coefficient
Coarse, Van Albada	0.46797	0.02246	-0.06999
Fine, Tinoco	0.48160	0.02021	-0.06822

Even if the drag coefficient is higher than the Tinoco's result, the calculated solution shows reasonable agreement with the other's results. One reason for the high drag coefficient is the grid quality, which is a similar characteristic of the multi-grid solver verification [74, 75].

Because this overset grid has the region where more than three blocks were overlapped together, the overlap optimization scheme was activated. The sub-cell TFI and the SBIG scheme were also used in this case to deal with the overlapped wall surface. The wing surface modified by SBIG scheme is shown in Fig. 17.

The pressure contour of the wing upper surface, which can be compared to that of multi-block grid, is presented in Fig. 18. Because a mesh treated by SBIG

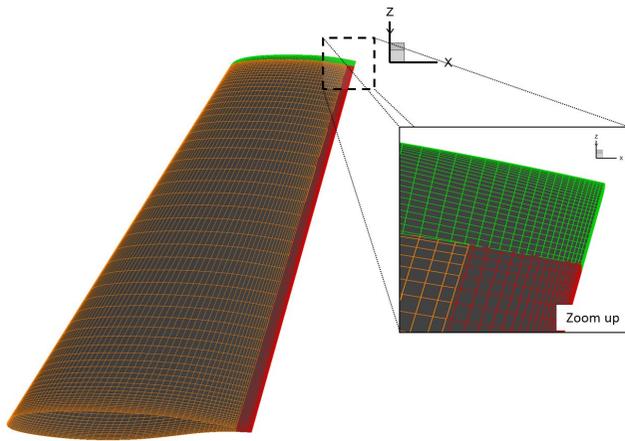


Figure 17 Reconstructed surface meshes of DPW-W1.

scheme does not have connectivity information between the cells, only one cell plots only one value and the cell values cannot be interpolated, which makes discontinuous contour in Fig. 18.

Figure 19 shows the comparison of the pressure coefficient of the wing section at $y/\text{span} = 42\%$.

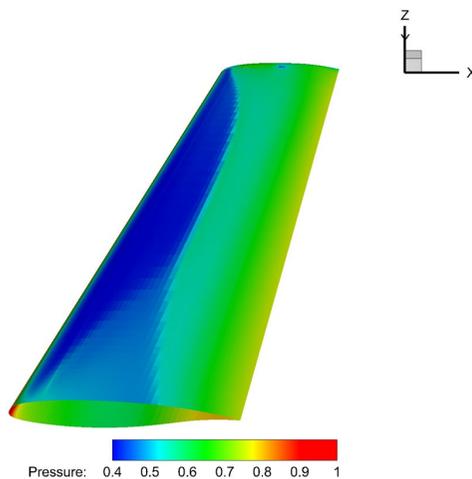


Figure 18 Pressure contour of DPW-W1 (overset).

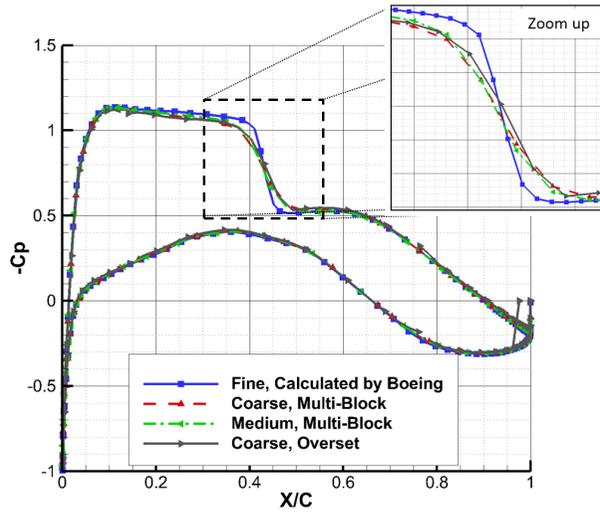


Figure 19 Pressure coefficient of DPW-W1 at $y/span = 42\%$ (overset).

These results proved that the present flow solver is well validated even in multi-block and overset grid system.

Chapter III

Sensitivity Analysis

3.1 Finite Difference Method

The sensitivity information is easily evaluated with two times of the flow analysis by the Finite Difference Method (FDM). The second order central differenced derivative given in Eq. 3.1 is widely used.

$$\frac{dF}{dx} = \frac{F(x + \Delta x) - F(x - \Delta x)}{\Delta x} \quad (3.1)$$

where F is an objective function, and x is a variable that is same as a design variable. Although the computational cost of this method is so high, twice the number of design variables times the consuming time of flow analysis, this method is still popularly used in the design optimization except in aerodynamic optimization problems.

3.2 Complex Step Derivative Method

The complex step derivative method proposed by Martins *et al.* can calculate accurate sensitivity information. For this reason, this method is widely applied to validate the other methods. The sensitivity of an objective function can be evaluated as follows:

$$\frac{dF}{dx} = \frac{\text{Im}(F(x+i\Delta x))}{\Delta x} \quad (3.2)$$

This equation can be derived by the Taylor series expansion for the objective function F , as follows:

$$F(x+i\Delta x) = F(x) + i \frac{dF(x)}{dx} \Delta x - \frac{d^2 F(x)}{dx^2} \frac{\Delta x^2}{2!} - i \frac{d^3 F(x)}{dx^3} \frac{\Delta x^3}{3!} + \dots \quad (3.3)$$

The first order derivative can be represented by

$$\text{Im}(F(x+i\Delta x)) = \frac{dF(x)}{dx} \Delta x + O(\Delta x^3) \quad (3.4)$$

This equation is the same as Eq. 3.2.

The complex step derivative method can be easily implemented by modifying the real variables of the flow solver to the complex form. Then the imaginary part of the variable x adopts a small perturbation in order to calculate the derivative with respect to the design variable; therefore, only one design variable can be considered at once providing the strongest reason why this method cannot be popularly applied to actual design problems. The perturbation value is generally less than 10^{-6} , and the value of 10^{-20} was used in this study.

The flow solver for real value is carefully modified to a complex form because some standard functions of FORTRAN, such as a minimum (min), a maximum (max), an absolute value (abs), a trigonometric function, and so forth, do not support the complex value, but Martines *et al.* provides the complexify code for these unsupported functions. For more information about this code, find the complexfy.f90 on the web or visit Martines's web-site [76].

3.3 Direct Differentiation Method

The direct differentiation method can be considered in both the continuous manner and the discrete manner. Because the Adjoint Variable (AV) method is considered in discrete manner in this study, the direct differentiation method was also derived in discrete manner.

The discrete residual of the discretized governing equation has to become zero when the flow solver converges to steady-state solution. Because the discrete residual is a function of the flow variable (Q), computational grid position (X), and the design variable (D), the discrete residual can be written as follows:

$$\{R\} = \{R(Q, X, D)\} = \{0\} \quad (3.5)$$

Similarly, the objective function (F) to be minimized or maximized is also dependent on these variables of Q , X , and D , as follows:

$$\{F\} = \{F(Q, X, D)\} \quad (3.6)$$

The sensitivity derivatives of the objective function are calculated by directly differentiating Eq. 3.6 with respect to D as follows:

$$\left\{ \frac{dF}{dD} \right\} = \left\{ \frac{\partial F}{\partial Q} \right\}^T \left\{ \frac{dQ}{dD} \right\} + \left\{ \frac{\partial F}{\partial X} \right\}^T \left\{ \frac{dX}{dD} \right\} + \left\{ \frac{\partial F}{\partial D} \right\} \quad (3.6)$$

The term of $\{dQ/dD\}$ represents the differentiation of flow variables with respect to the design variables, which is the sensitivity of flow variable. The term of $\{dX/dD\}$ represents the sensitivity of the grid position, and the derivatives of the grid position can be easily obtained by applying the shape modification functions, such as Hicks-Henne function, B-Spline function, Non-Uniform Rational B-Spline

(NURBS) function, and so forth, while the derivatives of flow variables cannot be simply evaluated because the flow variables are evaluated by the iterative calculation of the flow solver. The term of $\{dQ/dD\}$, therefore, can be acquired by the differentiated equations of discrete residual as follows:

$$\left\{ \frac{dR}{dD} \right\} = \left[\frac{\partial R}{\partial Q} \right] \left\{ \frac{dQ}{dD} \right\} + \left[\frac{\partial R}{\partial X} \right] \left\{ \frac{dX}{dD} \right\} + \left\{ \frac{\partial R}{\partial D} \right\} = \{0\} \quad (3.7)$$

This equation has an $Ax=B$ matrix form that can be calculated by the linear algebra or the time integration, which is similar to that of a flow solver. In the direct differentiation procedure, the calculation of Eq. 3.7 has to be carried out for all design variables. For this reason, the time cost of this method is also directly dependent on the number of design variables.

3.4 Discrete Adjoint Method

To avoid the direct calculation of the derivative of flow analysis with respect to the design variable $\{dQ/dD\}$, a vector of adjoint variables was introduced by Jameson [39]. Because the discrete residual of the governing equation, shown in Eq. 3.5, is zero, this equation can be added to the sensitivity analysis of the direct differentiate method by introducing the adjoint vectors (Λ), as follows:

$$\left\{ \frac{dF}{dD} \right\} = \left\{ \frac{\partial F}{\partial Q} \right\}^T \left\{ \frac{dQ}{dD} \right\} + \left\{ \frac{\partial F}{\partial X} \right\}^T \left\{ \frac{dX}{dD} \right\} + \left\{ \frac{\partial F}{\partial D} \right\} + \Lambda^T \left(\left[\frac{\partial R}{\partial Q} \right] \left\{ \frac{dQ}{dD} \right\} + \left[\frac{\partial R}{\partial X} \right] \left\{ \frac{dX}{dD} \right\} + \left\{ \frac{\partial R}{\partial D} \right\} \right) \quad (3.8)$$

The adjoint vector has seven elements: five elements are related to the conservative flow variables and two elements are related to the two-equation

turbulence model. By rearranging Eq. 3.8, the term of $\{dQ/dD\}$ can be organized as:

$$\begin{aligned} \left\{ \frac{dF}{dD} \right\} &= \left\{ \frac{\partial F}{\partial X} \right\}^T \left\{ \frac{dX}{dD} \right\} + \left\{ \frac{\partial F}{\partial D} \right\} + \Lambda^T \left(\left[\frac{\partial R}{\partial X} \right] \left\{ \frac{dX}{dD} \right\} + \left\{ \frac{\partial R}{\partial D} \right\} \right) \\ &+ \left(\left\{ \frac{\partial F}{\partial Q} \right\}^T + \Lambda^T \left[\frac{\partial R}{\partial Q} \right] \right) \left\{ \frac{dQ}{dD} \right\} \end{aligned} \quad (3.9)$$

If the last term of the above equation satisfies the following adjoint equation

$$\left[\frac{\partial R}{\partial Q} \right]^T \Lambda + \left\{ \frac{\partial F}{\partial Q} \right\} = \{0\}^T \quad (3.10)$$

the sensitivity derivatives of the objective function can be calculated without the necessity of evaluating the term of $\{dQ/dD\}$ by computing as follows:

$$\left\{ \frac{dF}{dD} \right\} = \left\{ \frac{\partial F}{\partial X} \right\}^T \left\{ \frac{dX}{dD} \right\} + \left\{ \frac{\partial F}{\partial D} \right\} + \Lambda^T \left(\left[\frac{\partial R}{\partial X} \right] \left\{ \frac{dX}{dD} \right\} + \left\{ \frac{\partial R}{\partial D} \right\} \right) \quad (3.11)$$

Because the adjoint equation of Eq. 3.10 also has the $\mathbf{Ax}=\mathbf{B}$ matrix form, several methods can be adopted for calculating the adjoint vector Λ , but the method that needs a large memory is hard to be adopted because the flux Jacobian $[\partial R/\partial Q]$ of the adjoint equation is a large banded matrix in the flow analysis. The solution, therefore, is generally obtained by solving the Euler implicit method of Eq. 3.10 time-iteratively with the implicit time integration method, such as the LU-SGS scheme.

The adjoint variable method is quite attractive because the required computational cost is almost independent of the number of design variables.

3.5 Overset Adjoint Boundary Condition

In calculating of the adjoint vector, the boundary cells have to be considered; thus, Eq. 3.10 is expressed on the boundary as follows:

$$\begin{aligned} \left[\frac{\partial R}{\partial Q} \right]^T \Lambda + \left[\frac{\partial R_B}{\partial Q} \right]^T \Lambda_B + \left\{ \frac{\partial F}{\partial Q} \right\} &= \{0\}^T \\ \left[\frac{\partial R}{\partial Q_B} \right]^T \Lambda + \left[\frac{\partial R_B}{\partial Q_B} \right]^T \Lambda_B + \left\{ \frac{\partial F}{\partial Q} \right\} &= \{0\}^T \end{aligned} \quad (3.12)$$

The subscript B represents the boundary cell in discretized consideration.

Unlike the basic boundary condition, the overset adjoint boundary condition can be obtained as follows [5-7]:

$$\left[\frac{\partial R^M}{\partial Q^M} \right]^T \Lambda^M + \left[\frac{\partial R_F^S}{\partial Q^M} \right]^T \Lambda_F^S + \left\{ \frac{\partial F^M}{\partial Q^M} \right\} = \{0\}^T \quad (3.13)$$

$$\left[\frac{\partial R^S}{\partial Q^S} \right]^T \Lambda^S + \left[\frac{\partial R_F^M}{\partial Q^S} \right]^T \Lambda_F^M + \left\{ \frac{\partial F^S}{\partial Q^S} \right\} = \{0\}^T \quad (3.14)$$

$$\left[\frac{\partial R^M}{\partial Q_F^M} \right]^T \Lambda^M + \left[\frac{\partial R_F^M}{\partial Q_F^M} \right]^T \Lambda_F^M + \left\{ \frac{\partial F^M}{\partial Q_F^M} \right\} = \{0\}^T \quad (3.15)$$

$$\left[\frac{\partial R^S}{\partial Q_F^S} \right]^T \Lambda^S + \left[\frac{\partial R_F^S}{\partial Q_F^S} \right]^T \Lambda_F^S + \left\{ \frac{\partial F^S}{\partial Q_F^S} \right\} = \{0\}^T \quad (3.16)$$

where the subscript F indicates the fringe cell, and the superscripts M and S represent the main-grid and sub-grid block, respectively. By solving these four equations sequentially, the overset boundary value on the main- and sub-grids can be updated. For the sub-grid block, the adjoint vector on the fringe cell value of the

main-grid (Λ_F^M) is first updated from the inner cell value of the main-grid (Λ^M) as in Eq. 3.15. The inner cell value of the sub-grid (Λ^S) is then updated from the fringe cell value of the main-grid (Λ_F^M) as in Eq. 3.14. For the main-grid block, the adjoint vector on the fringe cell value of the sub-grid (Λ_F^S) is updated by Eq. 3.16, and then the inner cell value of the sub-grid (Λ^M) is calculated by using Eq. 3.13. The update procedure of the adjoint vector on the overset boundary is reverse to that of the flow analysis because of the transposed operation of the adjoint formulation.

3.6 BFGS method

After calculating the sensitivity information of the objective function, the optimization process is advanced as follows:

$$D^q = D^{q-1} + \alpha^* S^q \quad (3.17)$$

where D is set of design variable, α is scalar move parameter, q is the iteration number, and S^q is a vector of the search direction. The overall optimization process proceeds in following three steps: (1) Find a usable search direction, (2) Find the scalar parameter that will minimize $F(D^{q-1} + \alpha S^q)$, (3) Test the convergence to the optimum and terminate if convergence is achieved.

In the case of unconstrained minimization, the BFGS method [77, 78], named for its discoverers Broyden, Fletcher, Goldfarb, and Shanno, is a popular way to calculate a search direction for solving nonlinear optimization problems. The BFGS method is classified to a quasi-Newton method because it creates an approximation to the inverse of the Hessian matrix H , the matrix including the second derivatives of the objective function. Initially, H is set to the identity matrix I , so that the first search direction is the same as the direction calculated by the steepest descent

method.

The search direction is defined by using the BFGS method as

$$S^q = -H\nabla F(D^{q-1}) \quad (3.18)$$

After the first iteration, the Hessian matrix is updated by using the formula of

$$H^{q+1} = H^q + B^q \quad (3.19)$$

where

$$B^q = \left(\frac{\sigma + \tau}{\sigma^2} \right) pp^T - \frac{1}{\sigma} \left[H^q yp^T + p(H^q y)^T \right]$$

$$\sigma = p^T y, \quad \tau = y^T H^q y$$

The change vectors of p and y are defined as;

$$p = D^q - D^{q-1} \quad (3.20)$$

$$y = \nabla F(D^q) - \nabla F(D^{q-1}) \quad (3.21)$$

This method is considered to be theoretically good, but requires significant memory to store the Hessian matrix. The value of α is then found, which makes the $F(D^{q-1} + \alpha S^q)$ to minimize.

By adopting the search direction and the scalar parameter, the optimizer tries to find the optimum value by changing the design variables. Basically, four flow solutions are obtained for one sensitivity analysis. If the possibilities of the improvement are remained, the additional flow analyses are conducted until the objective function lost the possibilities. When no improvement can be found, new sensitivity information is obtained and a new search direction is then calculated. If still no improvement can be found, the optimizer regards that the optimization process is finished.

Chapter IV

Vortex Generator

4.1 BAY Model

As a mathematical source term to model a VG, the BAY model is employed as follows:

$$\Delta V_i \frac{\Delta \rho u_i}{\Delta t} = \sum_j F_M \Delta S + L_i \quad (4.1)$$

$$\Delta V_i \frac{\Delta \rho e_i}{\Delta t} = \sum_j F_e \Delta S + u_i \cdot L_i \quad (4.2)$$

where L_i is the source term representing the lift force of the VG. Equation 4.1 is the momentum equation and Eq. 4.2 is the energy equation. The flux summation along the boundary of the cell i is represented by j . Because the local flow direction becomes parallel to the VG, the energy source term of $u_i \cdot L_i$ in Eq. 4.2 disappears. The lift force (L_i) can be expressed as a correction term for the loss caused by the deviated flow from the VG surface as follows:

$$L_i = C_{VG} S_{VG} \left(\frac{\Delta V_i}{\sum_j \Delta V_j} \right) \alpha_{VG} \rho |\bar{u}|^2 \hat{l} \quad (4.3)$$

where \hat{l} is a unit vector of the lift force, C_{VG} is a relaxation parameter controlling the strength of the side force, and S_{VG} is the VG planform area. The percentage of the lift force of the ΔV_i (the volume of the cell i) is represented by $\Delta V_i / \sum_j \Delta V_j$, with

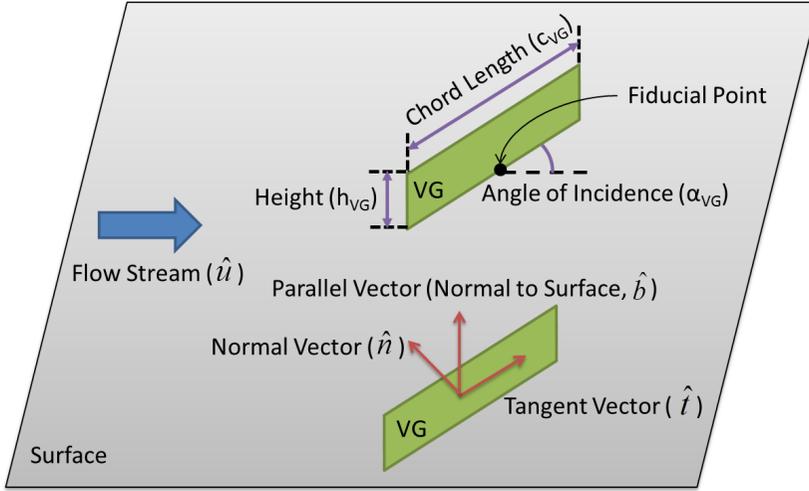


Figure 20 Directional definition of vortex generator.

$\Sigma_j \Delta V_j$ being the volume of all cells to which the VG is applied. The angle of incidence with respect to the flow direction is represented by the α_{VG} , ρ is the local density, and \vec{u} is the local velocity. The value of the C_{VG} should be more than five for an accurate solution, and the computed results are similar if it is greater than seven [17]. The unit vector of the VG is identified with three directions, as illustrated in Fig. 20.

The unit vector in the spanwise direction of the VG is represented by \hat{b} , \hat{i} is the unit vector tangent to the VG, and \hat{n} is the unit vector normal to the VG. Because Eq. 4.3 is difficult to implement into the discretized equations, the unit vector and the angle of incidence are modified by a small angle approximation as follows:

$$\hat{i} = \vec{u} / |\vec{u}| \times \hat{b} = \hat{u} \times \hat{b} \quad (4.4)$$

$$\alpha_{VG} \approx \sin \alpha_{VG} = \cos \left(\frac{\pi}{2} - \alpha_{VG} \right) = \vec{u} \cdot \hat{n} / |\vec{u}| = \hat{u} \cdot \hat{n} \quad (4.5)$$

To make up for the loss of the side force caused by a high angle of attack in a

small angle approximation, the $\frac{\vec{u} \cdot \hat{t}}{|\vec{u}|} = \hat{u} \cdot \hat{t}$ term is included. The final source term is then given by

$$L_i = C_{VG} S_{VG} \left(\frac{\Delta V_i}{\sum_j \Delta V_j} \right) \rho |\vec{u}|^2 (\hat{u} \times \hat{b})(\hat{u} \cdot \hat{n})(\hat{u} \cdot \hat{t}) \quad (4.6)$$

where \hat{u} is the unit velocity vector.

4.2 Differentiable BAY Model

From the view point of flow sensitivity, the original BAY model needs to be modified because it is formulated with the whole volume of each computational cell (Eqs. 4.3 and 4.6) that is crossed by the VG; thus it cannot reflect a small amount of positional change within the computational cell. Figure 21 shows the volume consideration of the BAY model for the percentage of the lift force ($\Delta V_i / \sum_j \Delta V_j$). The solid-lined VG and the broken-lined VG shown in Fig. 22 are treated as the same VG (or the same $\Delta V_i / \sum_j \Delta V_j$) in computational analysis although their actual positions are different. Moreover, it is difficult, with the BAY model, to obtain the gradient information at an interface, such as the slashed cell-interface in Fig. 22, between the cell where the VG is crossed and the one not crossed, or cells (a) and (b) in Fig. 22, which is caused by the discontinuous source term value.

A new differentiable BAY model is, therefore, developed by taking into account a small positional change, or equivalently a small volume change, which is going to provide more accurate sensitivity information for gradient evaluation. Figure 23 shows the differentiable BAY model, which is realized by replacing the whole volume of each cell crossed by the VG with the overlaid VG volume. By projecting the VG into each cell interface, the length of the intersected lines ($\Delta \xi^z$, $\Delta \eta$) is

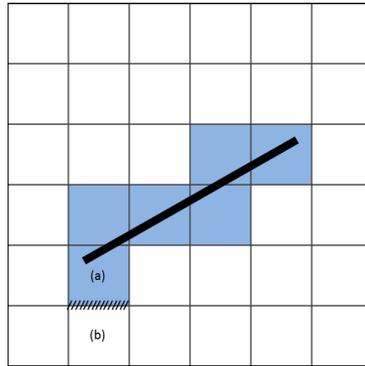


Figure 21 Volume calculation of BAY model.

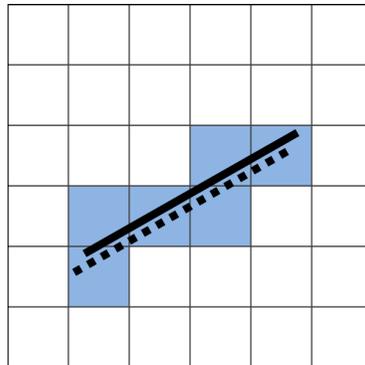


Figure 22 Limitation of BAY model in small positional change.

calculated, and then used to obtain the overlaid VG area or volume. The volume taken by the VGs hardly can be zero in general mesh systems. If the local grids perfectly align with the VGs, however, the volume terms of the differentiable BAY model may approach zero. This problem can be sidestepped by introducing a thin “virtual” thickness of the VG (ϵ in Fig. 24) to make $\Delta V_i / \Sigma_j \Delta V_j$ non-zero. So long as the “virtual” thickness of the VG is thin enough when compared to the characteristic length of the computational cell, the problem caused by the grid-aligned VGs can be properly cured because $\Delta V_i / \Sigma_j \Delta V_j$ is independent of ϵ and this term represents only a percentage of the VG lift force. This cure may not be complete because the virtual thickness of VG does not include the change of $\partial L_i / \partial \beta_{VG}$ or Eq. 4.25.

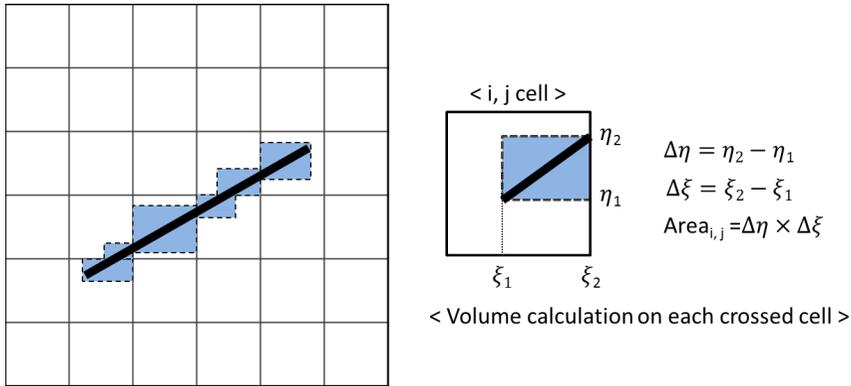


Figure 23 Volume calculation of differentiable BAY model.

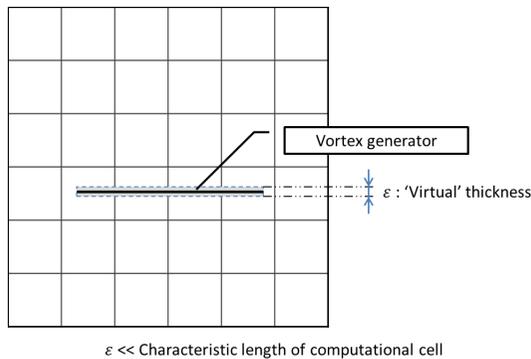


Figure 24 Virtual thickness of vortex generator for differentiable BAY model.

The resulting expression for the lift force is the same as that in the original BAY model.

Because the BAY model and the differentiable BAY model were derived from small angle approximation, the BAY type models have intrinsic limitation on the available angle of incidence of the VG even if the mathematical model includes the supporting term for the loss of the side force by high angle of attack. To check the compatible range of these models, the comparison between the fully gridded analysis and the flow analysis using source term model for the single VG on a flat plate was conducted, and this result is presented in Appendix B. From the result of the comparison, it is confirmed that the BAY type models are acceptable in the range from -30° to 30° .

4.3 Design Strategy Using VG Source Term Model

A VG can be optimized in several ways by using the gradient based or non-gradient based optimization methodologies. Basically, the rectangular type of the VG is considered for design with five design parameters of chord length (C_{VG}), height (h_{VG}), angle of incidence (α_{VG}), x -directional position (X_{VG}), and relative y - or z -directional position (β_{VG}), all of which are the components of the VG source term model. The number of installed VGs is also considered as an essential parameter although this variable cannot be treated by the GBOM. More complex shapes of the VG, such as a curved shape, a triangular shape, and other shapes, can be applied from now on because the differentiable BAY model reflects the shape complexity within a cell.

Much previous research on the VG design has been conducted, but all of the research applied only to the DOE-based design because of its simplicity. One of the known limitations of the DOE-based design, however, is the lack of flexibility in the number of design variables; thus, the same design condition was imposed on all VGs in the previous studies. Although these studies presented reasonable results by applying only few design variables, the results were impossible to fully reflect the local flow pattern near each VG. Each VG, therefore, must be independently handled for true optimal conditions by adopting adjoint-based sensitivity analysis that can treat a large number of design variables. Both the original BAY model and the developed differentiable BAY model are applied to obtain the sensitivity information in the proposed design framework. The design approach by using the original BAY model, however, has some limitations in that it cannot treat two parameters related to the position of the VG because of the limitation of the BAY model as mentioned in Chapter I. The sensitivity information with respect to the other parameters of chord length, height, and angle of incidence can be calculated in the BAY model without the derivative with respect to the volume.

The total number of design variables, therefore, are five or three, or the number of design parameters of each VG, times of the number of VGs, which depends on the source term model and the type of the VG shape. For example, if the VG shape is changed to more complex one, the number of design parameters related to the shape increases. The design of the number of installed VGs should be ignored in the design process using GBOM because of its step-formed characteristics; therefore, the number of VGs is always decided before the optimization process. The baseline of the VG, which has to be closed to the optimum to overcome the limitation of GBOM, also has to be defined before the design.

It is better to consider the baseline of design from the results obtained by the DOE-based design imposing the same design condition to all of the VGs. This result also must include the number of VGs. If this consideration is not possible, the baseline of the design can be determined through the parametric studies that also include the number of VGs. Although the process for selection of the baseline needs extra design time, this step may decrease the possibilities that the optimized result is trapped in a local optimum.

4.4 Sensitivity Analysis with Differentiable BAY Model

As mentioned in Chapter III, the sensitivity derivatives of objective function can be calculated by Eq. 4.7, which is the same as Eq. 3.11.

$$\left\{ \frac{dF}{dD} \right\} = \left\{ \frac{\partial F}{\partial X} \right\}^T \left\{ \frac{dX}{dD} \right\} + \left\{ \frac{\partial F}{\partial D} \right\} + \Lambda^T \left(\left[\frac{\partial R}{\partial X} \right] \left\{ \frac{dX}{dD} \right\} + \left\{ \frac{\partial R}{\partial D} \right\} \right) \quad (4.7)$$

The adjoint vector (Λ) is calculated by the adjoint equation of Eq. 4.8, which is the same as Eq. 3.10.

$$\left[\frac{\partial R}{\partial Q} \right]^T \Lambda + \left\{ \frac{\partial F}{\partial Q} \right\} = \{0\}^T \quad (4.8)$$

When the BAY type source term models are applied to the flow and sensitivity analyses, the residual includes the VG source term. The derivatives of residual, therefore, are as follows:

$$\left\{ \frac{\partial R}{\partial D} \right\}^T = \left\{ \frac{\partial}{\partial D} \left(\sum_j Flux + L_i \right) \right\}^T \quad (4.9)$$

$$\left[\frac{\partial R}{\partial Q} \right]^T = \left[\frac{\partial}{\partial Q} \left(\sum_j Flux + L_i \right) \right]^T \quad (4.10)$$

When the design is performed by the proposed design strategy that uses the VG source term model, the presented objective function for the VG design (F) is independent of the computational mesh (X), numerical flux, and the design variables (D); therefore, the sensitivity of the objective function is finally calculated as:

$$\left\{ \frac{dF}{dD} \right\} = \Lambda^T \left\{ \frac{\partial R}{\partial D} \right\} = \Lambda^T \left\{ \frac{\partial L_i}{\partial D} \right\} \quad (4.11)$$

The derivatives of the lift force with respect to the flow variables for Eq. 4.10 are calculated as follows:

$$\left\{ \frac{\partial L_i}{\partial Q} \right\}^T = \left(\left[\frac{\partial L_i}{\partial Q_p} \right] \left[\frac{\partial Q_p}{\partial Q} \right] \right)^T = \left[\frac{\partial Q_p}{\partial Q} \right]^T \left[\frac{\partial L_i}{\partial Q_p} \right]^T = \mathbf{M}^{-1T} \left[\frac{\partial L_i}{\partial Q_p} \right]^T \quad (4.12)$$

The result from differentiating L_i with respect to the primitive variable vector Q_p is

$$\left[\frac{\partial L_i}{\partial \rho} \right] = C_{VG} S_{VG} \left(\frac{\Delta V_i}{\sum_j \Delta V_j} \right) |\vec{u}|^2 (\hat{u} \times \hat{b})(\hat{u} \cdot \hat{n})(\hat{u} \cdot \hat{t}) \quad (4.13)$$

$$\left[\frac{\partial L_i}{\partial u_i} \right] = C_{VG} S_{VG} \left(\frac{\Delta V_i}{\sum_j \Delta V_j} \right) \rho |\vec{u}|^2 \times \left(\begin{aligned} & \frac{\partial(\hat{u} \times \hat{b})}{\partial u_i} (\hat{u} \cdot \hat{n})(\hat{u} \cdot \hat{t}) + (\hat{u} \times \hat{b}) \frac{\partial(\hat{u} \cdot \hat{n})}{\partial u_i} (\hat{u} \cdot \hat{t}) \\ & + (\hat{u} \times \hat{b})(\hat{u} \cdot \hat{n}) \frac{\partial(\hat{u} \cdot \hat{t})}{\partial u_i} \end{aligned} \right) \quad (4.14)$$

$$\left[\frac{\partial L_i}{\partial p} \right] = 0 \quad (4.15)$$

$$\left[\frac{\partial L_i}{\partial k} \right] = 0 \quad (4.16)$$

$$\left[\frac{\partial L_i}{\partial \omega} \right] = 0 \quad (4.17)$$

Also, differentiating the VG directional vectors is given by

$$\frac{\partial(\hat{u} \times \hat{b})}{\partial u} = (\hat{b}_2 \cdot v - \hat{b}_3 \cdot w) / c, \quad c = \sqrt{u^2 + v^2 + w^2} \quad (4.18)$$

$$\frac{\partial(\hat{u} \cdot \hat{n})}{\partial u} = \hat{n} / c \quad (4.19)$$

$$\frac{\partial(\hat{u} \cdot \hat{t})}{\partial u} = (\hat{t}_1 \cdot c - u(\hat{u} \cdot \hat{t})) / c \quad (4.20)$$

Subscripts 1, 2, 3 in Eqs. 4.18 and 4.20 indicate the x -, y -, z -directional component of the unit vector.

Next, the derivatives of the lift force with respect to the design parameters can be expressed as follows:

$$\left[\frac{\partial L_i}{\partial c_{VG}} \right] = C_{VG} \left(h_{VG} \left(\frac{\Delta V_i}{\sum_j \Delta V_j} \right) + S_{VG} \left(\frac{\partial \left(\frac{\Delta V_i}{\sum_j \Delta V_j} \right)}{\partial c_{VG}} \right) \right) \times \rho |\vec{u}|^2 (\hat{u} \times \hat{b})(\hat{u} \cdot \hat{n})(\hat{u} \cdot \hat{t}) \quad (4.21)$$

$$\left[\frac{\partial L_i}{\partial h_{VG}} \right] = C_{VG} \left(c_{VG} \left(\frac{\Delta V_i}{\sum_j \Delta V_j} \right) + S_{VG} \left(\frac{\partial \left(\frac{\Delta V_i}{\sum_j \Delta V_j} \right)}{\partial h_{VG}} \right) \right) \times \rho |\vec{u}|^2 (\hat{u} \times \hat{b})(\hat{u} \cdot \hat{n})(\hat{u} \cdot \hat{t}) \quad (4.22)$$

$$\left[\frac{\partial L_i}{\partial \alpha_{VG}} \right] = C_{VG} S_{VG} \left(\frac{\Delta V_i}{\sum_j \Delta V_j} \right) \rho |\vec{u}|^2 \times \left(\frac{\partial(\hat{u} \times \hat{b})}{\partial \alpha_{VG}} (\hat{u} \cdot \hat{n})(\hat{u} \cdot \hat{t}) + (\hat{u} \times \hat{b}) \frac{\partial(\hat{u} \cdot \hat{n})}{\partial \alpha_{VG}} (\hat{u} \cdot \hat{t}) + (\hat{u} \times \hat{b})(\hat{u} \cdot \hat{n}) \frac{\partial(\hat{u} \cdot \hat{t})}{\partial \alpha_{VG}} \right) \quad (4.23)$$

$$+ C_{VG} S_{VG} \left(\frac{\partial \left(\frac{\Delta V_i}{\sum_j \Delta V_j} \right)}{\partial \alpha_{VG}} \right) \times \rho |\vec{u}|^2 (\hat{u} \times \hat{b})(\hat{u} \cdot \hat{n})(\hat{u} \cdot \hat{t})$$

$$\left[\frac{\partial L_i}{\partial X_{VG}} \right] = C_{VG} S_{VG} \left(\frac{\partial \left(\frac{\Delta V_i}{\sum_j \Delta V_j} \right)}{\partial X_{VG}} \right) \rho |\vec{u}|^2 (\hat{u} \times \hat{b})(\hat{u} \cdot \hat{n})(\hat{u} \cdot \hat{t}) \quad (4.24)$$

$$\left[\frac{\partial L_i}{\partial \beta_{VG}} \right] = C_{VG} S_{VG} \left(\frac{\partial \left(\frac{\Delta V_i}{\sum_j \Delta V_j} \right)}{\partial \beta_{VG}} \right) \rho |\vec{u}|^2 (\hat{u} \times \hat{b})(\hat{u} \cdot \hat{n})(\hat{u} \cdot \hat{t}) \quad (4.25)$$

It is noted that the differentiable BAY model can provide the sensitivity of the VG position by a smooth change in the volume term at each cell. Equations 4.24 and 4.25, however, cannot be calculated by using the BAY model because the derivative of the volume term disappears.

Chapter V

RAE M2129 S-Duct

At first, the Royal Aircraft Establishment intake Model 2129 (RAE M2129) was considered an internal flow application.

5.1 RAE M2129 S-shape Subsonic Offset Inlet

5.1.1 Geometric Information

The geometry used for flow analysis and design optimization is the RAE M2129, an S-shaped diffusing subsonic offset inlet (S-duct) in which a strong flow separation is observed on the starboard side. RAE M2129 geometry was introduced by the AGARD group in the 1990s [50]. The inlet geometry consists of a circular inlet entrance section, a constant cross sectional region located after the engine face plane, and a smooth S-bend diffuser of a circular cross section connecting the inlet entrance section and the engine face plane. The S-bend diffuser has two bends, and its cross-sectional area increases along the centerline of the S-duct. The non-dimensional length of the inlet entrance radius (R_{in}) is 1.0, the radius of the engine face (R_{ef}) is 1.183, the length of the diffusing section (L) is 7.1, and the gap of the centerline between the inlet entrance and the engine face (ΔZ_{cl}) is 2.13. The length of the remaining region 1 (from the starting point of the inlet to the starting point of the diffusing section) is 2.2, and the length of the remaining region 2 (from the end point of the diffusing section to the outlet boundary) is 3.8. All numbers are normalized with respect to the throat radius (*i.e.*, the radius of inlet entrance). The offset of the centerline (Z_{cl}) and the variation of the radius in the diffusing part of

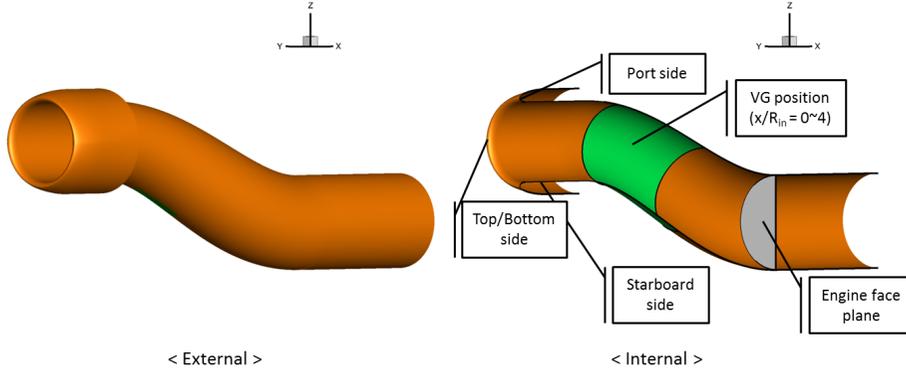


Figure 25 Geometric schematic of the RAE M2129.

the inlet (R_d) can be defined by the following two equations:

$$Z_{cl} = \Delta Z_{cl} \left[1 - \cos \left(\pi \frac{x_{cl}}{L} \right) \right] \quad (5.1)$$

$$\left(\frac{R_d - R_{in}}{R_{ef} - R_{in}} \right) = 3 \left(1 - \frac{x_{cl}}{L} \right)^4 - 4 \left(1 - \frac{x_{cl}}{L} \right)^3 + 1 \quad (5.2)$$

The geometric schematic of the RAE M2129 is shown in Fig. 25. While the actual S-duct has an engine shaft and a shaft cap, these are typically implemented as the boundary condition of the flow exit [49].

5.1.2 Performance Coefficients for Subsonic Inlet

The performance of the subsonic inlet can be measured by the total pressure recovery ratio and the engine face distortion coefficient. The total pressure recovery ratio, as shown in Eq. 5.3, is defined by the ratio of the average total pressure on the engine face to that on the inlet entrance. The engine face distortion coefficient, as given in Eq. 5.4, represents the flow non-uniformity at the engine face. All the circumferential angles (θ) in Eq. 5.5 are evaluated at the engine face section; therefore, the performance coefficients are calculated as

$$PR = \bar{p}_{t,ef} / \bar{p}_{t,in} \quad (5.3)$$

$$DC\theta = \max[\bar{p}_t - \bar{p}_t(\theta)] / \bar{q} \quad (5.4)$$

$$\bar{p}_t = \frac{\int_A P_t dA}{\int_A dA}, \quad \bar{p}_t(\theta) = \frac{\int_\theta P_t d\theta}{\int_\theta d\theta}, \quad \bar{q} = \frac{\int_A q dA}{\int_A dA} \quad (5.5)$$

where p_t is the total pressure, q is the dynamic pressure, \int_θ indicates integration over an angular domain, \int_A indicates integration over the entire cross sectional area A, and DC θ is the normalized maximum positive difference between \bar{p}_t and $\bar{p}_t(\theta)$ for all possible angular domains. During design process, the objective is to minimize the engine face distortion coefficient while maintaining the total pressure recovery ratio.

5.1.3 Previous Vortex Generator Study in an S-Duct

Anderson and Gibb [60] presented a matrix of CFD-designed VG installations (see Table 7) through computational analysis with the BAY model and experimental tests. This matrix includes detailed VG conditions, such as chord length and height, and the angle of incidence, number, location, and spacing of the VGs. They designed VG configurations named VG160, VG165, and VG170, which configurations were optimally determined with respect to some parameters. The baseline VG configuration of the present study was selected from these configurations, the VG170. This configuration was optimally designed with respect to the VG height which is known as one of the most sensitive design parameters. Furthermore, the VG170 configuration yields minimal distortion coefficient, among the four configurations, on the high-mass-flow-rate condition (see Table 8).

Table 7 Matrix of CFD-Designed Vortex Generator Installations.

Designation	VG130	VG160	VG165	VG170
Number of pairs (n_{VG})	11	13	11	11
Sector location (X_{VG}/R_i)	3.0	1.0	1.0	2.0
Blade height (h_{VG}/R_i)	0.075	0.060	0.065	0.070
Chord length (c_{VG}/R_i)	0.300	0.240	0.260	0.280
Lateral spacing (d/R_i)	0.289	0.224	0.267	0.277
Spacing angle (β_{VG} [deg.])	15.0	12.6	15.0	15.0
Angle of incidence (α_{VG} [deg.])	16.0	16.0	16.0	16.0
Sector angle (θ_{VG} [deg.])	157.5	157.5	157.5	157.5

5.2 Flow Analysis and Flow Solver Verification

Flow analyses of the S-duct are based on the AGARD test case 3.1 [50]. From the flow conditions presented by the AGARD group, the high mass flow rate (HMFR) case is selected because it yields more complicated and significant flow characteristics than the low mass flow rate (LMFR) case. Table 8 shows the HMFR condition. Prior to the design process, the present flow solver with/without the VG source term model was validated by comparing the computed results with experimental data. The results of the analyses to the BAY model and to the differentiable BAY model were also compared. In addition, the grid refinement test was conducted to obtain an optimal grid density without compromising solution accuracy.

Table 8 High Mass Flow Rate (HMFR) Condition of RAE M2129.

Test Case 3.1 (DP 3532)	
Total pressure	$H_0 = 29.889$ in Hg
Total temperature	$T_{t0} = 293$ °K
Flight Mach number	$M_0 = 0.210$
Throat Mach number	$M_{th} = 0.794$
Non-dimensional weight flow	$WAT_{cf} = 0.311 \left(in^2 \sqrt{^\circ K} \right) / sec$
Compressor face Mach number (Engine face Mach number)	$M_{cf} = 0.530$
Pressure recovery	$PR = 0.928$
Capture flow ratio	$A_0/A_c = 2.173$
Capture area	$A_c = 25.245$ in ²

5.2.1 Grid Topology and Boundary Condition

The structured multi-block grid system is composed of 51 radial node points, 37 circumferential node points, and 321 axial node points for the half duct, a total number of grids of 576,000 (coarse grid). Figure 26 shows the overall grid distribution and approximate range of the VG position. A grid refinement test is carried out on three levels. The medium grid has 51 x 73 x 321 node points (1 million cells), and the fine grid has 51 x 181 x 321 node points (3 million cells).

According to the studies by Menzies [49], Lee and Kim [57], and other researchers, constant static pressure is applied as the inlet exit boundary condition. The condition at the inlet entrance is the total state inflow boundary condition defined by the total pressure and total temperature. The entrance and exit boundaries should control the mass flow rate and throat Mach number.

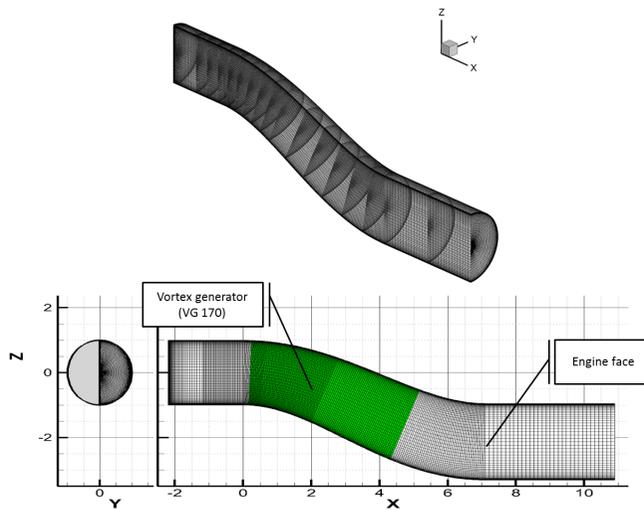


Figure 26 Overall grid distribution.

5.2.2 Validation of Flow Solver with the Source Term Model

Prior to the design process, the present flow solver was validated by comparing the computed results of the S-duct with/without the VG170 configuration to the experimental data of the DRA/Bedford 13 x 9 *ft.* wind tunnel test conducted by Anderson and Gibb [60]. The flow solver with/without the original BAY model was successfully validated, and the results are presented in Figs. 27-32. In Figs. 27 and 28, the distortion coefficient and the total pressure recovery ratio are compared and show that the present results agree very well with experimental data. The similarity of the flow pattern between the computed results and the experimental data is also quite good in the sense that flow separations on the starboard and port sides are well captured. The results of the grid refinement test are also presented in Figs. 27 and 28, which indicate that all the three grid systems provide reasonably good agreements with experimental data. The coarse grid system was thus adopted for an efficient design.

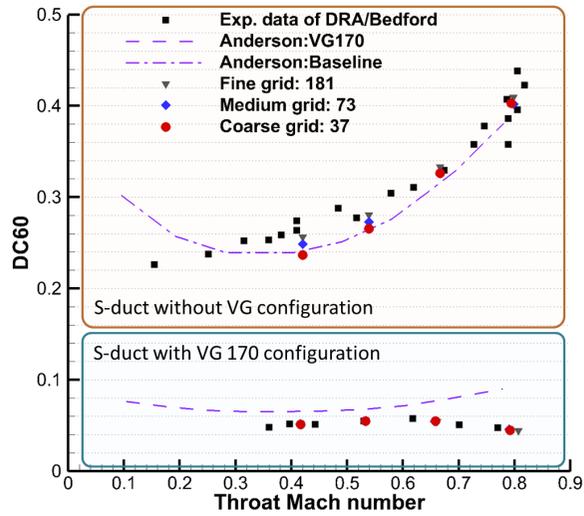


Figure 27 Validation of flow solver with/without BAY model (distortion coefficient).

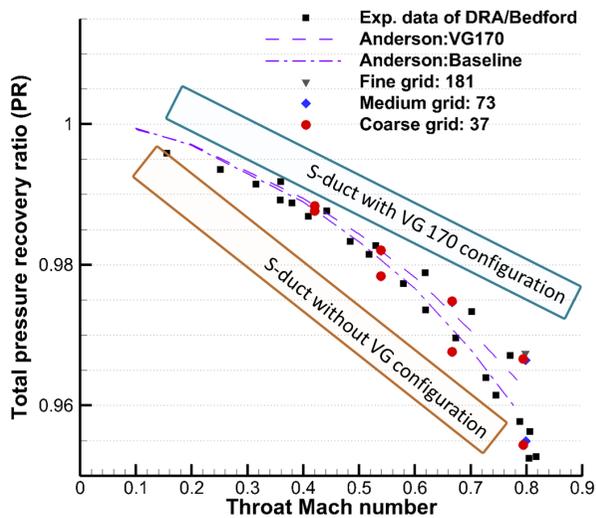


Figure 28 Validation of flow solver with/without BAY model (total pressure recovery ratio).

Figure 29 illustrates the streamlines of the S-duct without the VG and shows the flow pattern of the circulatory flow and secondary flow. After the installation of the VG, the flow directions are properly controlled into the parallel direction of the VG as shown in Fig. 30. Figure 30 also shows the overall position of the VG170 configuration (VG1 on the starboard side to VG11 on the port side), and Figs. 31 and 32 provide the total pressure recovery distributions along the S-duct with/without the VG170 configuration. The flow distortion grows because of the secondary flow without the VG configuration in Fig. 31, while the distortion on the starboard side is eliminated by the VG170 as shown in Fig. 32.

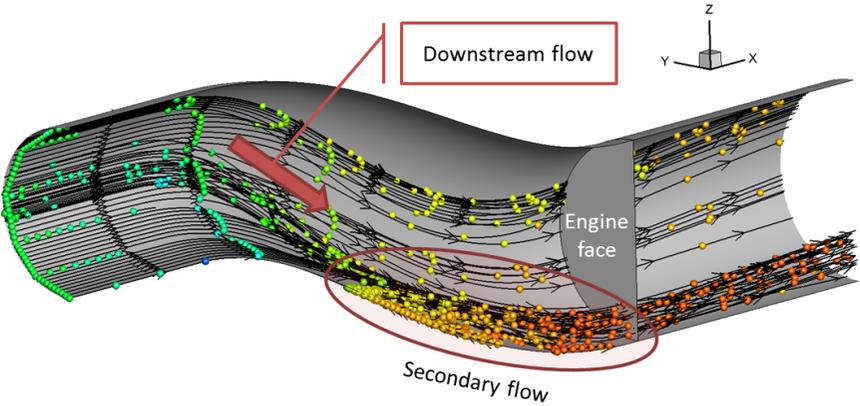


Figure 29 Flow pattern of S-duct without vortex generator.

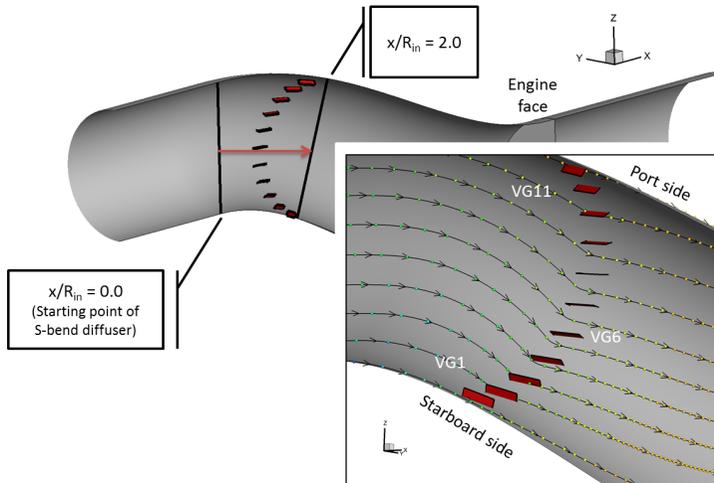


Figure 30 Position of VG170 configuration and flow pattern near vortex generators.

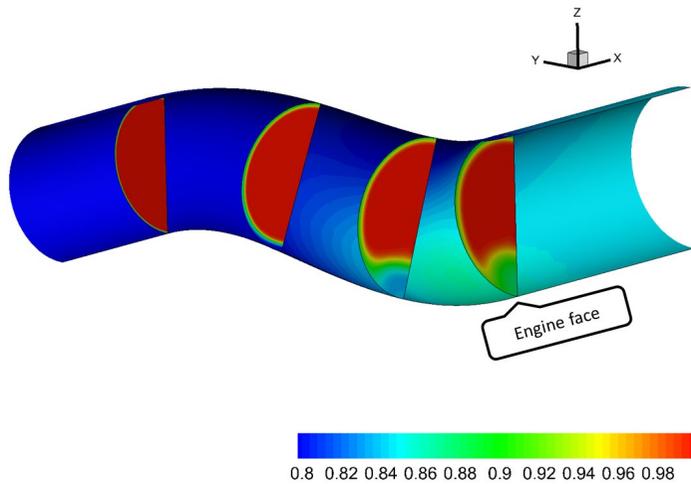


Figure 31 Total pressure recovery contour along S-duct without VG configuration.

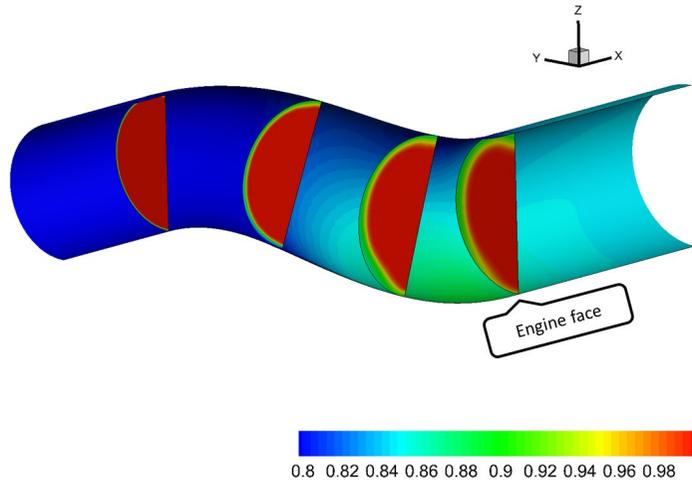


Figure 32 Total pressure recovery contour along S-duct with VG170 configuration.

The flow solver with the differentiable BAY model was also successfully validated. Figure 33 shows the distortion comparison graph, and Fig. 34 compares the total pressure recovery ratio. Both results demonstrate that the differentiable BAY model can provide the same results with the original BAY model. Though not presented here, the total pressure recovery contour is identical to that of Fig. 32.

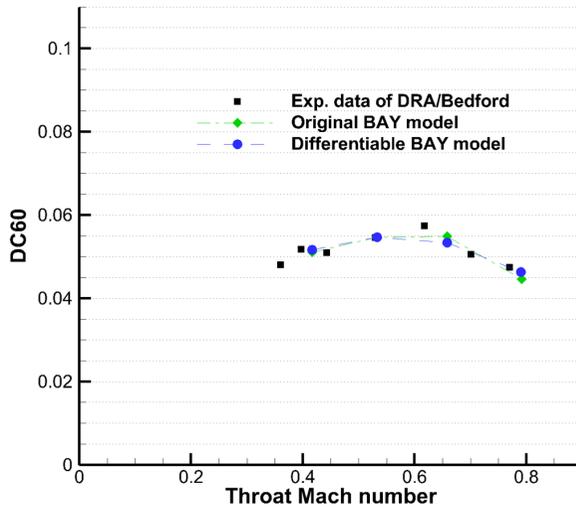


Figure 33 Validation of flow solver with BAY model and differentiable BAY model (distortion coefficient).

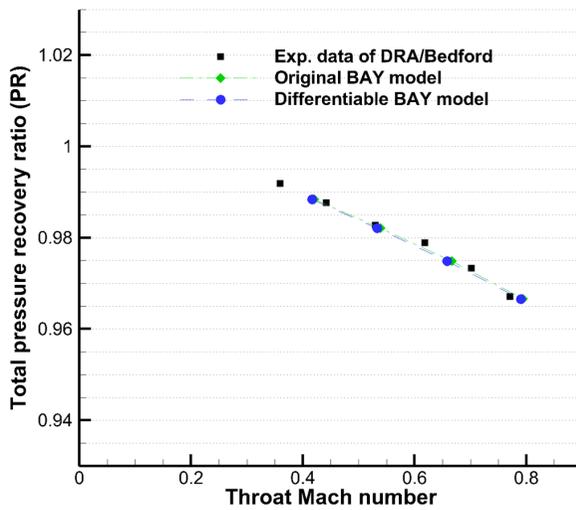


Figure 34 Validation of flow solver with BAY model and differentiable BAY model (total pressure recovery ratio).

5.3 Flow Characteristics of S-Duct

The flow characteristics produced by the S-shape are rather complicated. The flow stream moving along a curved surface yields a centrifugal force in the radial direction of curvature, which becomes substantial at the first and second bend. In order to balance the centrifugal force and to keep the flow stream moving along the curved surface, the static pressure on the port side must be larger than that it is on the starboard side. This static pressure gradient is combined with another static pressure gradient because of the pressure difference between the compression region on the port side and the expansion region on the starboard side, leading to a large net static pressure gradient [49, 79].

The net static pressure gradient produces a force from the port side to the starboard side; therefore, some portion of the flow stream does not run along the S-shape (see Fig. 35-② and Fig. 35-③). Instead, it moves downward and sometimes burrows into the original flow stream on the starboard side after the first bend. The original flow stream on the starboard side is then accelerated by the pressure gradient between the low pressure region at the first bend and the high pressure

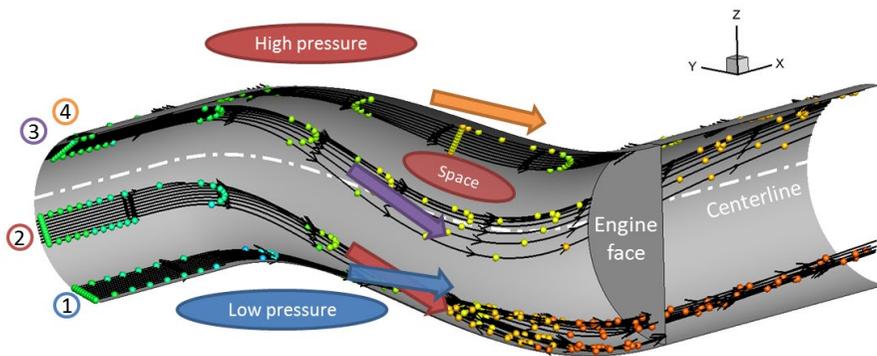


Figure 35 Flow characteristics of S-duct without vortex generator.

region at the inlet entrance. Consequently, a secondary separated flow is developed on the farther downstream side by mixing the two flow streams. This secondary flow reaches the second bend of the inlet and the engine face. The flow stream of Fig. 35-① indicating the original starboard flow stream and the flow stream of Fig. 35-② showing the downward flow stream develop the secondary flow in the S-duct. The region produced by the flow stream moving downward near the port side (Fig. 35-③) and the port side flow stream (Fig. 35-④) must be eliminated during the design process in order to diminish the second flow on the starboard side.

On the other hand, the S-duct with the VG170 configuration shows substantially different flow features. Although the secondary separated flow on the starboard side is eliminated, a small secondary flow on the port side after the engine face is observed as shown in Fig. 36. The entire flow stream (Fig. 36-① to ④) reaches the port side of the engine face, thereby creating a mixing flow. This secondary mixing flow is thought to be the main cause of distortion in the S-duct with the VG170 configuration.

The observed flow characteristics indicate that the overall flow quality can be further enhanced by reorganizing and modifying the VG configuration through some optimal design process.

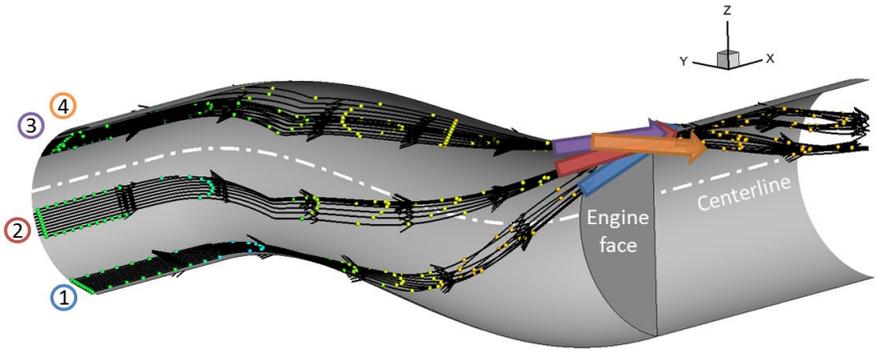


Figure 36 Flow characteristics of S-duct with VG170 configuration.

5.4 Design Approach

Conventionally, the design of a VG configuration for an S-duct was carried out without taking into account the differences in geometric parameters and/or upcoming flow conditions of each VG. As a result, configurations of all VGs were placed in a regular manner in terms of VG position, chord length, height, angle of incidence, and so forth. This result occurred mainly because the design of experiment (DOE) method was used for all of the previous design subjects [61, 63], which required huge computational cost as the number of design variables increased. The previous research with the DOE method usually considered a total of 5 to 8 design variables, which made it extremely difficult to treat each VG independently.

As mentioned above, the flow pattern on the starboard side and port side yields completely different flow characteristics. For example, the secondary flow is observed on the starboard side while a fully attached downstream flow appears on the port side. A design strategy allowing the differences in shape, angle, and position of each VG would bring more effective flow control performance. Following this philosophy, optimization was performed with five design parameters representing the positional and geometric property of each VG. The baseline VG configuration, VG170, had 11 VGs, and the present design was performed with a maximum of 55 design variables.

5.4.1 Optimization Technique, Objective Function, and Design Range

The Gradient-Based Optimization Method (GBOM) was used for the present VG design. Because the differentiable VG source term can be readily implemented, a discrete adjoint variable method was employed to obtain the sensitivity information [5-9, 11, and 80]. The Design Optimization Tool (DOT) was selected as an

optimizer, and the search direction was determined by the Broyden-Fletcher-Goldfarb-Shanno (BFGS) method. As an objective of optimization, a minimization of the DC60, the distortion coefficient for the circumferential angle of 60 degree, was selected for decreasing a non-uniformity of the flow at the engine face. The baseline total pressure recovery ratio was then imposed as a constraint to maintain the inlet efficiency. Because both the constraint and the objective function simultaneously affect the sensitivity analysis, the constraint can be added to the objective function as a penalty function. Then, the objective function is defined as:

$$F = DC60 + Wt \cdot \max(PR_{Baseline} - PR, 0) \quad (5.6)$$

where the weighting factor (Wt) is given by the ratio of the $L2$ norm for the sensitivity of the flow distortion to that of the total pressure recovery, which is given as follows:

$$Wt = \left\| \left\{ \frac{\partial(DC60)}{\partial D_i} \right\} \right\| / \left\| \left\{ \frac{\partial(PR)}{\partial D_i} \right\} \right\| \quad (5.7)$$

The design parameters include the chord length, the height, the angle of incidence, the axial location, and the circumferential location. Shape design parameters (the chord length and the height) and the angle of incidence represent the geometric property of the VG, while the axial and circumferential locations reflect the positional property of the VG. The design range is shown in Table 9. In particular, the angle of incidence starts from zero degree to include the case of the VG with no practical effect on lift generation. Figure 37 shows the design parameters and the VG installed in an S-Duct.

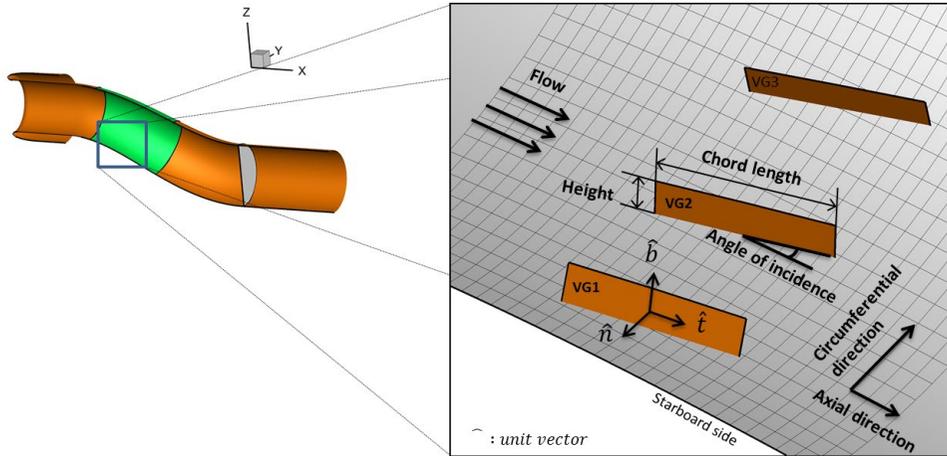


Figure 37 Geometric schematic of the vortex generator installed in S-duct and related parameters.

Table 9 Design parameters and their range.

Design parameter	Lower bound	Initial value	Upper bound
Chord length (c_{VG}/R_i)	0.140	0.280	0.420
Blade height (h_{VG}/R_i)	0.020	0.070	0.120
Angle of incidence (α_{VG} [deg.])	0.0	16.0	32.0
Axial position (X_{VG}/R_i)	-2.0	0.0	+2.0
Circumferential position (β_{VG} [deg.])	-5.0	0.0	+5.0

5.4.2 Validation of Adjoint Solver with VG Source Term Model

To verify the sensitivity of the objective function, the gradient calculated from the discrete adjoint method was compared to the sensitivity obtained by the complex step derivative method [37]. The step size of complex step derivative was taken as 10^{-20} . Sample design variables are the proposed five design parameters on the VG1, the VG that is located on the starboard side. The computed results from the two

methods are compared in Table 10. The maximum difference is about 6.0×10^{-5} (or less than 0.2%), confirming that the discrete adjoint solver is successfully validated.

Table 10 Validation results: adjoint variable method vs. complex step method.

Design parameter	Sensitivity value (dF/dD)		Difference (Abs. value)
	Complex step method	Adjoint method	
Chord length (DV1)	-0.0048945887	-0.0049003139	5.73×10^{-6}
Height (DV2)	-0.0165489810	-0.0164882855	6.07×10^{-5}
Angle of incidence (DV3)	-0.0047060463	-0.0047092213	3.18×10^{-6}
Axial position (DV4)	0.0054133545	0.0054174762	4.12×10^{-6}
Circumferential position (DV5)	-0.0028970167	-0.0028925438	4.47×10^{-6}

5.5 Design Cases

Five cases of design optimization were performed. The main objective of the first design was to demonstrate the idea of the present research using the BAY model. Only the geometric parameters (the chord length, the height, and the angle of incidence) could be chosen as a design parameters because the original BAY model cannot provide the gradient information of the positional parameters. To examine the effect of the source term in the design process, the second design was performed with the same design parameters using the differentiable BAY model. Before adding the positional design parameters (axial and circumferential locations) into the final design, a third design was conducted with the positional design parameters to check only the possibility of further improvement. After the three cases of validation process, the complete design for the optimized VG configuration was carried out by including geometric and positional design parameters. Because the present gradient-based optimization approach can be trapped into local optima, an additional design with a different starting point and off-design tests were conducted.

The performance improvement was calculated by Eq. 5.8.

$$\text{Performance improvement (\%)} = \frac{DC60_{Initial} - DC60_{Designed}}{DC60_{Initial}} \times 100 \quad (5.8)$$

5.6 Design Results

5.6.1 Case 1: Design by BAY Model with Geometric Parameters

The first design was performed with the original BAY model and three design parameters of chord length, height, and angle of incidence. Using the GBOM design process, a designed VG configuration was obtained within 80 design iterations. The DC60 decreased from 0.402269 (without the VG) and 0.044630 (with the VG170) to 0.012207 (the designed result) while maintaining the initial PR. The number of the sensitivity analysis was 15, and the optimized result was obtained through 73 design iterations (or 73 calls of the flow solver). The history of the objective function is shown in Fig. 38. Compared to the S-duct without the VG configuration, the inlet performance (Eq. 5.8) is enhanced by a total of 96.97%. Improvement from the baseline VG170 configuration (72.65%) is the contribution of the geometric design for each VG.

Figure 39 shows the change of the shape and angle of incidence of each VG. The area of the designed VG decreases (the area of the VG170 is 0.0196 with the chord

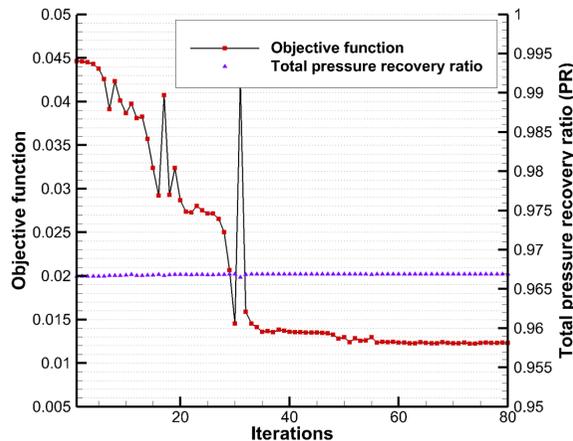


**Figure 38 History of objective function:
Design by BAY model (first design).**

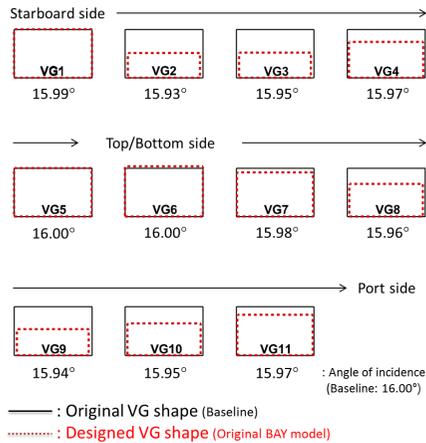


**Figure 39 Design result:
Designed VG shape and angle of incidence.**

length of 0.280 and the height of 0.07) except for the VG on the top/bottom side. Area distribution is somewhat symmetric with respect to the VG on the top/bottom side. From the top figure of Fig. 40, the S-duct with the VG170 configuration shows a higher flow distortion at the circumferential angles of 0, 90, and 180 degrees (0 deg. = starboard side, 90 deg. = top/bottom side, 180 deg. = port side), and thus the height of the designed VG configuration becomes relatively larger at these angles in order to diminish the high flow distortion.

Two additional sub-designs were conducted to examine the relationship among the three design parameters. The first sub-design was performed with chord length and height, and the second sub-design by the angle of incidence only. It can be observed from Fig. 40 that the impact of each design parameter on the inlet performance is somewhat different. In the first sub-design case, the DC60 decreases over 60% while maintaining the initial PR, and the second sub-design reduces the DC60 over 23% with the same PR. A comparison of the overall distortion patterns shows that the distortion pattern after the first sub-design is substantially different from the initial pattern with the VG170 configuration, while the second sub-design

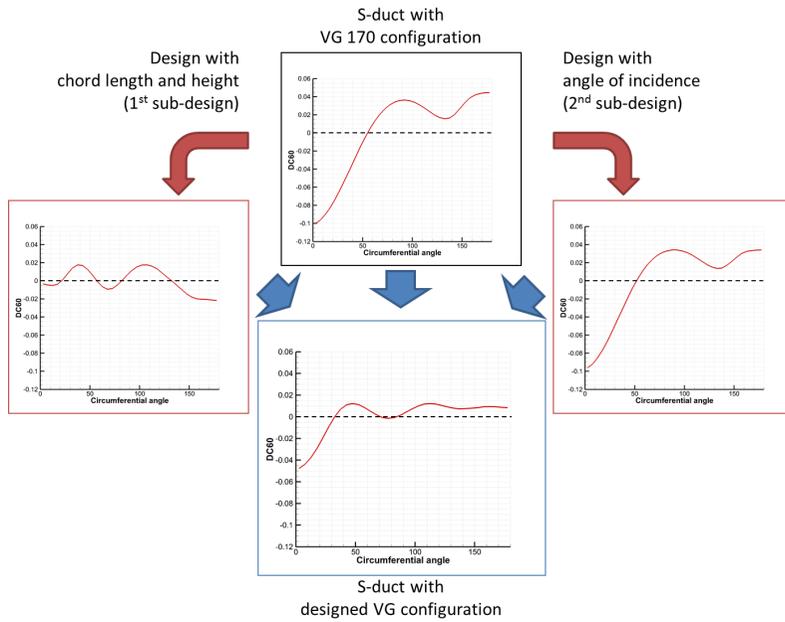


**Figure 40 Comparison of distortion patterns:
First design and two sub-designs of first design.**

reduces overall distortion without changing the initial pattern. The design result with three parameters can be obtained by combining the two design patterns, thereby indicating that three design parameters are complementary to one another. Figure 41 shows the distribution of the total pressure recovery contour after design.

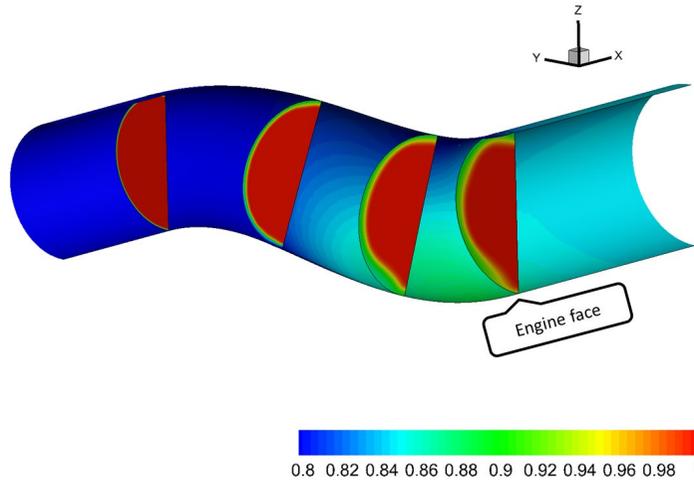
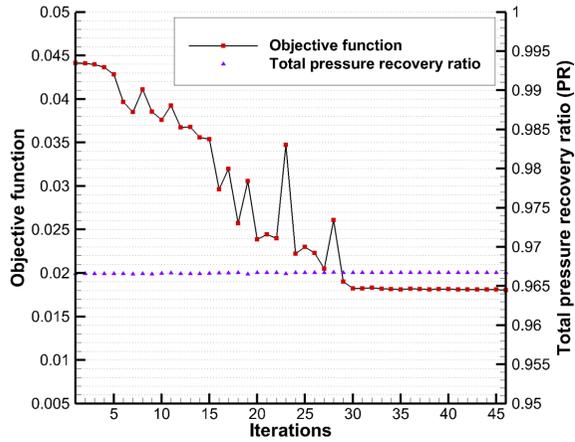


Figure 41 Total pressure recovery contour along S-duct with designed VG configuration (first design).

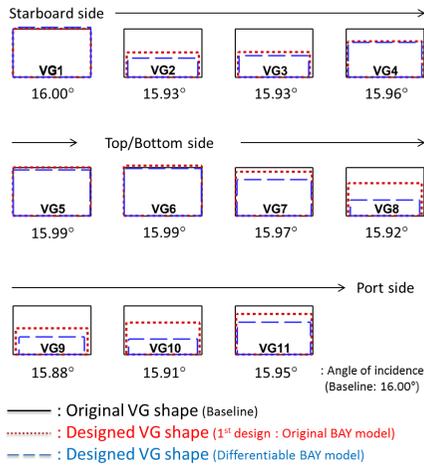
5.6.2 Case 2: Design by Differentiable BAY Model with Geometric Parameters

To identify the effect between the original BAY model and the differentiable BAY model on the design process, the second design was performed using the differentiable BAY model with the same design parameters as Case 1. After the design, the DC60 decreases from 0.044150 (with the VG170) to 0.018041 (the designed result), and the PR is almost maintained (from 0.966571 to 0.966720). The design history is shown in Fig. 42.

Although the DC60 is a bit higher than the first design result, the differentiable BAY model is valuable enough to be adopted in the design process, because the geometric pattern of the designed VG is similar to the results obtained by the original BAY model, and more importantly, the differentiable BAY model can provide the gradient information on the positional parameters. Its effect is going to be verified in Case 4.



**Figure 42 History of objective function:
Design by differentiable BAY model (second design).**



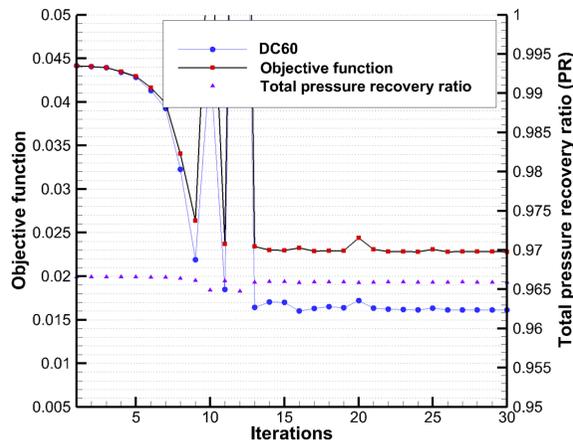
**Figure 43 Design result:
Designed VG shape and angle of incidence (second design).**

Figure 43 compares the pattern of the designed VG shape. Both designs show the same qualitative trend in a sense that the area distributions are somewhat symmetric with respect to the VG on the top/bottom side. In addition, the design effect owing to positional change, which is the design Case 3, cannot be obtained without the differentiable BAY model.

5.6.3 Case 3: Design by Differentiable BAY Model with Positional Parameters

Before obtaining the final optimized VG configuration, the third design using the differentiable BAY model with the positional parameters of axial and circumferential locations was conducted to explore the possibility of further improvement in the inlet performance.

The design results show a similar amount of distortion reduction as in the design Cases 1 and 2, but the PR is reduced by 0.07%, as shown in Fig. 44. Figure 45



**Figure 44 History of objective function:
Design with positional design parameters (third design).**

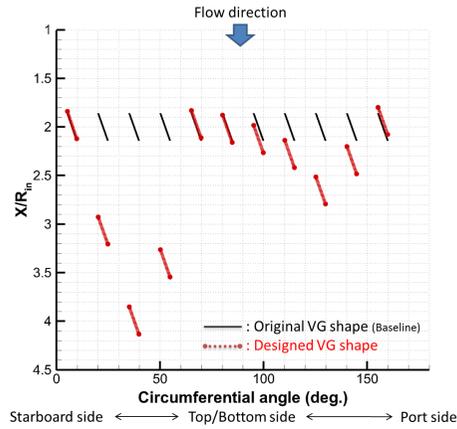


**Figure 45 Design result:
Location of each VG (third design).**

shows the positional change of each VG after the design. The DC60 decreases from 0.044150 (with the VG170) to 0.016120 (the designed result), indicating that the positional parameters play an important role in design optimization.

5.6.4 Case 4: Complete Design by Differentiable BAY Model

The complete design was performed using the validated design approach and the differentiable BAY model with all of the considered design parameters. An optimal VG configuration was then obtained by 95 design iterations. The DC60 decreases from 0.402269 (without VGs) and 0.044150 (with the VG170) to 0.009208 (the designed result) while the initial PR is maintained. The inlet performance is enhanced over 79%, which is 6.5% more improvement than the design Case 1. Figure 46 shows the design history of the complete design, and Figs. 47 and 48 illustrate the shape and location of optimized VGs. Figure 49 shows the overall changes of each VG.

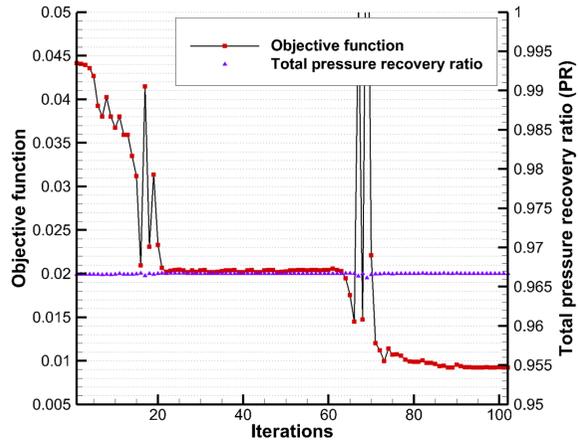


Figure 46 History of objective function: Complete design.

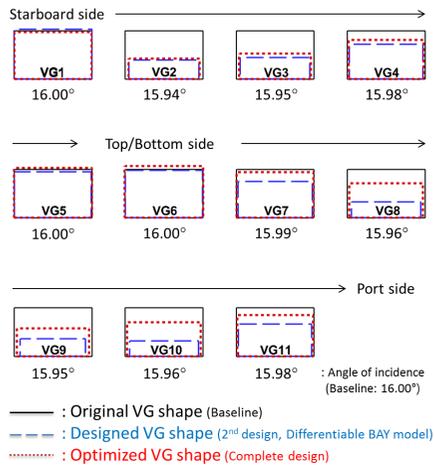


Figure 47 Design result: Optimized VG shape.

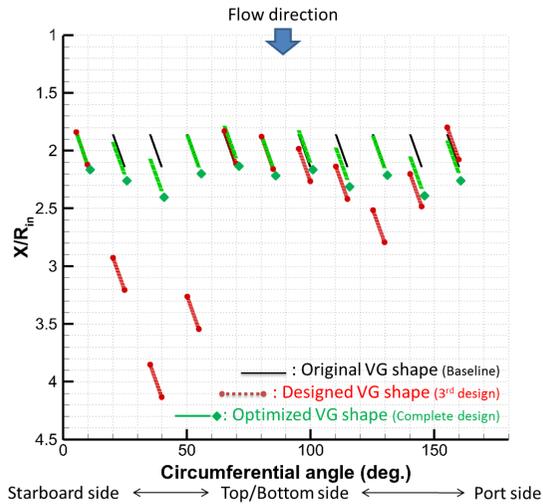


Figure 48 Design result: Location of optimized VG.

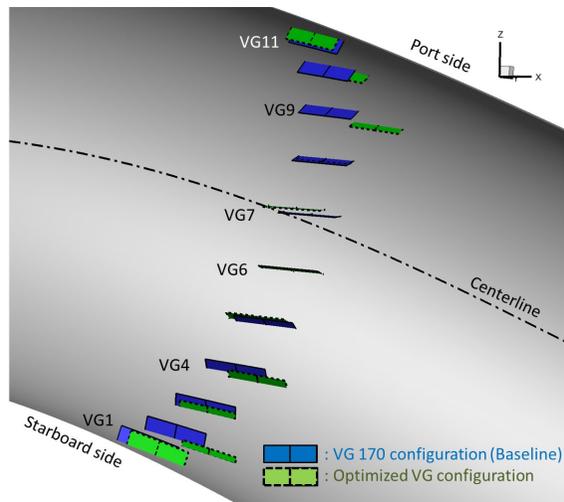


Figure 49 Design result: Optimized VG installed in S-duct (complete design).

A large portion of the flow streams in the S-duct with the VG170 configuration were moved up to the port side, as shown in Fig. 36, so the new secondary flow was

generated instead of the original secondary flow on the starboard side, which indicates that the effectiveness of the VG170 configuration was larger than the optimal condition. The effectiveness of the optimized VG, therefore, must be smaller than the VG170 configuration, and the optimal shapes of the VGs were smaller than the initial size of the VG170, as shown in Figs. 47 and 49. In addition, the effectiveness of the optimized VGs has a relation with the distortion pattern that is shown in Fig. 50. The distortion pattern of the VG170 configuration showed a large deviation in circumferential angle of 0° (starboard side), 90° (top/bottom side), and 180° (port side). To decrease the deviation at these angles, the optimized VGs on the related position to these angles showed large size, and the VGs on the other positions became smaller than the size of baseline.

The complete design result was compared with design Cases 2 and 3 in order to examine the relationship between geometric and positional parameters. It is noted from Figs. 47 and 48 that the complete design produces a better result than design Case 2 and Case 3 with smaller changes in geometric and/or positional parameters. This is mainly caused by the complementary nature between the geometric parameters and the positional parameters in the complete design. Owing to the similar complementary behavior in the design process, the role of the angle of incidence in finding an optimum cannot be neglected even if the designed angle of incidence remains very close to the baseline value. Figures 50 and 51 show the distortion pattern and the total pressure recovery contour. Similar to the one observed in the design Case 1, each design case shows a different distortion pattern but the complete design result is the favorable combination of each design case. This comparison suggests again that all of the design parameters are complementary to one another.

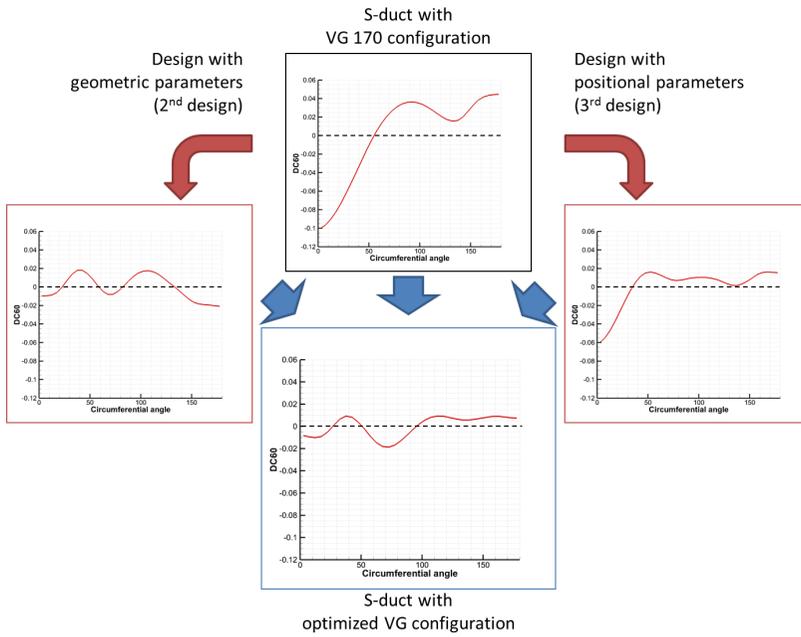


Figure 50 Comparison of distortion patterns: Second design, third design, and complete design.

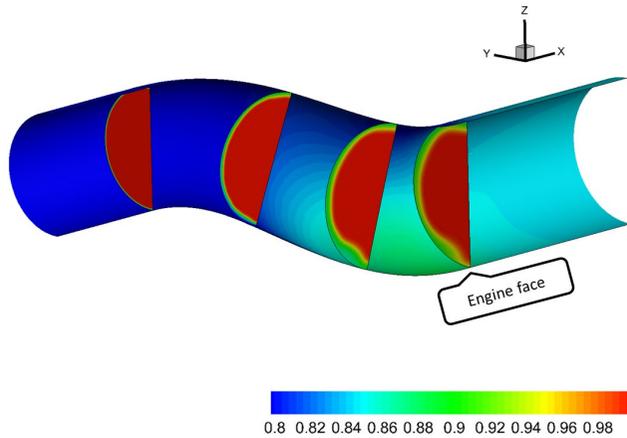


Figure 51 Total pressure recovery contour along S-duct with optimized VG configuration (complete design).

The gradient information calculated by the adjoint variable method supports the initial design patterns and the crude design results. Because the distortion coefficient of baseline (the VG170 configuration) between the top/bottom side and the port side is larger than the starboard side, the sensitivity of the objective function (or distortion coefficient) must be larger at these sections, as shown in Fig. 52. In addition, the gradients of the objective function were a positive value on the shape parameters in a large portion of the sections because the size of the VGs of the baseline were chosen as larger than the estimated optimal condition, as mentioned above. The fact that the heights were more sensitive than the chord lengths supports the optimized shape in Fig. 47 in terms of the evidently changed height while the chord length was almost maintained.

As the design process advanced, however, the optimized results are hard to be estimated perfectly because the flow pattern is modified and the sensitivity information is updated. The parameters related to the circumferential position were less sensitive than the other parameters on the all VGs but this parameter must be included for other applications and the freedom for the design. Moreover, the sensitivity of this parameter may be changed in the design process while changing the flow pattern.

Starting from the complete design result, the off-design performance of the optimized model was examined by changing the throat Mach number with the BAY model and the differentiable BAY model. The distortion coefficients for four different throat Mach numbers are presented in Fig. 53. The optimized VG configuration yields better performance with the two BAY models than the baseline VG170 configuration in all of the off-design cases, thereby demonstrating the applicability of the present design approach in wide operating conditions.

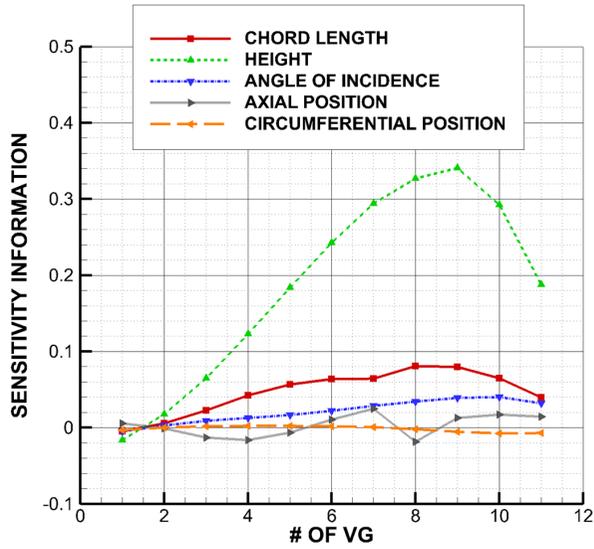


Figure 52 Sensitivity information of baseline (complete design).

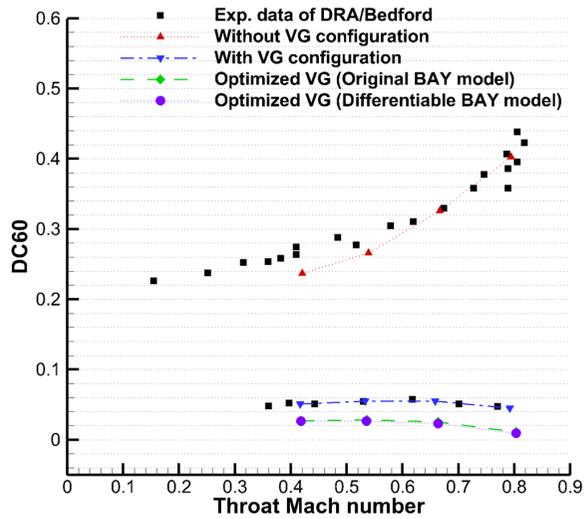
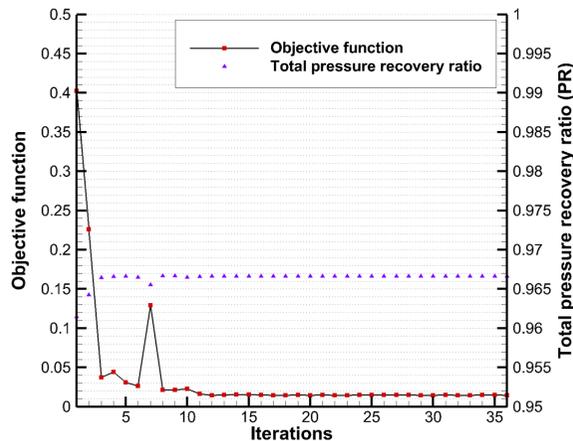


Figure 53 Off-Design condition test.

5.6.5 Case 5: Additional Design from Different Initial Condition

Because the GBOM-based designs may have a potential to be trapped in a local optimum, a design history and a final designed configuration could be susceptible to the selection of the initial design point (or the baseline configuration in this work). From this point of view, the VG170 configuration was considered as one of the proper baseline configurations. To check its validity and the viability of the present design approach, an additional design was conducted from a different initial condition, *i.e.*, the VG170 condition with the initial VG height of zero. The height of VG is known to be one of the most sensitive design parameters.

Figure 54 shows the design history, indicating that the designed configuration is obtained with 36 design iterations and 8 sensitivity analyses. It is observed that the designed VG configuration provides better performance than the VG170 configuration, but not as good as the design result obtained from the VG170 condition. This result supports that the VG170 was well selected as a baseline configuration, and the present design approach (the GBOM-based design starting from a well-chosen initial design point) provides a reliable optimal configuration



**Figure 54 History of objective function:
Design from different initial condition (additional design).**

within a specified design space. The DC60 decreases from 0.402269 (with the zero-height VG170) to 0.014449 (the designed result), and the PR increases slightly from 0.961460 to 0.966620.

5.7 Flow Characteristics of S-Duct with Optimized VG Configuration and Discussion

All of the inlets with the designed VG configuration yield considerably more improved performance than the inlets with/without the VG170 configuration, and most shortcomings of the S-Duct disappeared. In particular, the secondary flows on the starboard and port sides, which are the main cause of the flow distortion, are eliminated after design. All of the inlets with the designed VG configuration provide highly uniform flow streams like the one seen in Fig. 55.

All of the design cases provide a similar correction pattern to the swirling flow at the engine face, one of which is illustrated in Fig. 56. The vortex core at the engine face of the VG170 is positioning between the top/bottom and the port side, and the

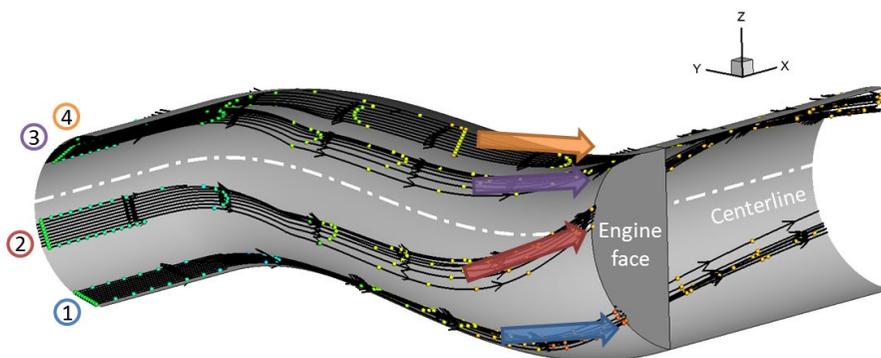


Figure 55 Flow characteristics of S-duct with designed VG configuration.

swirling flow locates on the port side. After design, the vortex core moves to the top/bottom side, and the flow mixing induced by the optimized VGs makes the total pressure distribution over the whole engine face uniform.

The distortion coefficient, consequently, was significantly reduced while the total pressure recovery ratio was maintained. In the three cases validation of the proposed design framework, the design parameters of position and shape were separately examined by the original BAY model or the differentiable BAY model, and the resulting distortion coefficient decreased over 70% from the VG170. In the complete design, a further improved result was obtained by including all of the design parameters (a total of 55 design variables). As a result, the S-duct with the optimized VG configuration provided 79% improvement in the distortion coefficient over the baseline model. The results confirm that the proposed design approach based on the independent treatment of the design parameters for each VG leads to more efficient configurations.

Although the present adjoint design approach may not guarantee the global optimum, several off-design tests maintain improved performance over a wide range of operation conditions, thereby supporting the claim that the proposed design

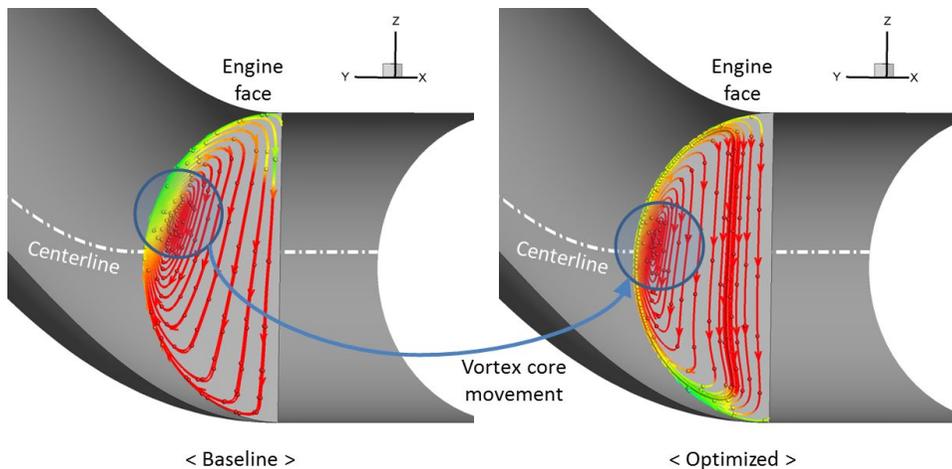


Figure 56 Design result: Comparison of mixing flow patterns at engine face.

approach is applicable to more complex configurations of these kinds under a wide range of operating conditions.

Table 11 summarizes the improvements of the DC60 after five design cases.

Table 11 Design results: Distortion coefficient and total pressure recovery ratio.

Design cases	Changes of DC60	Percentages of DC 60 reduction (vs. baseline)	Changes of PR	Percentages of Pr increase (vs. baseline)
Case 1	0.0446→0.0122	72.65%	0.9666→0.9669	0.03%
Case 2	0.0442→0.0180	59.14%	0.9666→0.9667	0.02%
Case 3	0.0442→0.0161	63.49%	0.9666→0.9659	-0.07%
Case 4	0.0442→0.0092	79.14%	0.9666→0.9667	0.015
Case 5	0.4023→0.0144	96.42%*	0.9615→0.9666	0.54%*

* This value is compared to the S-duct without VG.

Chapter VI

DLR-F6 Aircraft

Secondly, the wing-body configuration of aircraft (DLR-F6) is considered an external flow application.

6.1 DLR-F6 Wing-Body Configuration

6.1.1 Geometric Information

The DLR-F6, a typical modern wide-body transport, was designed by German Aerospace Center (DLR) and is derived from the DLR-F4 wing-body configuration. The DLR-F6 has two configurations: the wing-body and the wing-body-nacelle-pylon. The latter configuration has a wing-mounted twin-engine [81], but the former one has only wing and body components. The experimental data measured by the ONERA-S2MA wind tunnel is provided with the specific information of geometry manufactured by DLR [82, 83]. The aerodynamic mean chord is 141.2mm , the reference area is $145,400\text{mm}^2$, and the aspect ratio is 9.5. The reference center of moment calculation is $(x=157.9, y=0.0, z=-33.92)$ mm based on the CAD coordinates. The nose location in CAD geometry is $(x=-347.0, y=0.0, z=17.5)$ mm . The shape of the DLR-F6 for the wind-tunnel experiment is shown in Fig. 57.

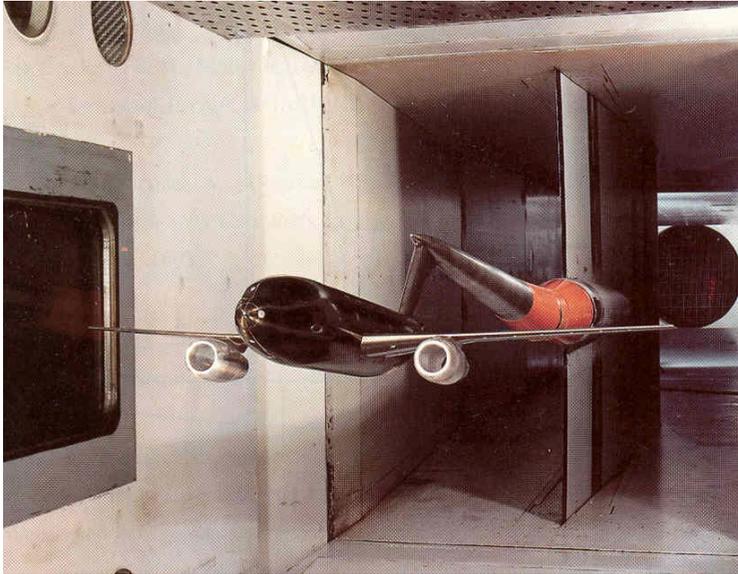


Figure 57 Geometric schematic of DLR-F6 model [83].

6.1.2 Performance Coefficient for Aircraft

Generally, the aircraft performance is represented as lift (C_L), drag (C_D), and moment (C_M) coefficients. The lift and drag coefficients are closely related to aircraft flight range, aerodynamic efficiency, and so forth. The other coefficients with respect to the pitching, yawing, and rolling moment play an important role in determining the stability of an aircraft [84]. To consider the lift and drag simultaneously, the ratio of lift to drag (L/D , the same as the C_L/C_D) is presented for a direct measurement of the aerodynamic efficiency of a given airplane. The L/D is also connected to the maximum endurance (E) and the maximum range (R) for a jet airplane, both of which are calculated as follows:

$$E = \frac{1}{c_t} \frac{C_L}{C_D} \ln \frac{W_0}{W_1} \quad (6.1)$$

$$R = 2 \sqrt{\frac{2}{\rho_{\infty} S}} \frac{1}{c_t} \frac{C_L^{1/2}}{C_D} (W_0^{1/2} - W_1^{1/2}) \quad (6.2)$$

where c_t is the thrust-specific fuel consumption, W_0 is the weight with full fuel tank, and W_1 is the weight with empty fuel tank. The ρ_{∞} is density and S is the wing area. When the ratio of W_0/W_1 is the highest, the aircraft can contain maximum fuel weight W_F . To estimate brief weights of aircraft, Raymer introduced various calculating methods for weight in his publication [1]. For maximum endurance, an aircraft must fly with maximum L/D .

6.1.3 Previous Vortex Generator Study for Aircraft

The Vortex Generator (VG) has been popularly used on most of commercial aircrafts, and there are many patents related to the VG. For examples, several small VGs have been popularly installed at the leading edge of the wing upper surface to prevent separation and stall. Moreover, a rather large size VG is installed to guide the flow on the nacelle [85]. These two types of VG are installed on the Boeing 737, 767, 777, and so forth as a part of the performance improvement package.

The device installed on the aircraft, however, was not a main research topic. The only study to discover the effectiveness of VG on the stall characteristics of an airfoil or a wing in high angle-of-attack and/or low speed was performed in China and then the results were published as a journal in Japan [86]. Many individual elementary experiments using the actual VG on the actual aircraft can be found by web-searching, but these results have not published as research paper. These situations indicate that the VG on the aircraft is quite useful and popularly adopted nowadays, but either the VG is hard to be considered as a research topic or the industries have enough data about the VG to use it. Few precedent research about the VG related to the aircraft have been only focused on the separation delay by supplying additional energy to the flow by installing the VG on the wing upper

surface.

Because a VG generates longitudinal vortices to give rise to local mixing of mean flow, to energize the low-energy boundary layer, and to delay or prevent the turbulent boundary layer separation, the point of view in previous research is absolutely correct. However, there is another well-known functions that the thin-plate type VG may modifies the direction of the flow to be parallel to the VG, like a guiding vane [18, 21, 58, and 60]. By adopting these advantages, the usage of the VG can expand to the other point of view. Controlling junction vortex of the aircraft is an example. By concurrently considering these two merits of VG, the detrimental problems induced by low-energy and wrong flow directions can be controlled.

6.2 Flow Analysis of DLR-F6

The flow conditions of this study followed the DPW-III [19, 20] whereby all of participants were required to provide data of “fixed- C_L , single point” and “drag polar.” The freestream Mach number is 0.75, the Reynolds number based on the mean chord length is 5 million, and the fixed- C_L is 0.5. Among the presented angle of attack for drag polar of $\alpha = [-3, -2, -1, -0.5, 0, 0.5, 1, 1.5]$, the all of the flow analysis and design optimizations are performed at a zero angle of attack.

A Reynolds-Averaged Navier-Stokes (RANS) solver was employed for three-dimensional flow analysis and design. The Roe scheme [23] was adopted to evaluate the convection term and Yoon’s LU-SGS scheme [35] was used for time integration. The 3rd order accurate TVD-MUSCL with Van-Albada limiter was applied. For simulating turbulent flow, Menter’s $k-\omega$ SST-2003 model [31] was incorporated.

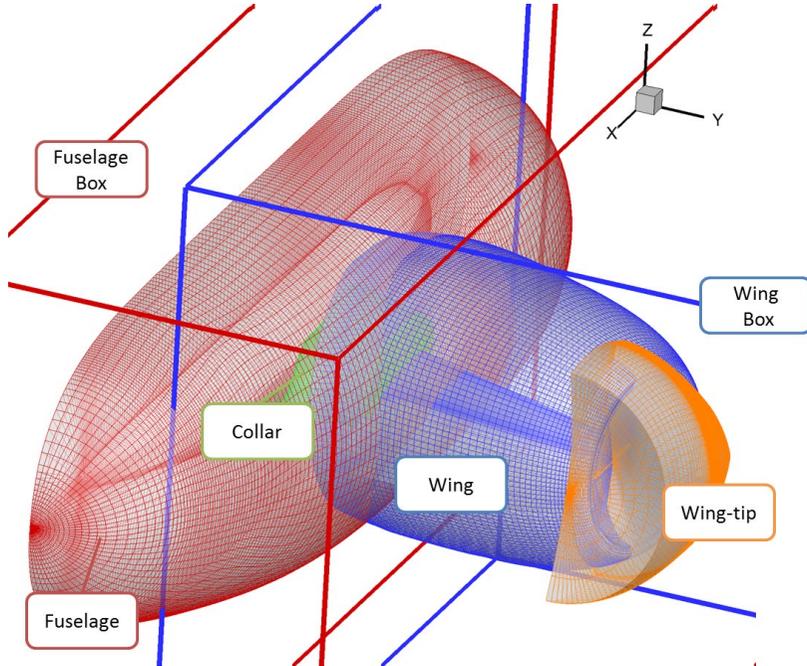


Figure 58 Grid topology of DLR-F6.

6.2.1 Grid Topology and Overset Structure

The grid was generated based on the mesh system presented by Sclafani *et al.* [19, 74, and 87]. Figure 58 shows the grid topology for the given problem and the mesh points on the surface are plotted in Fig. 59. Among the four levels of given grid systems (coarse, medium, fine, and extra fine), the coarse grid was chosen as a basis of the grid generation for the efficiency of the flow analysis and the design. As an exception, the collar block was generated based on the medium grid level because additional cells are necessary to resolve the detail flow around the wing-body junction and to describe the effects of a flow control device. The final generated grid is composed of 6 parts: fuselage, collar, wing, wing-tip, fuselage box, wing box, and global box. The total number of cells is 1.7 million.

To analyze the flow fields accurately by using the overset grid technique,

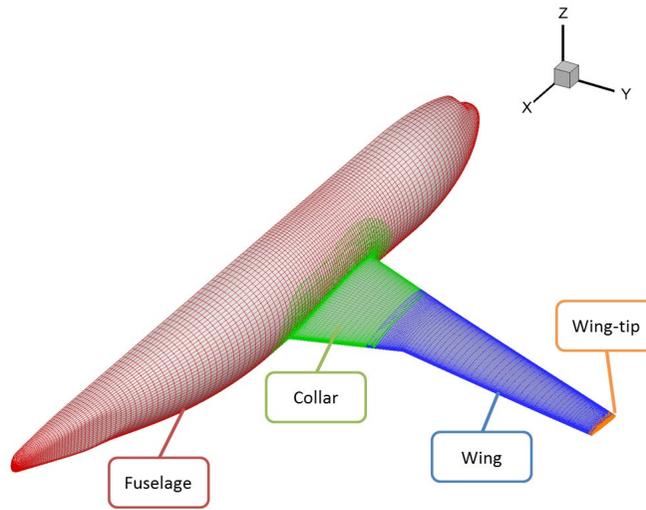


Figure 59 Surface grid distribution.

advanced methodologies such as the overlap optimization, the sub-cell TFI, and the SBIG scheme were applied.

6.2.2 Flow Analysis of DLR-F6 without VG

The computed results were compared to the wind-tunnel experimental data presented in DPW-II [82, 83] and to the CFD data of the DPW-III participants [66]. Because the experimental data based on the flow condition of the DPW-III does not exist, computed results must be compared to the DPW-II experimental data in spite of the different Reynolds number.

Figure 60 shows a lift curve versus the angle of attack. The solid red line is the calculated data, and the broken green and blue lines show the range of other participants's results. At all angles, the red line lies between upper and lower limits of the DPW-III results. Figure 61 shows a comparison of drag coefficient with a fixed- $C_L=0.5$ condition to the other researchers results. The blue circles are the computed data of the other participants, and the red diamond is the calculated data

with presented flow solver. Figures 60 and 61 prove that the calculated lift and drag are acceptable and that the presented solver is useful enough to predict the flow physics of external application. Figure 62 illustrates a pressure contour of DLR-F6 wing-body configuration, and Fig. 63 shows the junction vortex on the wing trailing edge near the wing-body junction. Both results of Figs. 62 and 63 are calculated at a zero angle of attack. The eye of the calculated junction vortex is at $x=233.884\text{mm}$, $y=89.3561\text{mm}$, which is within an acceptable error range from the DPW-II results.

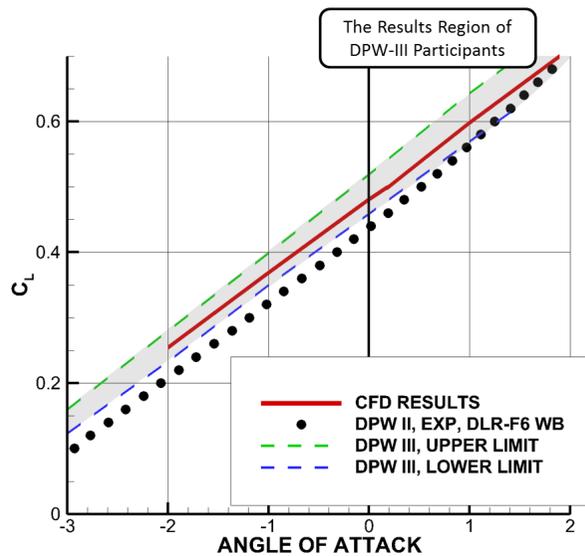


Figure 60 Lift coefficient curve.

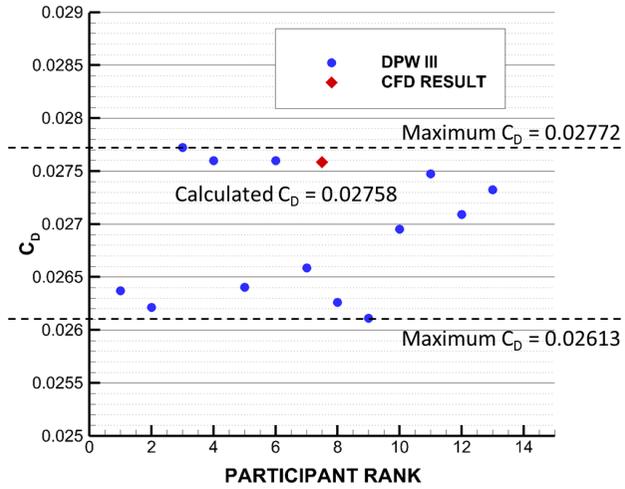


Figure 61 Comparison of drag coefficient ($C_L=0.5$).

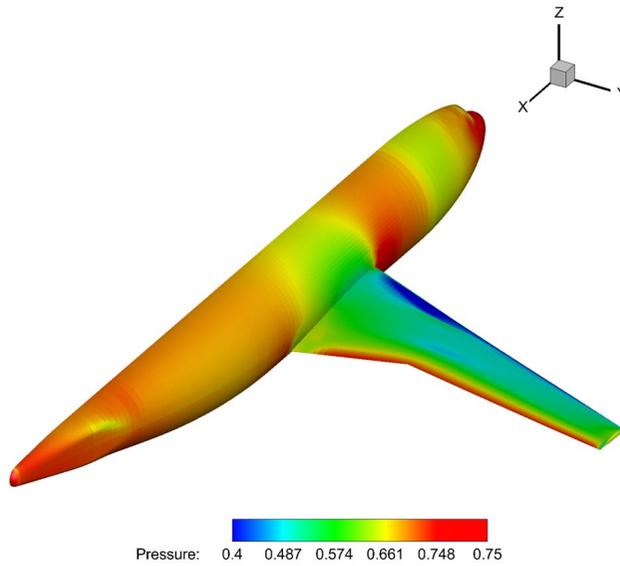


Figure 62 Pressure contour of DLR-F6.

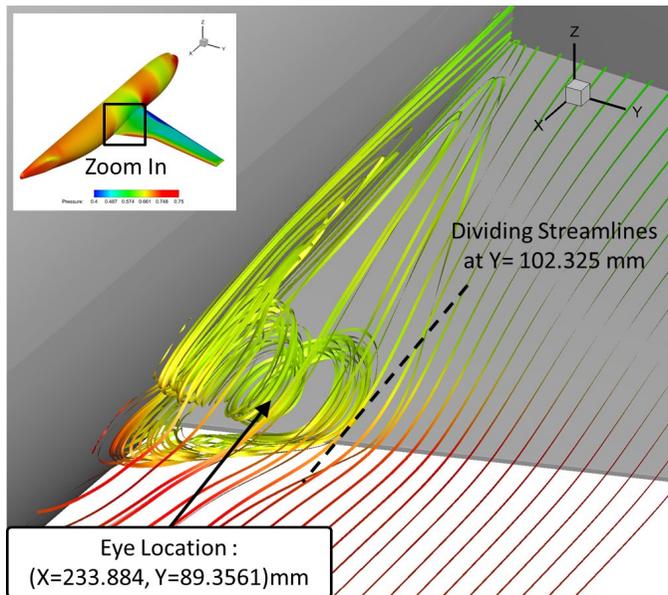


Figure 63 Shape and size of junction vortex.

6.3 Flow Characteristics of DLR-F6 and Junction Vortex

The flow characteristics produced by the DLR-F6 is quite complicated, and too many complex phenomena, such as shock, wing-tip vortex, wing-body junction vortex, wing trailing-edge vortex, and so forth, are developed at one time. Although all of these phenomena should be considered at the same time, this paper focused only on the development of the wing-body junction vortex.

A large number of studies have been conducted to reveal the physics behind the wing-body junction by using simplified geometries [88-91]. A representative configuration of simplified junction involves an obstacle profile (mimics a wing) mounted normally on a flat plate. Of the several flow characteristics of the junction, many studies focused on the horseshoe vortex, thereby phenomena of the junction vortex (or the corner separation on the trailing-edge of the wing) relatively neglected. The incoming flat plate boundary layer rolls up around the leading edge of the obstacle when the flow approaches to the junction, causing the generation of a horseshoe vortex. The horseshoe vortex, therefore, can be classified as Prandtl's first kind of secondary flow because it is induced by the skewing of flows [92]. This horseshoe vortex is stretched and convected around the wing. The shape and strength of the horseshoe vortex is related to the bluntness of the obstacle's leading edge and the momentum of incoming boundary layer. Fleming *et al.* [88] introduced the bluntness factor (BF) which is an indicator of the strength of the horseshoe vortex, and the momentum deficit factor (MDF_x) that linked to a parameter of the distortion of the axial velocity. Mehta [89] confirmed that a round leading edge (high BF) creates a strong horseshow vortex with a large spatial extension, and that a sharp leading edge (low BF) creates a thinner horseshoe vortex. A larger MDF_x brings the legs of the horseshoe vortex closer to the wing. Because the BF of the DLR-F6 is 0.075, the DLR-F6 is classified as low BF junction. According to the previous literatures, it seems that low BF junctions are more likely to suffer from

corner separations [90, 91].

Only a few publications [90, 93-96] focused on the analysis of the corner separation on the wing trailing-edge, which is referred to as a junction vortex in this paper. Previous researchers concluded that the interaction between two perpendicular boundary layers is one of reasons for the corner separation and that the growth of pairs of vortices within the corner is corresponded to Prandtl's second kind of secondary flows because this secondary flow is triggered by Reynolds stresses [92]. Barber [96] wrote that there is an interaction between the horseshow vortex and the corner separation. When the incoming flows have a thick boundary layer, a large horseshoe vortex is formed with a small corner separation zone. Contrary to this phenomenon, a small horseshoe vortex and a large corner separation zone are generated by a thin boundary layer flow. Barber, however, did not provide any information about the strength of the corner separations and their influence on the flow physics near the junction.

From the results of the flow analysis and of the previous publications, this study predicted that the junction vortex has an effect on the distribution of physical properties such as pressure, density, velocity, and so forth. Figures 64 and 65 illustrate the pressure at near and far locations from the junction vortex. It was found that pressure contour around a junction vortex in Fig. 64 is lower than that of the area without the vortex in Fig. 65. This high-pressure region of the trailing edge on upper surface directly influences the high-pressure under the wing. From this observation, the junction vortex is interrupting a recovery of pressure, density, and the Mach number at the trailing edge of wing upper surface, which causes the lift decrease. In fact, the previous study for eliminating the junction vortex by the fairing also discovered the reduced lift at the same angle of attack [20, 66].

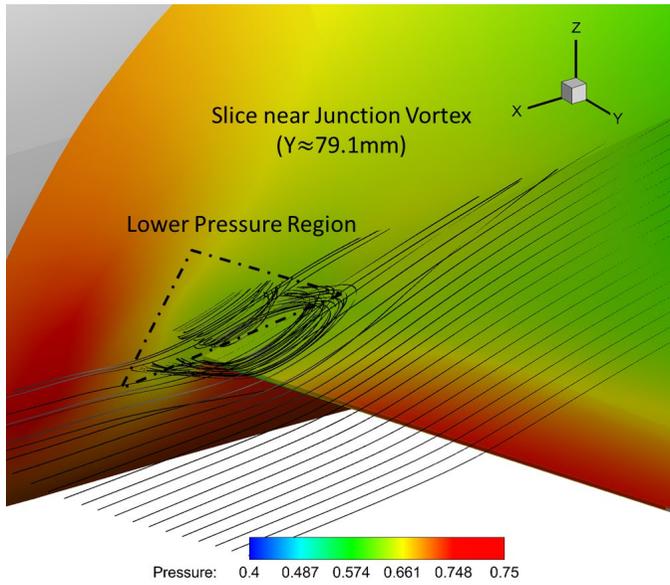


Figure 64 Pressure contour near the junction vortex.

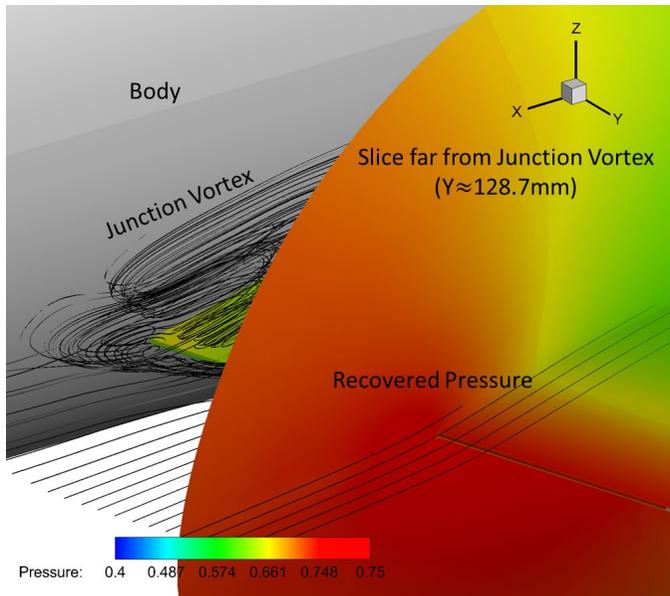


Figure 65 Pressure contour far from the junction vortex.

6.4 Parametric Study

Prior to the design process, several cases of parametric study were performed to decide the baseline configuration of Vortex Generator (VG) for design optimization. These cases were decided based on the flow characteristics of junction vortex.

For measuring the DLR-F6 performance, the lift and drag coefficients (C_L , C_D) and the ratio of lift to drag (L/D) were observed. Two comparison graphs were presented for each case, and the results were compared to the case without the VGs. Without the VG, which is referred as an initial case, the C_L , C_D , and L/D are 0.4823, 0.0271, and 17.7999, respectively.

In all of the parametric studies, the chord length (c_{VG}) and height (h_{VG}) of VG non-dimensionalized by the aerodynamic mean chord (c_{mean}) of DLR-F6 were fixed to 0.1 (14.12mm) and 0.01 (1.412mm), respectively. These parameters of the VG are designed in the optimization stage, and the normal vector of VG (\hat{n}) is normal to the installed surface. By reflecting the junction vortex size and the gaps of the VGs, three VGs were installed as an initial VG on each side.

As a first case (Case 1), three VGs were installed side-by-side along the wing in a spanwise (y -) direction on the middle of the wing upper surface near the body where the junction vortex begins. The positional effects of the VGs were checked by moving the VGs toward the trailing edge along the streamwise (x -) direction. Next, three VGs were located on the body surface above the wing to control body boundary layer separation (Case 2). From the results of these two positional parametric studies, the incidence angle of the VGs was changed to consider effects of the amount of supplied energy and the flow guiding direction (Cases 3 and 4). As a fifth case, the angle of incidences of the VGs placed on the body in front of the wing root was considered to verify the effect of the horseshoe vortex on the junction vortex (Case 5). To check the effectiveness of the VGs installed on the lower surface, three VGs were installed and moved from the leading edge to the trailing

edge as a sixth case (Case 6).

Cases of 1-6 were constructed for checking the role of the VG depending on the location and the angle of incidence, which does not consider the simultaneous effects of the first and second types of secondary flows. Cases of 7 and 8, however, considered the coupling effects of the VGs by concurrently installing them on the wing upper surface and the body surface. In Case 7, the VGs located on the body surface were fixed and the VGs installed on the wing upper surface were moved along the streamwise (x -) direction, which is reflected in the results of the Cases 1, 2, 3, and 4. Case 8 also considers the results of the above cases, but this case has the inverse condition of Case 7. While the VGs of the wing upper surface moved, the VGs on the body were locked up. In Case 9, the number of VGs on the wing upper surface was changed from 2 to 15. The added VGs were installed side-by-side along the wing spanwise (y -) direction.

The percentage of the performance improvement amounts was calculated as follows:

$$\text{Performance improvement (\%)} = \frac{L/D_{Initial} - L/D_{Improved}}{L/D_{Initial}} \times 100 \quad (6.3)$$

Figure 66 illustrates the three parameters used in the parametric studies and their ranges, and each parameters of each test case is summarized again as a Table in each sub-chapter.

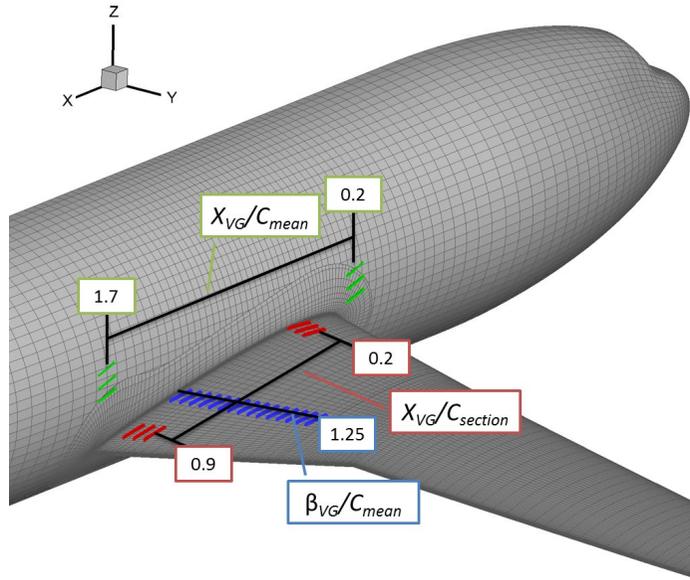


Figure 66 Parameters and its ranges.

6.4.1 Case 1: Position, Wing Upper Surface

As a first parametric study, the flow characteristics related to the wing boundary layer and the VGs on the wing upper surface were observed. Figures 67 and 68 show the results of Case 1.

Table 12 VG condition: Case 1.

# of VG	Chord length (c_{VG}/c_{mean})	Height (h_{VG}/c_{mean})	Angle of incidence ($^{\circ}$)	Streamwise position ($X_{VG}/c_{section}$)	Wing spanwise position (β_{VG}/c_{mean})
1	0.1	0.01	-15.0	Parameter	0.55
2	0.1	0.01	-15.0	Parameter	0.60
3	0.1	0.01	-15.0	Parameter	0.65

In the comparison graph, the broken red line is an initial C_L , and the broken green line is an initial C_D , and the broken blue line is an initial L/D , which is the same in all comparison graphs of Cases 1-9. The solid lines show the computed results, and the color is respectively the same as the initial graph. After the VG installation, lift and drag increase in the middle range of airfoil. Because the increase rate of lift is larger than that of the drag, the ratio of lift to drag also increases. The increased lift reaches its peak at $X_{VG}/C_{section}=0.7$, but the performance decrease sharply after then. The maximum improvement of L/D is 3.37% (from

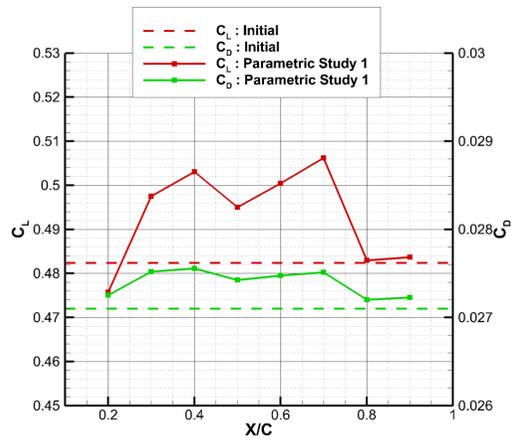


Figure 67 Parametric study Case 1: Comparison of C_L and C_D .

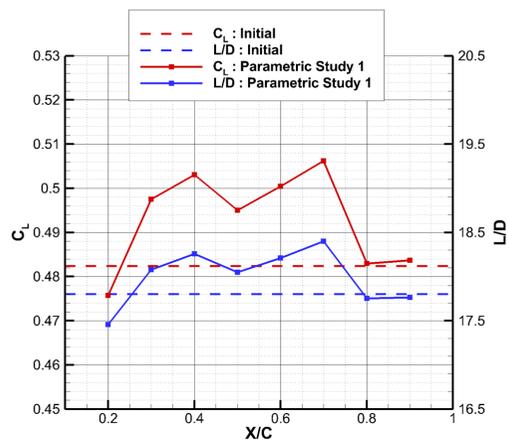
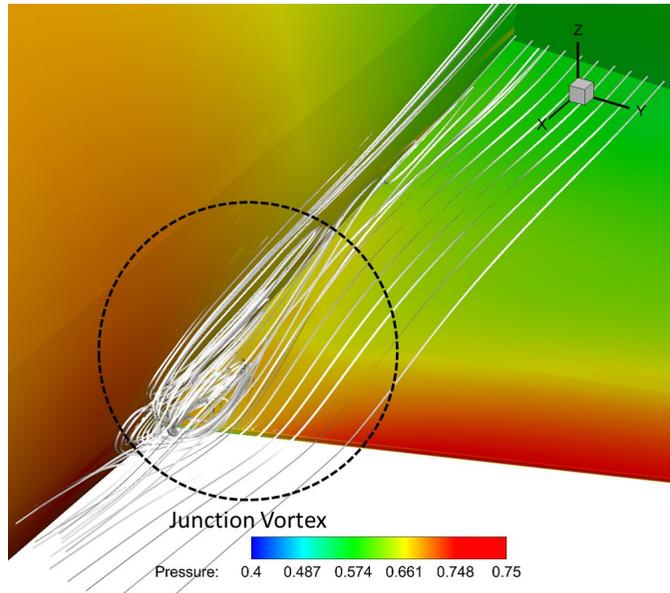


Figure 68 Parametric study Case 1: Comparison of C_L and L/D .



**Figure 69 Parametric study Case 1:
Junction vortex and high-pressure region on the trailing edge.**

17.7999 to 18.3998). Although this amount of improvement is quite substantial, a small vortex still remains in the junction, and the vortex has a form as irregular as ever. The shrunken vortex and the extension of the high-pressure region of the trailing edge are shown in Fig. 69.

6.4.2 Case 2: Position, Body Surface

As a second parametric study, the flow characteristics related to the horseshoe vortex were observed by installing and moving three VGs on the body surface. These VGs posed above the wing and moved across the streamwise (x -) direction. To disturb the growth of the horseshoe vortex, the VGs had a positive angle that induced the tail of horseshoe vortex to move downward.

Table 13 VG condition: Case 2.

# of VG	Chord length (c_{VG}/c_{mean})	Height (h_{VG}/c_{mean})	Angle of incidence ($^{\circ}$)	Streamwise position (X_{VG}/c_{mean})	Body position (β_{VG}/c_{mean})
1	0.1	0.01	15.0	Parameter	0.15
2	0.1	0.01	15.0	Parameter	0.20
3	0.1	0.01	15.0	Parameter	0.25

Two comparison graphs are presented in Figs. 70 and 71. In these graphs, Case 2 shows better results than Case 1, which shows that the control of the horseshoe vortex has more possibilities to eliminate complex flow physics than that of the stress-induced secondary flow, but this effect depend on the VG location. The L/D increased in the range between 0.3 and 0.7 of the streamwise position, and the peak appeared at $X_{VG}/c_{mean}=0.7$. After the peak, the coefficients decrease sharply as in Case 1. The maximally increased L/D is 4.34% (from 17.7999 to 18.5717), which is the best value among the all parametric studies.

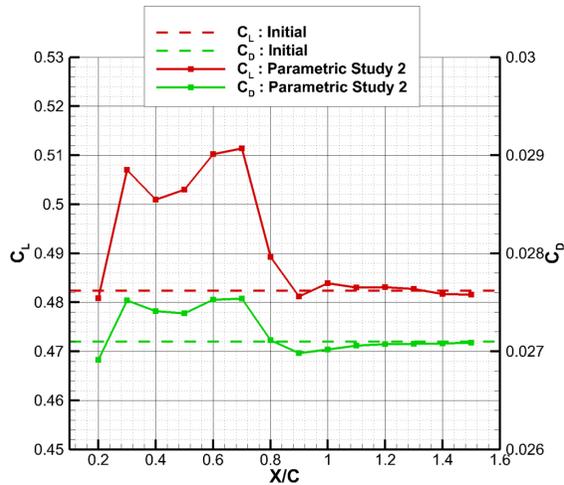


Figure 70 Parametric study Case 2: Comparison of C_L and C_D .

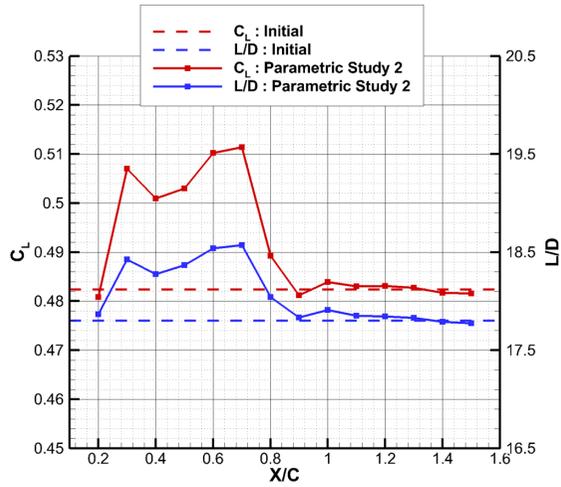
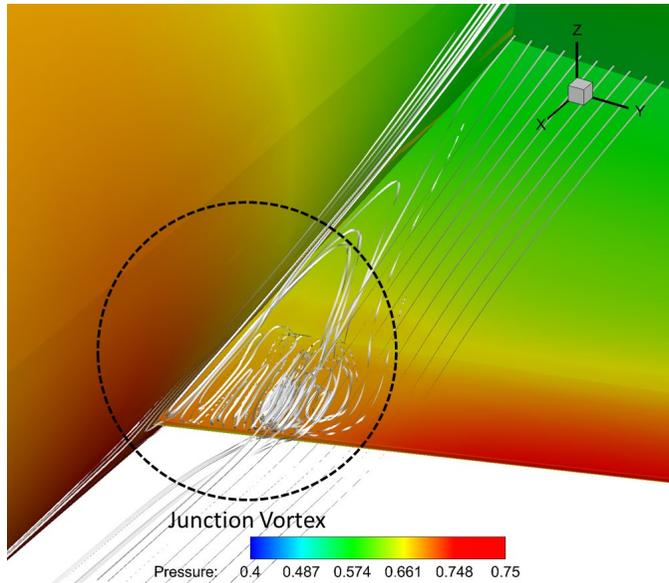


Figure 71 Parametric study Case 2: Comparison of C_L and L/D .

There is a considerable feature on the junction vortex shape. The shape of vortex in Case 1 is narrow and tall, the vortex shape of Case 2 is wide and short, and both of them are smaller than the initial shapes. Specifically, the junction vortex of this case has a systematic form as shown in Fig. 72. From this comparison, we can reach a conclusion that the VGs on the wing surface and the body surface have different ripple effects on the shape of junction vortex, even if the amounts of L/D increase are not significantly different.

Moreover, the extension of high-pressure region is also different from that of Case 1. The pressure value under the disorderly vortex that appeared in Case 1 is lower than the region under the orderly vortex that appeared in Case 2, meaning that the systematic wide junction vortex is seemingly weaker than unsystematic narrow vortex.



**Figure 72 Parametric study Case 2:
Junction vortex and high-pressure region on the trailing edge.**

6.4.3 Case 3: Angle of Incidence, Wing Upper Surface

From the results of Case 1, the streamwise (x -) position is decided as 70% of the chord length of the sectional airfoil. To examine the effectiveness of the flow direction turned by the VG, the angle of incidence was changed from -45° to 45° because of the limitation of the VG source term model. Although the BAY model shows seemingly positive results, even in the large incidence angle, the BAY type model has possibilities to impede the accuracy of modeling because this model was originally designed with small angle approximation.

Table 14 VG condition: Case 3.

# of VG	Chord length (c_{VG}/c_{mean})	Height (h_{VG}/c_{mean})	Angle of incidence ($^{\circ}$)	Streamwise position ($X_{VG}/c_{section}$)	Wing spanwise position (β_{VG}/c_{mean})
1	0.1	0.01	Parameter	0.7	0.55
2	0.1	0.01	Parameter	0.7	0.60
3	0.1	0.01	Parameter	0.7	0.65

Figures 73 and 74 show the comparison of C_L , C_D , and L/D , and these graphs have approximately symmetric shapes. From -5° to 5° , the C_L and C_D are almost same as the initial value, but the coefficients jump up in the external angles of this range. The difference between the positive angle and the negative angle begins to appear at an absolute angle of 10° . These coefficients still have their initial value in positive angle, but that value increases sharply at the negative angle. That difference is caused by a flow direction faced by the VGs. Because the initial flow direction to initiate the VG is defined along the x -direction, the real flow direction could not be a zero angle. At $X_{VG}/c_{section}=0.7$, the actual flow direction is nearly $2\sim 3^{\circ}$, thus the actual attack angle between the VG and the real flow is only $7\sim 8^{\circ}$. The graphs,

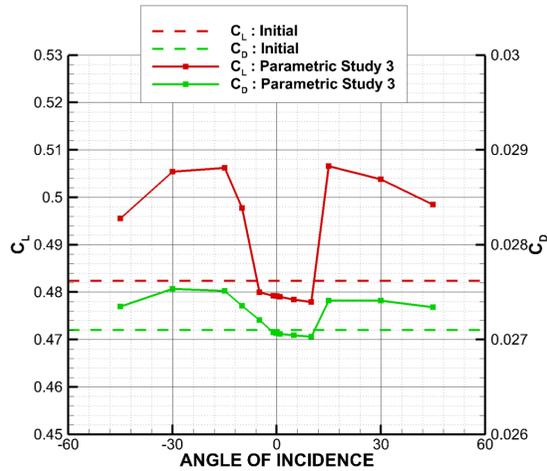


Figure 73 Parametric study Case 3: Comparison of C_L and C_D .

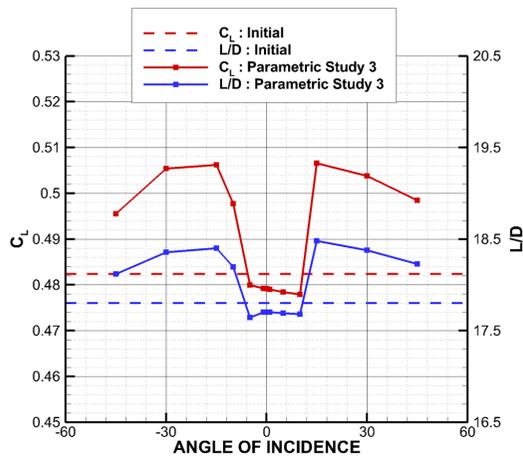
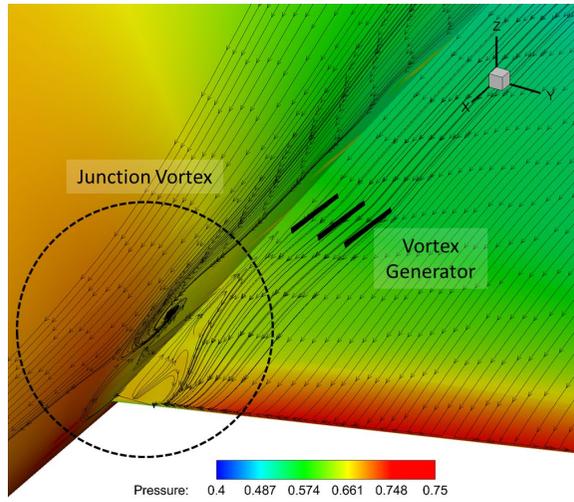


Figure 74 Parametric study Case 3: Comparison of C_L and L/D .

therefore, are practically symmetric although the graphs are one-sided to the positive angle.

When the VG has an incidence angle of -10° , the flows approach the body. The junction vortex, thus, becomes smaller, narrower, and weaker, and the high-pressure region on the trailing edge is expanded, which is the same characteristic of Case 1 that also has a minus angle to the VG. On the contrary, the flows veer away from the body when the VG has a positive angle, and the vortex has enough space to develop. These phenomena are illustrated in Figs. 75 and 76, and the junction vortices are presented as a surface line to mark out its size and shape easily on the wing surface. The good point of the positive angle of the VG is that the strength of the junction vortex is weakened because the vortex can expand enough without being squashed, which is proven by the expansion of the high-pressure region under the junction vortex in Fig. 76. From this phenomenon, the L/D at 15° has a peak value of this case, but at minus 15° , which shows an almost identical amount of improvement, is selected as a best solution. The L/D at -15° improves 3.37% (from 17.7999 to 18.3989), which is exactly the same with Case 1 because this case has the same condition.



**Figure 75 Parametric study Case 3:
Shape of junction vortex with negative angle VGs.**

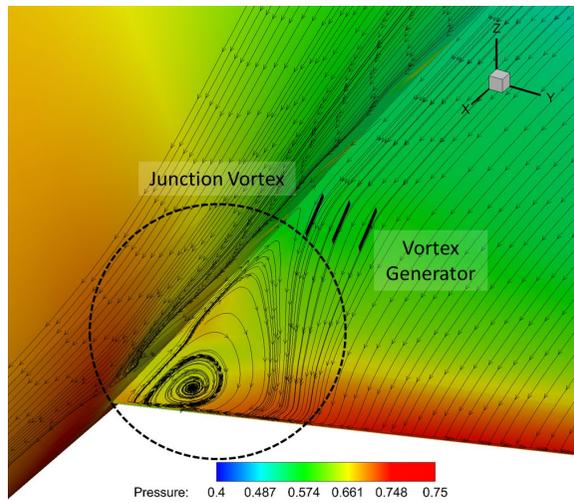


**Figure 76 Parametric study Case 3:
Shape of junction vortex with positive angle VGs.**

The overall shape of junction vortex is similar with Fig. 69 in Case 1.

6.4.4 Case 4: Angle of Incidence, Body Surface

This case is similar to Case 3. From the results of Case 2, the streamwise (x -) directional parameter on the body surface was decided as 0.7 of the mean chord length from the fiducial point of CAD geometry. The angle of incidence was also considered from -45° to 45° , which is the maximum range to be considered. If the VG changes to a larger angle, the VG1 which is the closest one to the wing penetrates into the wing surface.

Table 15 VG condition: Case 4.

# of VG	Chord length (c_{VG}/c_{mean})	Height (h_{VG}/c_{mean})	Angle of incidence ($^\circ$)	Streamwise position (X_{VG}/c_{mean})	Body position (β_{VG}/c_{mean})
1	0.1	0.01	Parameter	0.7	0.15
2	0.1	0.01	Parameter	0.7	0.20
3	0.1	0.01	Parameter	0.7	0.25

The comparison graphs are shown in Figures 77 and 78. The positive angle of the VG shows a good performance but the negatives are not good enough than initial value.

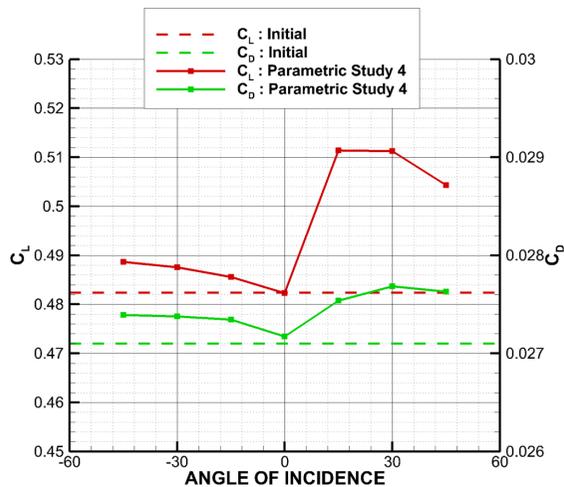


Figure 77 Parametric study Case 4: Comparison of C_L and C_D .

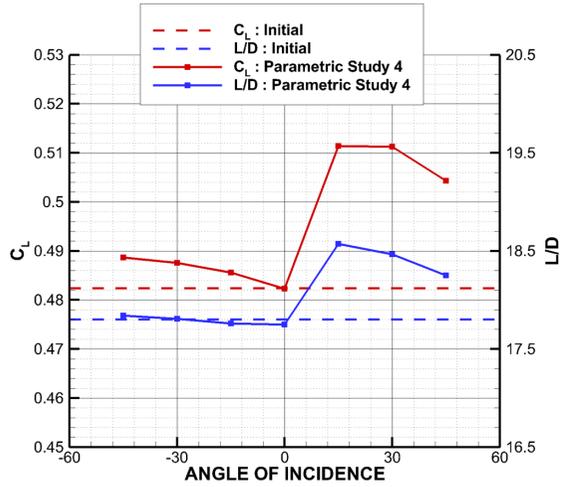


Figure 78 Parametric study Case 4: Comparison of C_L and L/D .

The VG having positive angle makes the flow stream downside although the negative angle of VG induces the upstream. Because the horseshoe vortex is originally upstream at $X_{VG}/c_{mean} = 0.7$, the negative angle will not have any effect on the horseshoe vortex. On the other hand, the positive angle of the VG blocks the

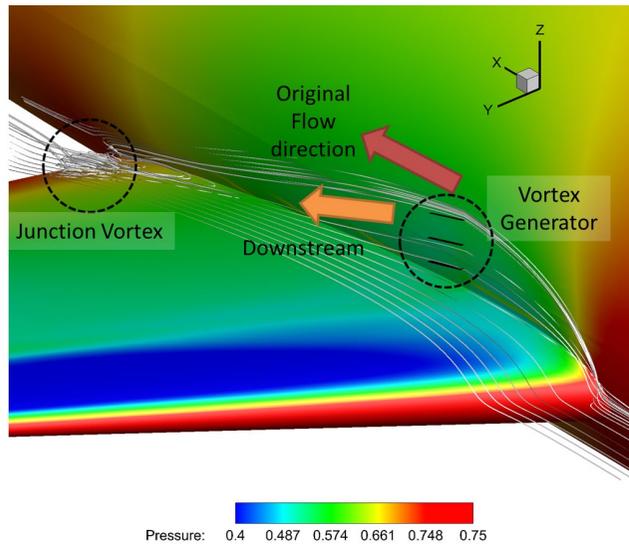


Figure 79 Parametric study Case 4: Flow direction.

horseshoe vortex and the induced downstream presses the original flow of the wing upper side, which delays the separation on the wing upper surface. Figure 79 shows the downstream induced by the VG.

The best angle of incidence is 15° , which is the same configuration with Case 2; therefore, the shape of the junction vortex, high-pressure region, and so forth is exactly same.

6.4.5 Case 5: Angle of Incidence, Body Surface, Front Side

In the above four parametric cases, the results show that the VG installed on the surfaces from the middle side of the wing to the trailing edge seems to show better performance than the VG located near the leading edge even in the body surface or the wing upper surface. The horseshoe vortex, however, is generated in front of the leading edge of the wing root. To investigate directly the influences of the VG on the development of the horseshoe vortex, the VGs were installed in the horseshoe vortex where they originated. Then, the angle of incidence was changed from -45° to 45° , which is the same condition of the cases 3 and 4.

Table 16 VG condition: Case 5.

# of VG	Chord length (c_{VG}/c_{mean})	Height (h_{VG}/c_{mean})	Angle of incidence ($^\circ$)	Streamwise position (X_{VG}/c_{mean})	Body position (β_{VG}/c_{mean})
1	0.1	0.01	Parameter	0.3	0.15
2	0.1	0.01	Parameter	0.3	0.20
3	0.1	0.01	Parameter	0.3	0.25

The results are similar with that of Case 4. The best angle of this case is positive 15° , and the VG with the zero angles also make better performance than both of the initial condition and the VG condition of Case 4. In front of the leading edge of the wing, the horseshoe vortex is generated, and it sharply rises to avoid the wing. Thus, the flow stream angle is higher than in that of Case 4, which means that the VG of 0°

also runs up against the horseshoe vortex even if the vortex is stronger than that of Case 4. The improvement of L/D is 3.51% at 15° , as shown in Figs. 80 and 81.

6.4.6 Case 6: Position, Body Surface, Under Wing

Similar to the fairings for the DLR-F6 that installed under the wing root, the sixth

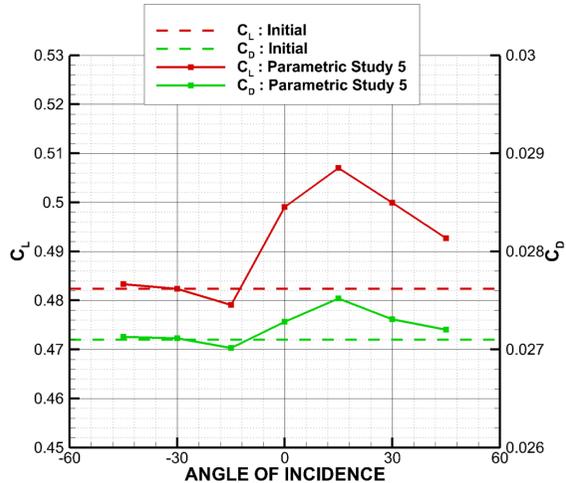


Figure 80 Parametric study Case 5: Comparison of C_L and C_D .

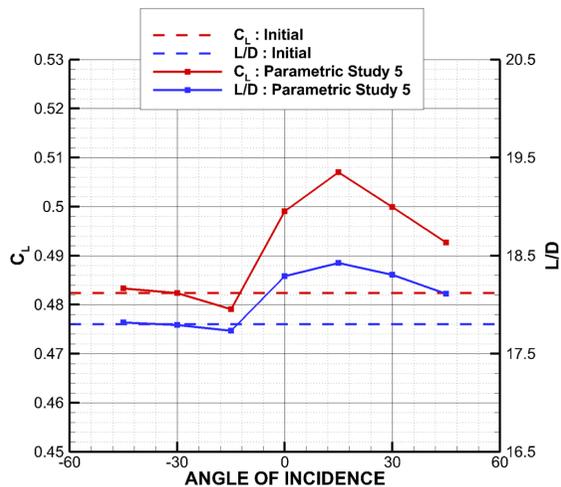


Figure 81 Parametric study Case 5: Comparison of C_L and L/D .

parametric study was conducted to identify the effectiveness of the VG installed under the wing root. These VGs were installed on the body surface and moved from in front of the leading edge to behind the trailing edge. To make the VGs symmetric to Case 2, the angle of incidence is set to -15° . The gaps from the VG to the wing surface are almost equal to the second case.

Table 17 VG condition: Case 6.

# of VG	Chord length (c_{VG}/c_{mean})	Height (h_{VG}/c_{mean})	Angle of incidence ($^\circ$)	Streamwise position (X_{VG}/c_{mean})	Body position (β_{VG}/c_{mean})
1	0.1	0.01	-15	Parameter	-0.15
2	0.1	0.01	-15	Parameter	-0.20
3	0.1	0.01	-15	Parameter	-0.25

To conclude, the VGs installed under the wing are not workable in every range from in front of the wing leading edge to the rear side of the trailing edge, which is proved by this parametric study. The result graphs are presented in Figs. 82 and 83.

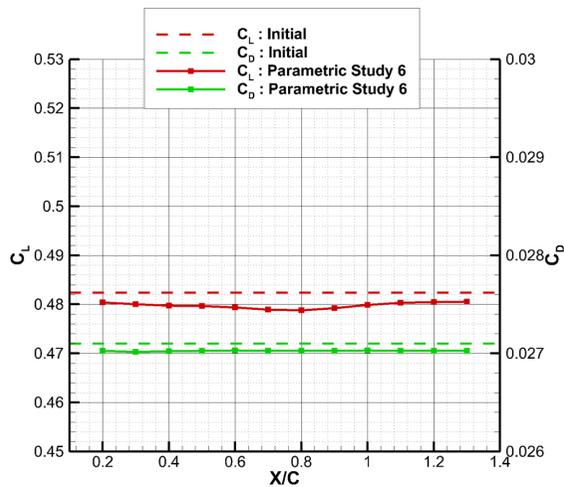


Figure 82 Parametric study Case 6: Comparison of C_L and C_D .

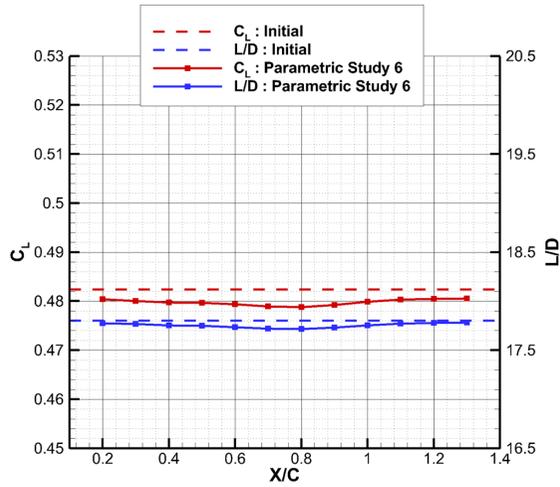


Figure 83 Parametric study Case 6: Comparison of C_L and L/D .

6.4.7 Case 7: Coupling, Position, Wing Upper Surface

In summarizing the above results of parametric study, except Cases 5 and 6, two types of VGs located on the wing surface and the body surface were considered at the same time. Because it is difficult to consider the streamwise position of two groups of each surface at once, three VGs on the wing upper surface were first moved. The initial streamwise position and the angle of incidence were decided by considering the results of Cases 1, 2, 3, and 4, which are summarized in Table 18.

Table 18 VG condition: Case 7.

# of VG	Chord length (c_{VG}/c_{mean})	Height (h_{VG}/c_{mean})	Angle of incidence ($^\circ$)	Streamwise position ($X_{VG}/c_{section, mean}$)	Body/wing spanwise position (β_{VG}/c_{mean})
1	0.1	0.01	-15	Parameter	0.55
2	0.1	0.01	-15	Parameter	0.60
3	0.1	0.01	-15	Parameter	0.65
4	0.1	0.01	15	0.5	0.15
5	0.1	0.01	15	0.5	0.20
6	0.1	0.01	15	0.5	0.25

The results are more complicated than when the VGs are installed on each surface. The comparison graphs of Figs. 84 and 85 show that the L/D increases while the VG location moves to the trailing edge of the wing. Because both the VG on the body surface and on the wing surface make delay of the development of junction vortex, the vortex are generated behind the vortex position of the Case 1, thus the very end VGs on the wing surface shows the best result. The performance improves 2.09% (from 17.7999 to 18.1724).

Figure 86 presents the flow stream and the shape of the junction vortex. The junction vortex become weaker and lower than the initial one, but the vortex is too wide to determine if it is the best solution. Moreover, the amount of the performance improvement is smaller than the improvement in Case 2 because the VGs on the body surface press the flow stream too much to the downward position, and the effectiveness of the VGs on the wing surface looks impaired.

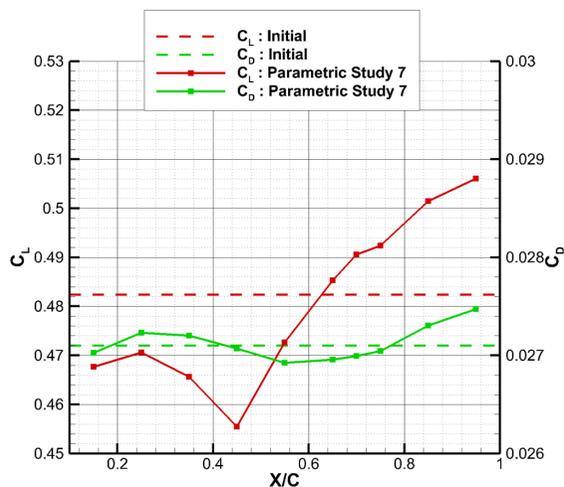


Figure 84 Parametric study Case 7: Comparison of C_L and C_D .

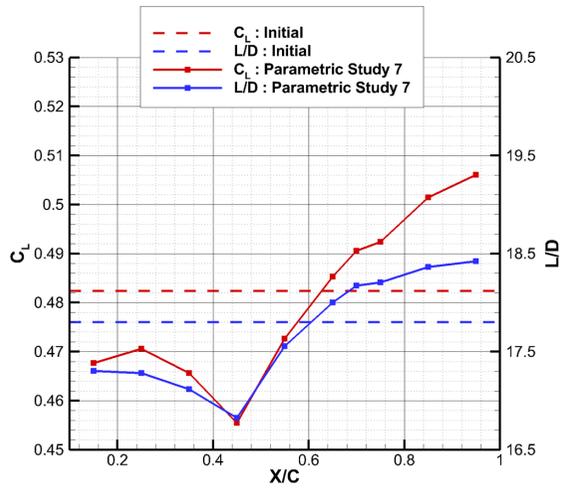


Figure 85 Parametric study Case 7: Comparison of C_L and L/D .

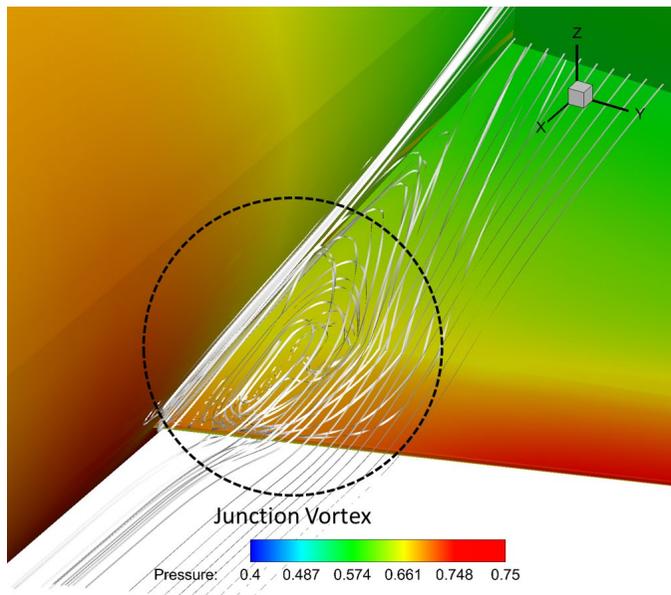


Figure 86 Parametric study Case 7: Junction vortex and high-pressure region on the trailing edge.

6.4.8 Case 8: Coupling, Position, Body Surface

Similar to the seventh parametric study, six VGs were installed and three VGs on the body surface were moved back and forth. The other parameters were the same as in Case 7.

Table 19 VG condition: Case 8.

# of VG	Chord length (c_{VG}/c_{mean})	Height (h_{VG}/c_{mean})	Angle of incidence ($^{\circ}$)	Streamwise position ($X_{VG}/c_{section\ or\ mean}$)	Body/wing spanwise position (β_{VG}/c_{mean})
1	0.1	0.01	-15	0.7	0.55
2	0.1	0.01	-15	0.7	0.60
3	0.1	0.01	-15	0.7	0.65
4	0.1	0.01	15	Parameter	0.15
5	0.1	0.01	15	Parameter	0.20
6	0.1	0.01	15	Parameter	0.25

As mentioned above, the interaction between the VGs is too complicated to estimate simply. This case fails to predict the conditions of the incidence angle and the β_{VG} position. The VGs on the body surface do not have any effect as the VGs move to the end, thus the performance is almost the same after $X_{VG}/c_{mean} = 1.3$, which is shown in Figs. 87 and 88. The result of the rear side is similar with the results of Case 1 that only consider the VG on the wing surface. The VGs on the body surface of the rear side only remove the tips of the horseshoe vortex as shown in Fig. 89, so the shape of junction vortex is narrow but slightly higher than the initial vortex shape.

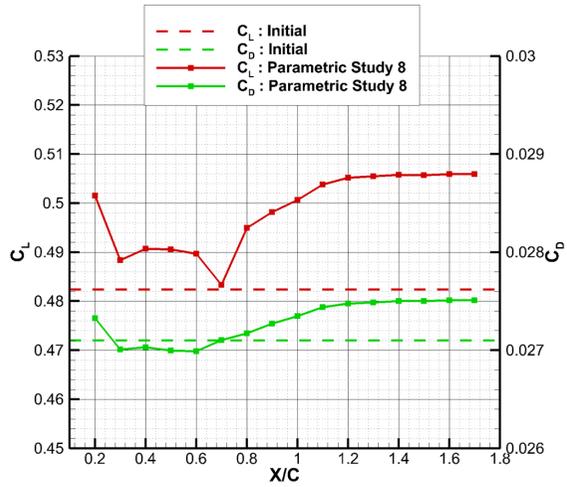


Figure 87 Parametric study Case 8: Comparison of C_L and C_D .

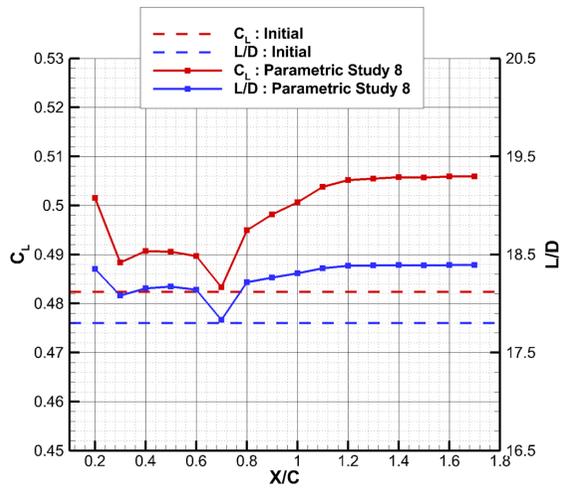


Figure 88 Parametric study Case 8: Comparison of C_L and L/D .

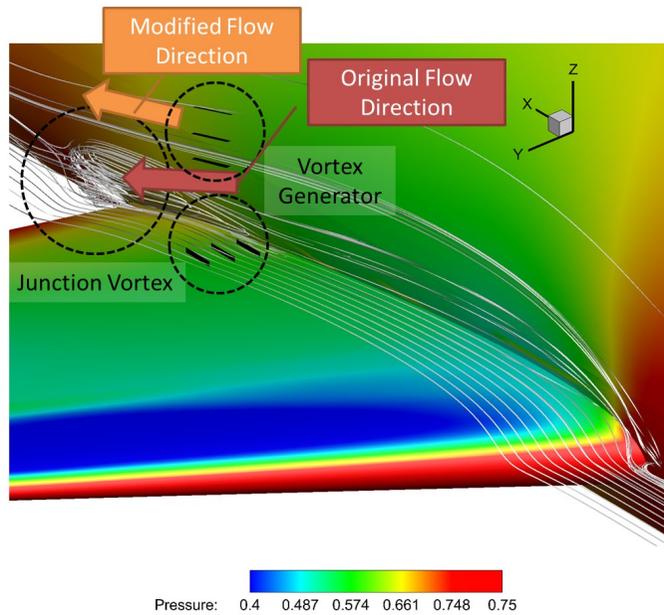


Figure 89 Parametric study Case 8: Flow direction with VG of rear side.

6.4.9 Case 9: Number, Wing Upper Surface

All of the parametric studies only considered three VGs for each surface except for this case. In this parametric study case, the number of VGs increased from 2 to 15 (from β_{VG}/c_{mean} is from 0.55 to 1.25), so the ranges of the VG region expanded along the spanwise direction of the wing upper surface. The streamwise position and the angle of incidence were selected from the Case 1, as summarized in Table 20.

Table 20 VG condition: Case 9.

# of VG	Chord length (c_{VG}/c_{mean})	Height (h_{VG}/c_{mean})	Angle of incidence ($^{\circ}$)	Streamwise position ($X_{VG}/c_{section}$)	Wing spanwise position (β_{VG}/c_{mean})
Parameter	0.1	0.01	-15	0.7	Parameter

Figures 90 and 91 show the comparison of the C_L , C_D , and L/D . As the number

of VGs increases, the L/D also increases. When the VGs are installed near the body, the improvement ratio of performance is slightly higher while its gradient is very flat as the additional VGs are posed far from the body. The effects of the VG are because the VGs near the body surface affect both the junction vortex and the separation flow on the wing upper surface, but the additional far-off VGs only functions the influence on delaying separation. The VGs far-off from the body are

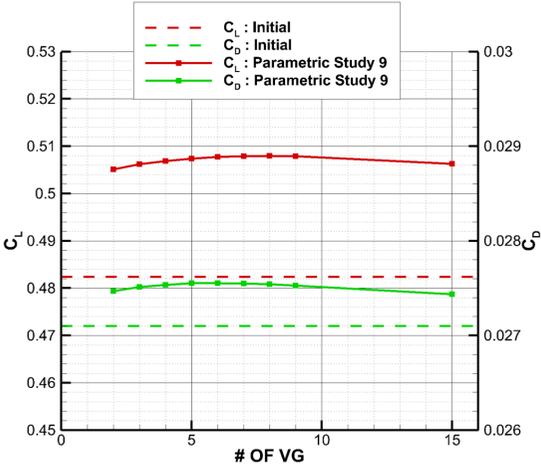


Figure 90 Parametric study Case 9: Comparison of C_L and C_D .

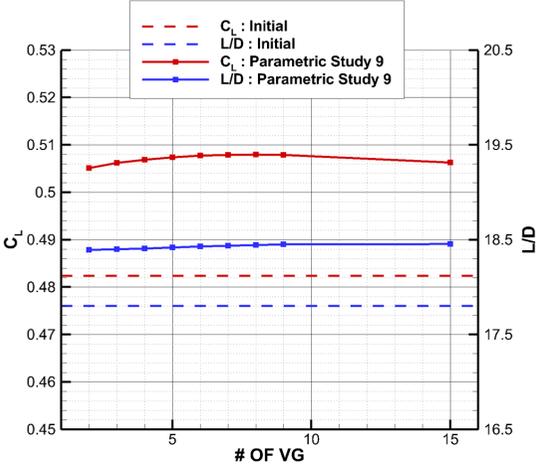


Figure 91 Parametric study Case 9: Comparison of C_L and C_D .

known to provide impressive performance on delaying stall characteristics [86].

6.4.10 Discussion of Parametric Study

Note that the VG installed for controlling the junction vortex shows better performance than initial condition in the parametric studies even if some cases failed to improve the performance of aircraft effectively. The VGs on each surface shows possibilities to eliminate the junction vortex, and the VGs on both surface also provide possibilities to remove that vortex, but Case 9 is not good at the shape of the vortex. The range of the VGs does not hinder the performance improvement while the VGs are expanded more and more in spanwise direction. The percentage of maximally improved performance is 4.34% in the ratio of lift to drag, which is

Table 21 VG configurations for optimization.

	Wing VG	Body VG	Combined VG	Plenty of VG
Chord length (c_{VG}/c_{mean})	0.1	0.1	0.1	0.1
Height (h_{VG}/c_{mean})	0.01	0.01	0.01	0.01
Angle of incidence (α_{VG})	-15°	15°	-15° (wing) 15° (body)	-15°
Streamwise position ($X_{VG}/c_{section}$)	0.7	-	0.7	0.7
Streamwise position (X_{VG}/c_{mean})	-	0.7	0.7	-
Body position (β_{VG}/c_{mean})	-	0.15 0.20 0.25	0.15 0.20 0.25	-
Wing spanwise position (β_{VG}/c_{mean})	0.55 0.60 0.65	-	0.55 0.60 0.65	0.55 ~ 1.0

large amount because the junction vortex only takes less than 1~3% in the surface area of the DLR-F6.

This study proposed four VG configurations from the results of parametric studies, which are summarized in Table 21. These are used in optimization as a baseline configuration of each design case.

6.5 Design Approach

Similar to the design of the VG in an S-duct, optimization was performed by using five design parameters for each VG, which were already used in the parametric study. The GBOM was used for the present VG design, and an adjoint variable method of discrete approach was employed to obtain the sensitivity information. The differentiable BAY model was also applied to describe the VGs. The DOT was selected as an optimizer, and the searching direction was determined by the Broyden-Fletcher-Goldfarb-Shanno (BFGS) method.

The elimination of the junction vortex of DLR-F6 was an objective of this study. Because there is not a well-known coefficient directly related to the size and the strength of the junction vortex, a maximization of L/D was selected as a substitute objective function in order to improve the overall performance of the DLR-F6. Because the L/D is directly related to the enhancement of both endurance and flying range, and because the junction vortex identified as a cause of the lift decrease during the process of understanding the flow physics, the substitution of the objective function for representing the characteristics of the junction vortex is reasonable. Then, the objective function was defined as

$$F = L/D = C_L/C_D \quad (6.4)$$

The design parameters include the chord length (c_{VG}), the height (h_{VG}), and the

angle of incidence (α_{VG}) of a VG. The parameters of the axial position and the circumferential position used in S-duct are changed to the streamwise position (X_{VG}) and the body position/wing to the spanwise position (β_{VG}), respectively. The last parameter depended on the surface where the VGs were installed. These parameters are non-dimensionalized by the mean aerodynamic chord (C_{mean}) or the chord length of sectional airfoil ($C_{airfoil}$). The design range is presented in Table 22.

Table 22 Design parameters and its range.

Design parameter	Lower bound	Initial value	Upper bound
Chord length (c_{VG}/c_{mean})	0.00	0.10	0.20
Blade height (h_{VG}/c_{mean})	0.000	0.010	0.020
Angle of incidence (α_{VG} [deg.])	0.0°	15.0°	30.0°
Streamwise position (X_{VG}/c_{mean} or $X_{VG}/c_{airfoil}$)	-0.50	0.0 (Baseline)	+0.50
Body position or Wing spanwise position (β_{VG}/c_{mean})	-0.025	0.0 (Baseline)	+0.025

6.6 Design Results

Two cases of design optimization were performed and the extra cases will be submitted as a future work. The first design case only considered three VGs on the wing surface, and the second design case dealt with the three VGs on the body surface. The baseline of the first design case and the second design case are the Wing VG and the Body VG of the Table 21. The performance of improvement was calculated by Eq. 6.3 that was already used in parametric study.

6.6.1 Design Case 1: From Wing VG

The first design was performed with total of 15 design variables with respect to three VGs on the wing upper surface. Using the GBOM design process, a designed VG configuration was obtained within 37 design iterations. The L/D increases from 18.3998 (baseline) to 18.7765 (designed), and the performance is improved 5.49% from the DLR-F6 without any VGs. Both of C_L and C_D increased together but the increasing ratio was different, which amount to, respectively, 8.51% and 2.87%. The lift coefficient increased from 0.482389 (without VG) and 0.506188 (baseline) to 0.523438 (designed), and the drag coefficient also increased from 0.027101 (without VG) and 0.027511 (baseline) to 0.027878 (designed). From the view point of the drag source, the pressure drag increased while the skin friction drag almost maintained. The number of sensitivity analyses was only 6, and the optimized result was obtained through 22 design iterations, which are shown in the Fig 92. This iteration is very small numbers compared to the design of VG in an S-duct, and this convergence characteristic indicates that the design space is less complicated than that of the S-duct design. If the numbers of VGs for the design increase, it is certain that the number of design iterations also increases.

After the design process, the chord length and the height of all VGs increased slightly, and the incidence angles enlarge. The closest VG to the body approaches

more to the body and moves forward. As a result, each designed VG has its unique position and size. The junction vortex, however, still remains but the strength and the size of the vortex is significantly reduced, which is shown in Figs. 93 and 94.

Figure 95 shows the sensitivity information of the baseline. Among the five design parameters, the height is the most sensitive parameter, which is the same as the preceding design of the S-duct. The VG1, the VG closest to the body surface, was the most sensitive VG among three VGs in terms of the height and the other parameters; thus the VG1 showed definite change in both of the shape and the position, but the VG3, the VG farthest from the body surface, was almost unchanged because all of the design variables were not sensitive.

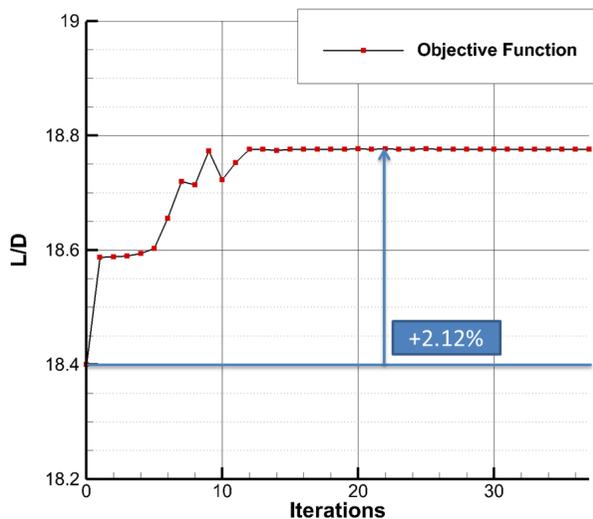


Figure 92 History of objective function: Design from ‘Wing VG’.

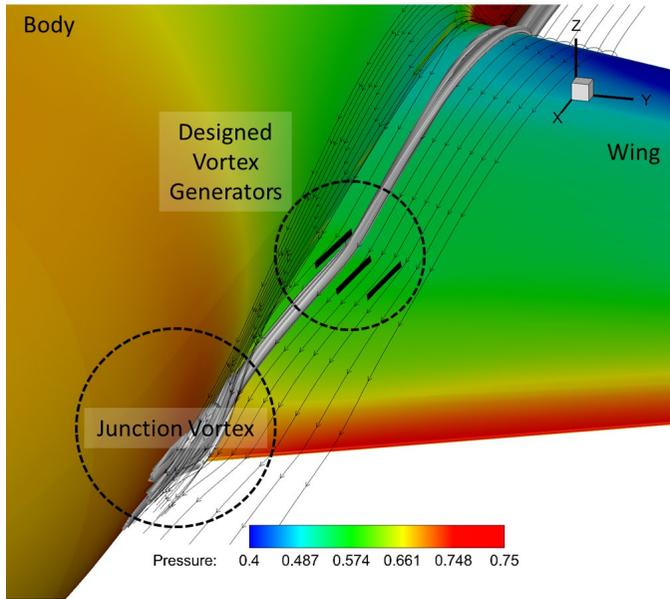


Figure 93 Design Case 1: Designed VG and pressure contour.

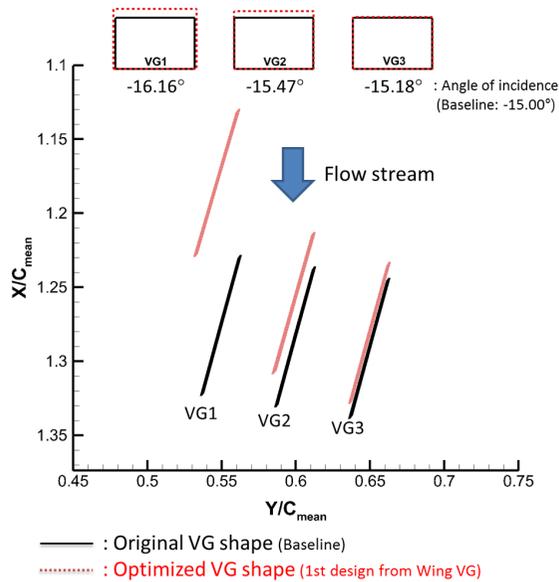


Figure 94 Design Case 1: Designed VG and their shapes and positions.

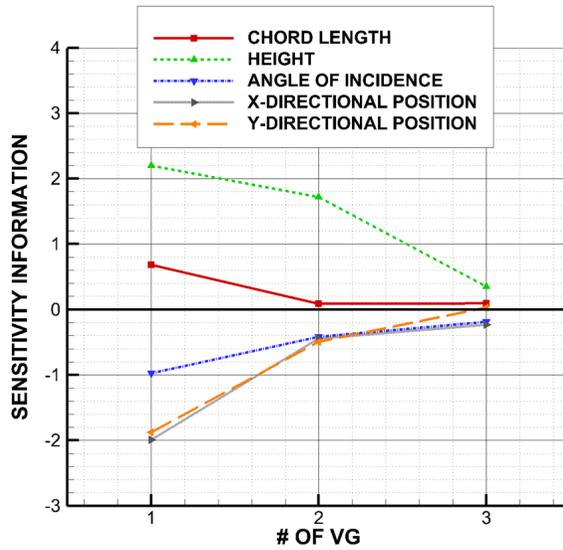


Figure 95 Sensitivity information of baseline (Design Case 1).

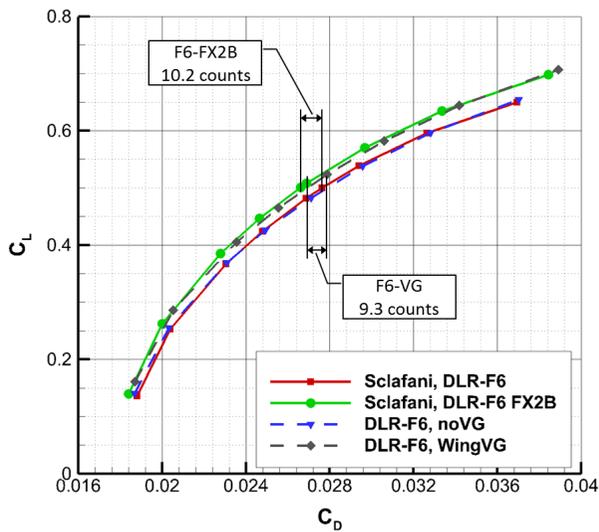


Figure 96 Drag polar: Design from 'Wing VG'.

The off-design performance of the optimized model was examined by changing the angle of attack, and then the results were plotted as drag polar, as illustrated in Fig. 96. The curve of drag polar moves to the left upper side, which indicates the improved performance in all off-design conditions. Although the amount of decreased drag by the VGs (9.3 counts) is smaller than that by the fairing (10.2 counts), the designed VGs showed highly good performance compared to the condition without the VGs. This result demonstrates the applicability of the present VG design approach in wide operating conditions of the external flow applications.

6.6.2 Design Case 2: From ‘Body VG’

The second design was conducted with total of 15 design variables with respect to the VGs on the body surface. The total number of design iteration was 32, and the number of sensitivity analysis was 4. The optimized result was obtained at 17 design iterations, and the history of the objective function is shown in Fig. 97. The optimized L/D is almost same with the baseline, which changed from 18.5716 (baseline) to 18.7228 (designed). However, the total improvement of aircraft performance by the VG is 5.19% from the DLR-F6 without VG configuration, which is not an inconsiderable value in terms of the area of the junction vortex region on the whole wing. Both of C_L and C_D also increased together like Design Case 1, which amount to, respectively, 6.87% and 1.60%. The lift coefficient increased from 0.482389 (without VG) and 0.511424 (baseline) to 0.515532 (designed), and the drag coefficient also increased from 0.027101 (without VG) and 0.027538 (baseline) to 0.027535 (designed).

In this case, the VGs on the body surface are not significantly changed because the baseline of this case, the Body VG, seems to be trapped in a local optimum already. The shape of junction vortex, the pressure contour, and the changes related to the shapes and the positions of each VG are illustrated in Figs. 98 and 99. The designed VGs indicate that the position of external VGs is the most effective

parameter among the five design parameters in this case although the sensitivity information that is shown in Fig. 100 shows that the height is the most sensitive parameter of the baseline.

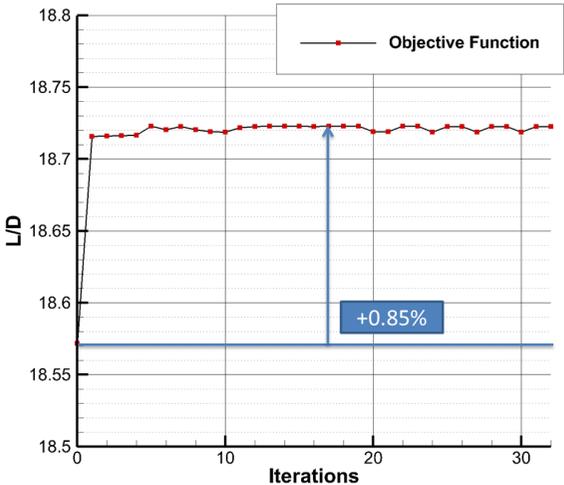


Figure 97 History of objective function: Design from ‘Body VG’.

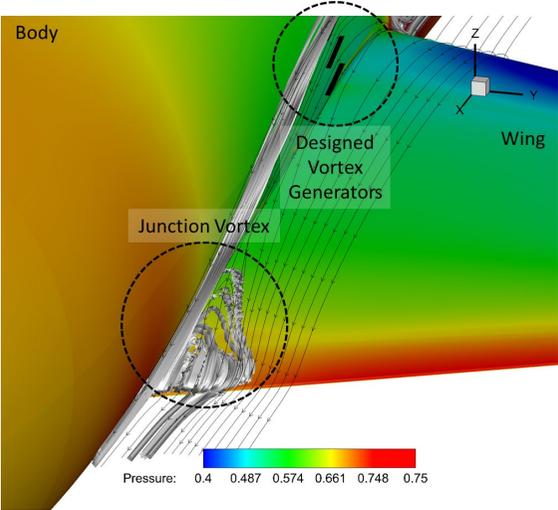


Figure 98 Design Case 2: Designed VG and pressure contour.

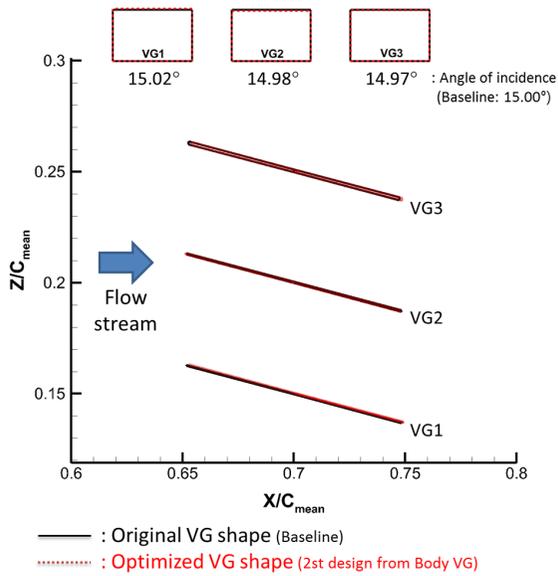


Figure 99 Design Case 2: Designed VG and their shapes and positions.

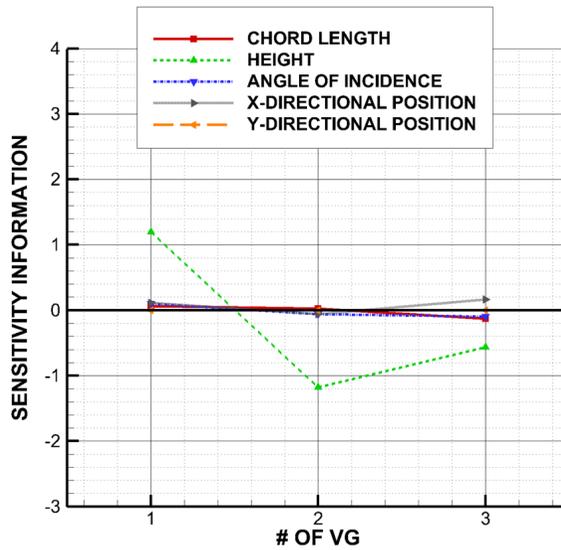


Figure 100 Sensitivity information of baseline (Design Case 2).

6.7 Flow Characteristics of DLR-F6

with Optimized VG Configurations and Discussion

Both of the VGs on the wing upper surface and the body surface showed considerably improved performance than before the VG installation even if the junction vortex is not eliminated perfectly. All of the optimized VGs make the junction vortex weaker, thereby expanding the high-pressure region of the trailing edge. Because the pressure increases of the wing lower surface follows this extension of a high-pressure region, the lift of the aircraft increases, and the drag also increases simultaneously because of the differences between the changed higher-pressure on the trailing edge and the undiversified pressure on the leading edge. Figure 101 compares the pressure coefficient of the wing between the results of without a VG and with a VG along the sectional airfoil at $y/\text{span} = 15\%$ in which the junction vortex located and Fig. 102 shows the results at $y/\text{span} = 23.9\%$ where the nearest junction vortex stands out. One interesting phenomenon is the similarity of the curve shape for the different shapes of junction vortex.

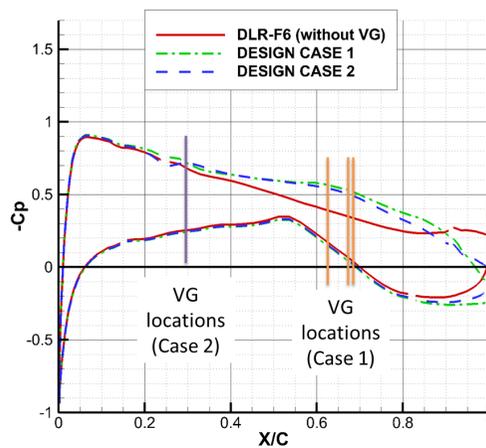


Figure 101 Pressure coefficient of DLR-F6 at $y/\text{span} = 15\%$.

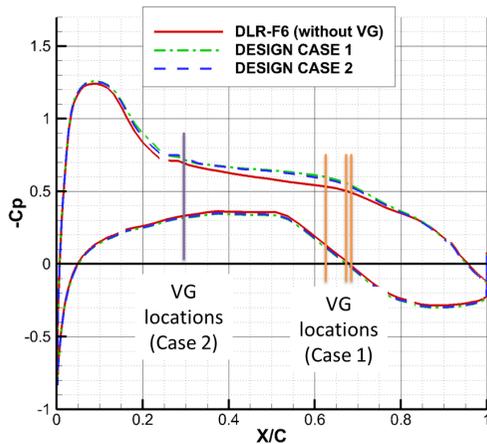


Figure 102 Pressure coefficient of DLR-F6 at $y/\text{span} = 23.9\%$.

As a result, two ways to weaken the junction vortex were discovered through the parametric study and the optimization study. In the case that the VG guides the flow direction to the inward to the body surface, as shown in Design Case 1, the junction vortex ascended up to the body surface, and the shapes of junction vortex are narrow and higher. On the contrary, the VG guiding the flow direction to the outward from the body surface, shown in Design Case 2, makes the wide junction vortex that must not be interrupted in order to be generated by the other flow streams. The amount of increased pressure and expended high-pressure region is almost the same in both of these cases. The size and shape of junction vortex on both cases are shown in Figs. 103 and 104.

Because the original objective is the elimination of the junction vortex, the VG making the smaller junction vortex better suits the proposed design purpose even if the amount of improved performance is smaller. In addition, the objective function, the ratio of lift to drag, is not suitable to eliminate the junction vortex perfectly, but this objective is acceptable in order to improve the performance of aircraft.

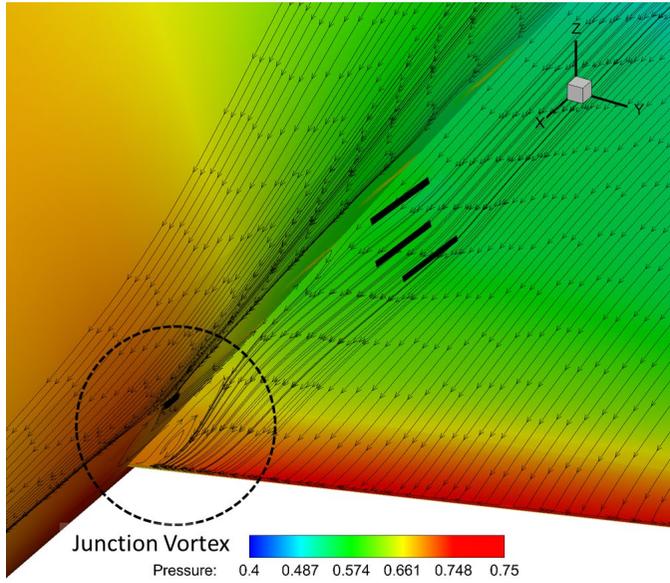


Figure 103 Small size junction vortex (Design Case 1).

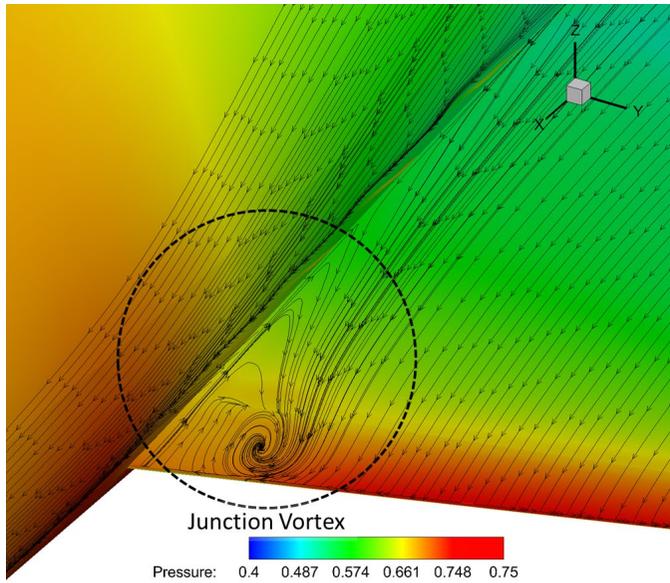


Figure 104 Large size junction vortex (Design Case 2).

Chapter VII

Concluding Remarks

7.1 Summary

The design optimizations of the Vortex Generator (VG) installed in the RAE M2129 S-shaped subsonic offset inlet and on the DLR-F6 wing-body configuration were conducted in this study. Each VG was optimized independently by fully reflecting the local flow pattern with geometric and positional parameters. To handle a large number of design variables, the discrete adjoint method with a VG source term model was adopted. As a source term model for sensitivity analysis, the differentiable BAY model was newly developed by adding the effect of positional parameters into the existing BAY model.

Following the design philosophy, the flow analysis and the design were performed step-by-step. The flow physics were first identified by using the re-designed efficient and the robust flow solver using the newly generalized parallel algorithm. To verify the accuracy of the flow solver, four cases for validation were performed. The flow solver and the adjoint solver including the BAY model and the differentiable BAY model were also validated by comparing each with the experimental data and the sensitivity information calculated by the complex step derivative method. By reflecting the results of parametric study to the baseline of the design, the optimized VG can successfully keep off the local optimum. Several optimizations were performed by the gradient-based optimization, and then the optimized VGs were tested in off-design conditions.

During the design of the internal flow application of the S-duct, the distortion

coefficient of the subsonic inlet was significantly reduced while the total pressure recovery ratio was maintained during the design of the VG. In the three cases for validation of the proposed design framework, the design parameters related to the position and the shape, which were separately examined by adopting the original BAY model and the differentiable BAY model. Among the results of five design cases, the optimized VG was obtained by design including all of the proposed design parameters including a total of 55 design variables. The resulting distortion coefficient decreased over 79% from the results of previous parametric research conducted by Anderson.

For the external flow application, the DLR-F6, the VGs were installed on the wing upper surface, on the wing lower surface, and on the body surface to investigate the effectiveness of VG to the junction vortex. Through the nine cases of parametric studies and the two cases of design studies, the way to control the junction vortex was discovered, and the ratio of lift to drag increased over 5% by the VG design. The two cases of design show different characteristics and induce different shapes of the junction vortices, but both of small and large size junction vortices weakened compared to the original junction vortex. The high-pressure region on the trailing edge was extended, which induced the improved performance of the aircraft. The percentage of improvement seems small, but it actually has a major influence on the aircraft's performance.

The designs of these two applications confirm that the proposed design approach based on the independent treatment of the design parameters for each VG leads to more efficient configurations. Although the present adjoint design approach may not guarantee the global optimum, several off-design tests maintain the improved performance over a wide range of operating condition, thereby supporting the claim that the proposed design approach is applicable in complex configurations of these kinds under a wide range of operating conditions.

7.2 Future Works

In this paper, the design of the VG on the wing-body configuration is not completely finished yet. Because the proposed objective function, the ratio of lift to drag, cannot perfectly represent the strength of junction vortex, the designed VGs do not perfectly eliminate the junction vortex; therefore, a new objective function that directly related to the junction vortex must be proposed, and new design cases will be conducted by using that function.

In addition, the bigger size VGs seems to have more possibilities to eliminate the junction vortex because the flow characteristics on the wing-body junction are more complicated and the boundary layer of the junction is thicker than that of the wing area farther from the body. The presented VG was decided from the comparison of the actual VGs on the wing upper surface and the normalized values of the VGs inside an S-duct, so the VGs can be small than the VGs that is actually needed. More large size VG, therefore, will be considered by conducting an additional parametric study or an additional design study.

The performance of aircraft with optimized VG will then be compared to the DLR-F6 with the fairing configuration. Although the fairings increase the weight and the volume of the aircraft, there certainly exists an improvement in performance. Thus, the endurance or the flying range can be compared, even if the increased weight and the increased volume of the fuel tank cannot perfectly estimate. Because the junction vortex undoubtedly interrupts the stability of aircraft, this detrimental phenomenon finally has to be removed.

References

- [1] Raymer, D. P., *Aircraft Design: A Conceptual Approach*, AIAA Education Series, 1989.
- [2] Jameson, A. and Ou, K. "Optimization Methods in Computational Fluid Dynamics," *Encyclopedia of Aerospace Engineering*, Edited by Richard Blockley and Wei Shyy, John Wiley & Sons, Ltd., ISBN: 978-0-470-68665-2, DOI: 10.1002/9780470686652, 2010.
- [3] Jameson, A., "Aerodynamic Design via Control Theory," *Journal of Scientific Computing*, Vol. 3, No. 3, 1988, pp.233-260.
- [4] Kim, H., "Aerodynamic Design of Transonic Wings Using Computational Design Methods," Ph.D. Dissertation, School of Mechanical and Aerospace Engineering, Seoul National University, Seoul, South Korea, 1999.
- [5] Kim, C. S., "Sensitivity Analysis for the Navier-Stokes Equations with Two-Equation Turbulence Models and Its Applications," Ph.D. Dissertation, School of Mechanical and Aerospace Engineering, Seoul National University, Seoul, South Korea, 2001.
- [6] Lee, B. J., "Aerodynamic Shape Optimization for Internal and External Flows via Discrete Adjoint Approach and Overset Mesh System," Ph.D. Dissertation, School of Mechanical and Aerospace Engineering, Seoul National University, Seoul, South Korea, 2007.
- [7] Yim, J., "Global-Local Multi-stage Shape Optimization Strategy for Three-dimensional Aircraft Configuration," Ph.D. Dissertation, School of Mechanical and Aerospace Engineering, Seoul National University, Seoul South Korea, 2012.
- [8] Kim, C. S., Kim, C., and Rho, O. H., "Sensitivity Analysis for the Navier-

- Stokes Equations with Two-Equation Turbulence Models,” *AIAA Journal*, Vol. 39, No. 5, 2001, pp.838-845.
- [9] Lee, B. J., and Kim, C., “Aerodynamic Redesign Using Discrete Adjoint Approach on Overset Mesh System,” *Journal of Aircraft*, Vol. 45, No. 5, 2008, pp.1643-1653.
- [10] Lee, B. J., Liou M.-S., and Kim, C., “Optimizing a Boundary-Layer-Ingestion Offset Inlet by Discrete Adjoint Approach,” *AIAA Journal*, Vol. 48, No. 9, 2010, pp.2008-2016.
- [11] Yim, J., Lee, B. J., and Kim, C., “Exploring Multi-Stage Optimization Strategy of Multi-Body Geometries Using Kriging-based Model and Adjoint Method,” *Computers & Fluids*, Vol. 68, 2012, pp. 71-87.
- [12] Jameson, A., “Aerodynamic Design and Optimization,” *16th AIAA Computational Fluid Dynamics Conference*, AIAA Paper 2003-3438, Orlando, FL, June 23-26, 2003.
- [13] Weck, O., Agte, J., Sobieszczanski-Sobieski, J., Arendsen, P., Morris, A., and Spieck, M., “State-of-the-Art and Future Trends in Multidisciplinary Design optimization,” *48th AIAA/ASME/ASCE/AHS/ASC Structures, Structural Dynamics, and Materials Conference*, AIAA Paper 2007-1905, Honolulu, Hawaii, April 23-26, 2007.
- [14] Jameson, A., Leoviriyakit, K., and Shankaran, S. “Multi-point Aero-Structural Optimization of Wings Including Planform Variations,” *45th AIAA Aerospace Sciences Meeting & Exhibit*, AIAA Paper 2007-764, Reno, NV, January 8-11, 2007.
- [15] Reuther, J., Alonso, J., Martins, J. R. R. A., and Smith, S. C., “A Coupled Aero-Structural Optimization Method for Complete Aircraft Configurations,” *37th AIAA Aerospace Sciences Meeting*, AIAA Paper 99-0187, Reno, NV, January 11-14, 1999.

- [16] Giesing, J. P., and Barthelemy, J.-F. M., "A Summary of Industry MDO Applications and Needs," *7th AIAA/USAF/NASA/ISSMO Symposium on Multidisciplinary Analysis and Optimization*, AIAA Paper 1998-4737, St. Louis, MO, September 2-4, 1998.
- [17] Dudek, J. C., "Modeling Vortex Generators in the Wind-US Code," NASA TM-2010-216744, July 2010.
- [18] Yi, J., Kim, C., and Lee, B. J., "Adjoint-Based Design Optimization of Vortex Generator in an S-shaped Subsonic Inlet," *AIAA Journal*, 2012, Vol. 50, No. 11, 2012, pp. 2492-2507.
- [19] 3rd AIAA CFD Drag Prediction Workshop, The American Institute of Aeronautics and Astronautics,
URL: <http://aac.larc.nasa.gov/tsab/cfdlarc/aiaa-dpw/Workshop3/> [Cited Oct. 2012]
- [20] Vassberg, J. C., Sclafani, A. J., and DeHaan, M. A., "A Wing-Body Fairing Design for the DLR-F6 Model: A DPW-III Case Study," *23rd AIAA Applied Aerodynamics Conference*, AIAA Paper 2005-4730, Toronto, Ontario, June 6-9, 2005.
- [21] Yi, J., and Kim, C., "Design Optimization of Vortex Generators for a Junction Vortex of Wing-Body Configuration by Discrete Adjoint Approach," *51st AIAA Aerospace Sciences Meeting*, Grapevine, TX, January 7-10, 2013.
- [22] Rogers, S. E., Suhs, N. E., and Dietz, W. E., "PEGASUS 5: An Automated Preprocessor for Overset-Grid Computational Fluid Dynamics," *AIAA Journal*, Vol. 41, No. 6, June 2003, pp. 1037-1045.
- [23] Roe, P. L., "Approximate Riemann Solver, Parameter Vectors, and Difference Schemes," *Journal of Computational Physics*, Vol. 43, 1981, pp. 357-372.
- [24] Liou, M.-S., and Steffen, C. J., Jr., "A new flux splitting scheme," *Journal of Computational Physics*, Vol. 107, 1993, pp. 23-39.

- [25] Kim, S., Kim, C., and Rho, O.-H., and Hong, S. K., “Cures for the Shock Instability: Development of a Shock-Stable Roe Scheme,” *Journal of Computational Physics*, Vol. 185, No. 2, 2003, pp. 342-374.
- [26] Liou, M.-S., “A Sequel to AUSM: AUSM+,” *Journal of Computational Physics*, Vol. 129, 1996, pp. 364-382.
- [27] Kim, K. H., Kim, C., and Rho, O.-H., “Methods for the Accurate Computations of Hypersonic Flows,” *Journal of Computational Physics*, Vol. 174, 2001, pp. 38-80.
- [28] Menter, F. R., “Two-Equation Eddy-Viscosity Turbulence Models for Engineering Applications,” *AIAA Journal*, Vol. 32, No. 8, August 1994, pp. 1598-1605.
- [29] Wilcox, D. C., *Turbulence Modeling for CFD*, DCW Industries, Inc., 5354 Palm Drive, La Canada, CA, 1993.
- [30] Wilcox, D. C., “Formulation of the k-omega Turbulence Model Revisited,” *AIAA Journal*, Vol. 46, No. 11, 2008, pp. 2823-2838.
- [31] Menter, F. R., Kuntz, M., and Langtry, R., “Ten Years of Industrial Experience with the SST Turbulence Model,” *Turbulence, Heat and Mass Transfer 4*, 2003, pp. 625-632.
- [32] Toro, E. F., *Riemann Solvers and Numerical Methods for Fluid Dynamics: A Practical Introduction*, Springer-Verlag, 1997, Chap. 13.
- [33] Kim, K. H., and Kim, C., “Accurate, Efficient and Monotonic Numerical Methods for Multi-Dimensional Compressible Flows. Part II: Multi-Dimensional Limiting Process,” *Journal of Computational Physics*, Vol. 208, No. 2, 2005, pp. 570-615.
- [34] Gottlieb, S., and Shu, C.-W., “Total Variation Diminishing Runge-Kutta Schemes,” *Mathematics of Computation*, Vol. 67, No. 221, January 1998, pp. 73-85.

- [35] Yoon, S., and Jameson, A., "Lower-Upper Symmetric-Gauss-Seidel Method for the Euler and Navier-Stokes Equation," *AIAA Journal*, Vol. 26, No. 9, 1988, pp. 1025-1026.
- [36] Ko, S. H., "Numerical Studies on the Separation Dynamics of a Strap-on Rocket Booster in the Next-generation Computing System," Ph.D. Dissertation, School of Mechanical and Aerospace Engineering, Seoul National University, Seoul, South Korea, 2008.
- [37] Martins, J. R. R. A., Sturdza, P., and Alonso, J., "The Complex-Step Derivative Approximation," *ACM Transactions on Mathematical Software*, Vol. 29, No. 3, 2003, pp.245-262.
- [38] Eleshaky, M. E., and Baysal, O., "Aerodynamic Shape Optimization Using Sensitivity Analysis on Viscous Flow Equations," *Journal of Fluid Engineering*, Vol. 115, No. 3, 1993, pp. 75-84.
- [39] Jameson, A., "Aerodynamic Design via Control Theory," *Journal of Scientific Computing*, Vol. 3, No. 3, 1988, pp. 233-260.
- [40] Jameson, A., Pierce, N. A., and Martinelli, L., "Optimum Aerodynamic Design Using the Navier-Stokes Equations," *35th AIAA Aerospace Sciences meeting and Exhibit*, AIAA Paper 97-0101, Reno, NV, January 6-9, 1997.
- [41] Jameson, A., "Re-Engineering the Design Process Through Computation," *35th AIAA Sciences Meeting & Exhibit*, AIAA Paper 97-0641, Reno, NV, January 6-9, 1997.
- [42] Kim, S., Alonso, J. J., and Jameson, A., "Multi-Element High-Lift Configuration Design Optimization Using Viscous Continuous Adjoint Method," *Journal of Aircraft*, Vol. 41, No. 5, 2004, pp. 1082-1097.
- [43] Nadarajah, S. and Jameson, A., "Studies of the Continuous and Discrete Adjoint Approaches to Viscous Automatic Aerodynamic Shape Optimization," *15th AIAA Computational Fluid Dynamics Conference*, AIAA Paper 2001-

2530, Anaheim, CA, June 11-14, 2001.

- [44] Wendt, B. J., "Initial Circulation and Peak Vorticity Behavior of Vortices Shed from Airfoil Vortex Generator," NASA CR-2001-211144, August 2001.
- [45] Bender, E. E., Anderson, B. H., and Yagle, P. J., "Vortex Generator Modeling for Navier-Stokes Codes," *3rd Joint ASME/JSME Fluids Engineering Conference, FEDSM Paper 99-6919*, American Society of Mechanical Engineering, New York, July 1999.
- [46] Jirásek, A., "A Vortex Generator Model and Its Application to Flow Control," *22nd AIAA Applied Aerodynamics Conference and Exhibit*, AIAA Paper 2004-4965, Providence, Rhode Island, August 16-19, 2004.
- [47] Goldsmith, E. L., and Seddon, J., *Practical Intake Aerodynamic Design*, AIAA Education Series, AIAA, Washinton, D. C., 1993, Chaps. 1-5.
- [48] Seddon, J., and Goldsmith, E. L., *Intake Aerodynamics*, AIAA Education Series, AIAA, New York, 1985, Chaps. 1, 2.
- [49] Menzies, R. D. D., "Investigation of S-Shaped Intake Aerodynamics Using Computational Fluid Dynamics," Ph.D. Dissertation, Department of Aerospace Engineering, Univ. of Glasgow, Glasgow, Scotland, U. K., 2002.
- [50] "Air Intakes for High Speed Vehicles," AGARD Advisory Rept., AGARD-AR-270, September 1991.
- [51] May, N. E., Peace, C. J., and Mchugh, C. A., "An Investigation of Two Intake/S-Bend Diffuser Geometries Using the Sauna CFD System - Phase 1," ARA Memo 386, 1993.
- [52] Abrahamsen, P. E. H., Pettersson-Reif, B. A., SaeTRAN, L., and FosSDal, J. B., "Air Intake Studies: Experimental Measurements and Computational Modelling," *RTO AVT Symposium on Missile Aerodynamics*, Sorrento, Italy, May 1998.
- [53] Kral, L. D., "Recent Experience with Different Turbulence Models Applied to

- the Calculation of Flow over Aircraft Components,” *Progress in Aerospace Sciences*, Vol. 34, Nos. 7-8, November 1998, pp. 520-529.
- [54] Menzies, R. D. D., Badcock, K. J., Barakos, G. N., and Richards, B. E., “Validation of the Simulation of Flow in an S-Duct,” *20th AIAA Applied Aerodynamics Conference*, AIAA Paper 2002-2808, St. Louis, MO, June 24-26, 2002.
- [55] Chevalier, M., and Peng, S.-H., “Detached Eddy Simulation of Turbulent Flow in a Highly Offset Intake Diffuser,” *Progress in Hybrid RANS-LES Modeling, Notes on Numerical Fluid Mechanics and Multidisciplinary Design*, Vol. 111, Springer-Verlag, Berlin/New York/Heidelberg, 2010, pp. 111-121.
- [56] Dudek, J. C., “Modeling Vortex Generator in the Wind-US Code,” NASA TM-2010-216744, July 2010.
- [57] Lee, B. J., and Kim, C., “Automated Design Methodology of Turbulent Internal Flow Using Discrete Adjoint Formulation,” *Aerospace Science and Technology*, Vol. 11, Nos. 2-3, 2007, pp. 163-173.
- [58] Anderson, B. H., and Gibb, J., “Study on Vortex Generator Flow Control for the Management of Inlet Distortion,” *Journal of Propulsion and Power*, Vol. 9, No. 3, 1993, pp. 422-430.
- [59] Dudek, J. C., “Empirical Model for Vane-Type Vortex Generators in a Navier-Stokes Code,” *AIAA Journal*, Vol. 44, No. 8, August 2006, pp. 1779-1789.
- [60] Anderson, B. H., and Gibb, J., “Vortex-Generator Installation Studies on Steady-State and Dynamic Distortion,” *Journal of Aircraft*, Vol. 35, No. 4, 1998, pp. 513-520.
- [61] Jirásek, A., “Design of Vortex Generator Flow Control in Inlets,” *Journal of Aircraft*, Vol. 43, No. 6, November-December 2006, pp. 1886-1892.
- [62] Allan, B. G., Owens, L. R., and Lin, J. C., “Optimal Design of Passive Flow

Control for a Boundary-Layer-Ingesting Offset Inlet Using Design-of-Experiments,” *44th AIAA Aerospace Sciences Meeting and Exhibit*, AIAA Paper 2006-1049, Reno, NV, January 9-12, 2006.

- [63] Lee, B. J., and Liou, M. S., “Re-Design of Boundary Layer Ingesting Offset Inlet via Passive Flow Control Manner,” *48th AIAA Aerospace Sciences Meeting Including the New Horizons Forum and Aerospace Exposition*, AIAA Paper 2010-842, Orlando, FL, .January 4-7, 2010.
- [64] Levi, D. W., Zickuhr, T., Vassberg, J., Agrawal, S., Wahls, R. A., Pirzadeh, S., and Hemsch, M. J., “Summary of Data from the First AIAA CFD Drag Prediction Workshop,” *40th AIAA Aerospace Sciences Meeting*, AIAA Paper 2002-0841, Reno, NV, January 14-17 , 2002.
- [65] Laflin, K. R., Vassberg, J. C., Wahls, R. A., Morrison, J. H., Brodersen, O., Rakowitz, M., Tinoco, E. N., Godard, J., “Summary of Data from the Second AIAA CFD Drag Prediction Workshop,” *42nd AIAA Aerospace Sciences Meeting and Exhibit*, AIAA Paper 2004-0555, Reno, NV, January 5-8, 2004.
- [66] Vassberg, J. C., Tinoco, E. N., Mani, M., Brodersen O. P., Eisfeld, B., Wahls, R. A., Morrison, J. H., Zickuhr, T., Laflin, K. R., and Mavriplis, D. J., “Summary of the Third AIAA CFD Drag Prediction Workshop,” *45th AIAA Aerospace Sciences Meeting and Exhibit*, AIAA Paper 2007-0260, Reno, NV, January 8-11, 2007.
- [67] Vassberg, J. C., Tinoco, E. N., Mani, M., Rider, B., Zickuhr, T., Levy, D. W., Brodersen, O. P., Eisfeld, B., Crippa, S., Wahls, R. A., Morrison, J. H., Mavriplis, D. J., and Murayama, M., “Summary of the Fourth AIAA CFD Drag Prediction Workshop,” *28th AIAA Applied Aerodynamics Conference*, AIAA Paper 2010-4547, Chicago, IL, June 28-July 1, 2010.
- [68] Rossow, C. -C., Godard, J. -L., Hoheisel, H., Schmitt, V., “Investigations of Propulsion Integration Interference Effects on a Transport Aircraft

- Configuration,” *Journal of Aircraft*, Vol. 31, No. 5, 1994, pp. 1022-1030.
- [69] Meakin, R. L., “Object X-Rays for Cutting Holes in Composite Overset Structured Grids,” *15th AIAA Computational Fluid Dynamics Conference*, AIAA Paper 2001-2537, Anaheim, CA, June 11-14, 2001.
- [70] Noack, R. W., and Belk, D. M., “Improved Interpolation for Viscous Overset Grids,” *35th AIAA Aerospace Sciences Meeting & Exhibit*, AIAA Paper 97-0199, Reno, NV, January 6-9, 1997.
- [71] Chan, W. M., and Buning, P. G., “Zipper Grids for Force and Moment Computation on Overset Grids,” *12th AIAA Computational Fluid Dynamics Conference*, AIAA Paper 1995-1681, San Diego, CA, June 19-22, 1995.
- [72] NPARC Alliance CFD Verification and Validation, NASA,
URL: <http://www.grc.nasa.gov/WWW/wind/valid/validation.html> [Cited Oct. 2012]
- [73] Cook, P. H., McDonald, M. A., and Firmin, M. C. P., “Aerofoil RAE 2822 – Pressure Distribution, and Boundary Layer and Wake Measurements,” *Experimental Data Base for Computer Program Assessment*, AGARD Report AR 138, 1979.
- [74] Sclafani, A. J., Vassberg, J. C., Harrison, N. A., DeHaan, M. A., Rumsey C. L., Rivers, S. M., and Morrison, J. H., “Drag Prediction for the DLR-F6 Wing/Body and DPW Wing Using CFL3D and OVERFLOW on an Overset Mesh,” *45th AIAA Aerospace Sciences Meeting and Exhibit*, AIAA Paper 2007-0257, Reno, Nevada, January 8-11, 2007.
- [75] Tinoco, E. N., Venkatakrishnan, V., Winkler, C., and Mani, M., “Structured and Unstructured Navier-Stokes Solvers for the Third Drag Prediction Workshop,” *Journal of Aircraft*, Vol. 45, No. 3, 2008, pp. 738-749.
- [76] Multidisciplinary Design Optimization Laboratory
URL: <http://mdolab.engin.umich.edu/> [Cited Oct. 2012]

- [77] Nocedal, J., and Wright, S. J., *Numerical Optimization*, Springer, 1999.
- [78] VMA Engineering, *DOT User Manual*, Vanderplaats, Miura, and Associates, Inc., 1993.
- [79] Miller, D. S., *Internal Flow System: Design and Performance Prediction*, 2nd ed.. Gulf Publishing Co., Houston, TX, 1990, Chap. 5.
- [80] Nadarajah, S. K., and Jameson, A., “Optimum Shape Design for Unsteady Flows with Time-Accurate Continuous and Discrete Adjoint Methods,” *AIAA Journal*, Vol. 45, No. 7, July 2007, pp. 1478-1491.
- [81] Redeker, G., Schmidt N., and Müller R., “Design and Experimental Verification of a Transonic Wing for Transport Aircraft,” *Proceedings of the FDP Symposium on Subsonic/Transonic Configuration Aerodynamics*, AGARD CP-285, 1980, pp. 13.1-13.7.
- [82] Brodersen, O., and Stürmer, A., “Drag Prediction of Engine-Airframe Interference Effects using Unstructured Navier-Stokes Calculations,” *19th AIAA Applied Aerodynamics Conference*, AIAA Paper 2001-2414, Anaheim, CA, June 11-14, 2001.
- [83] Rossow, C. -C., Godard, J. -L., Hoheisel, H., Schmitt, V., “Investigations of Propulsion Integration Interference Effects on a Transport Aircraft Configuration,” *Journal of Aircraft*, Vol. 31, No. 5, 1994, pp. 1022-1030.
- [84] Anderson, J. D., Jr., *Introduction to Flight*, 4th ed., McGraw-Hill, 2000, Chaps. 6-7.
- [85] Stein, D. E., “Vortex Generator,” Smart Cockpit Database, URL: http://www.smartcockpit.com/data/pdfs/flightops/aerodynamics/Vortex_Generators.pdf [cited Oct 2012]
- [86] Huang, J., Fu, S., Xiao, Z., and Zhang M., “Study of Separation Control of Vortex Generators on Transonic Wings,” *Journal of Fluid Science and Technology*, Vol. 6, No. 1, 2011, pp. 85-97.

- [87] Sclafani, A. J., DeHaan, M. A., and Vassberg, J. C., "OVERFLOW Drag Prediction for the DLR-F6 Transport Configuration; A DPW-II Case Study," *42nd AIAA Aerospace Sciences Meeting and Exhibit*, AIAA Paper 2004-0393, Reno, NV, Jan. 5-8, 2004.
- [88] Fleming, J., Simpson, R., Cowling, J., and Devenport, W., "An Experimental Study of a Turbulent Wing-Body Junction and Wake Flow," *Experiments in Fluids*, Vol. 14, 1993, pp. 366-378.
- [89] Mehta, R., "Effect of Wing Nose Shape on the Flow in a Wing Body Junction," *The Aeronautical Journal*, Vol. 88, 1984, pp. 456-460.
- [90] Gand, F., Brunet, V., and Deck, S., "A Combined Experimental, RANS and LES Investigation of a Wing Body Junction Flow," *40th Fluid Dynamics Conference and Exhibit*, AIAA Paper 2010-4753, Chicago, IL, Jun. 28- Jul. 1, 2010.
- [91] Simpson, R. L., "Junction Flows," *Annual Review of Fluid Mechanics*, Vol. 33, 2001, pp.415-443.
- [92] Bradshaw. P., "Turbulent Secondary Flows," *Annual Review of Fluid Mechanics*, Vol. 19, 1987, pp.53-74.
- [93] Bragg, G., "The Turbulent Boundary Layer in a Corner," *Journal of Fluid Mechanics*, Vol. 36, No. 3, 1969, pp. 485-503.
- [94] Nakayama, A., and Rahaij, H., "Measurements of Turbulent Flow Behind a Flat Plate Mounted Normal to the Wall," *AIAA Journal*, Vol. 22, No. 12, 1984, pp. 1817-1819.
- [95] Gessner, F., "The Origin of Secondary Flow in Turbulent Flow along a Corner," *Journal of Fluid Mechanics*, Vol. 58, No. 1, 1973, pp. 1-25.
- [96] Barber, T., "An Investigation of Strut-wall Intersection Losses," *Journal of Aircraft*, Vol. 15, No. 10, 1978, pp. 676-684.

This page is blank

Appendix A

Parallel Algorithm

The main point of the improvement in the flow solver is the parallel algorithm for highly complex and large scale multi-block structure. This algorithm is based on the structured multi-block including the twisted and separated interfaces.

Figure A-1 shows the sample grid composed of 9 blocks and the interface for transferring the data. The PI indicates the physical boundaries of *i*-direction, and the PJ show the *j*-directional physical boundaries. The symbols of A to I indicate block, and I or J is interfaces between the blocks.

A previously developed algorithm applied the sequential data transfer processing algorithm for communication. After finishing the communication of *i*-direction, the *j*-directional communication starts, and then the *k*-directional data transfer occurs by stage or the inverse direction was adopted from *k*- to *i*-directions. As the number of

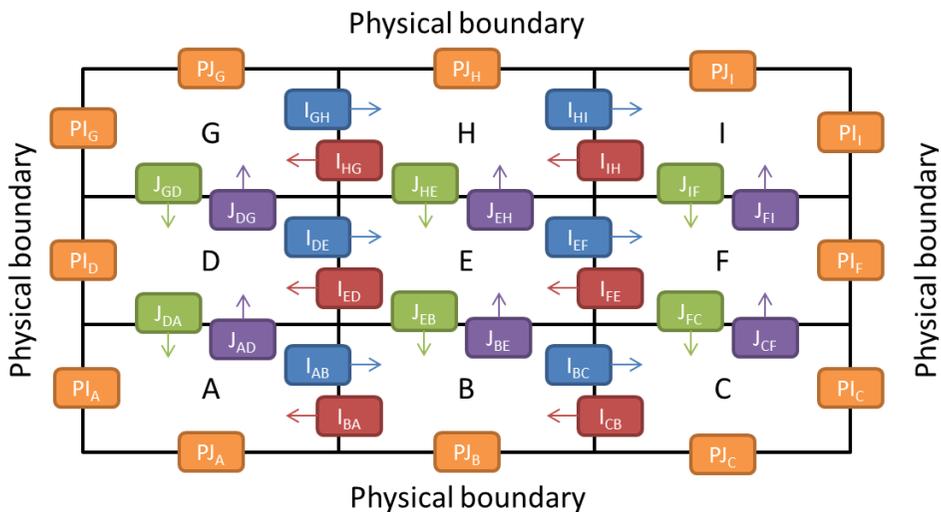


Figure A-1 Sample grid for parallel algorithm.

interfaces for data transfer increases, the communications are delayed, and many interfaces wait their turn. When the interfaces are in line with large size transfer data, the communications have reached a deadlock, as shown in Fig. A-2. This situation can be corrected by using the non-blocking communication, but this solution cannot be used when the data size is larger than the buffer size of hardware.

The previous algorithm is performed as

- 1) The left interface of a direction (i -, j -, or k -) of the block ready for sending the data by calling MPI_SEND type command.
- 2) The right interface of a direction of the block start to receive the data by calling MPI_RECV type command.
- 3) The right interface of the block start to send the data by calling MPI_SEND type command after finishing the process 2)
- 4) The left interface starts to receive the data and then the communications of the other direction starts in order.

This process is illustrated in Fig. A-3. This type of communication is inefficient for such a large-scale problem.

If there is never a physical boundary in a direction, all of the blocks call

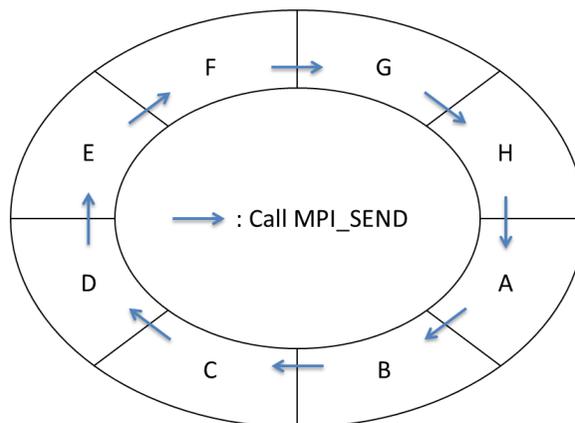


Figure A-2 Dead lock condition.

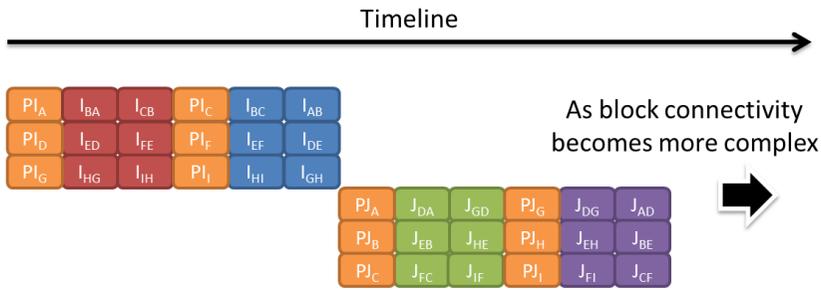


Figure A-3 Timeline of previous algorithm.

MPI_SEND command at first, as illustrated in Fig. A-2, which means all the blocks try to send the data but no one is ready to receive. This situation is okay when the data size is lower than the buffer size, but it is not okay if there is a large data size. As a result, the communication reaches a deadlock. In addition, as the number of blocks increase along the directions, the blocks' connectivity becomes more complex, indicating that the time requirement is directly influenced from the number of blocks. If the number of blocks increases, the time requirement also increases along the timeline.

The improved parallel algorithm considers each interface separately. Each separated interface performs by sending and receiving processes at one time for two related blocks. There are not any relations between the interfaces, which give an advantage that each interface independently performs its communication between the blocks. The individuality gives an advantage that the several communications can transfer data simultaneously. Furthermore, the twisted interface can be treated because the interface does not have fixed index information. Figure A-4 presents the process of the new parallel algorithm applied in this study. By using this algorithm, the time requirement is not directly connected to the increase of the block numbers. As the number of block increases, the time needs are also increased along the timeline, but the amount is really smaller than the original algorithm. Instead of the time needs, the waiting lines between the blocks start to communicate at the same

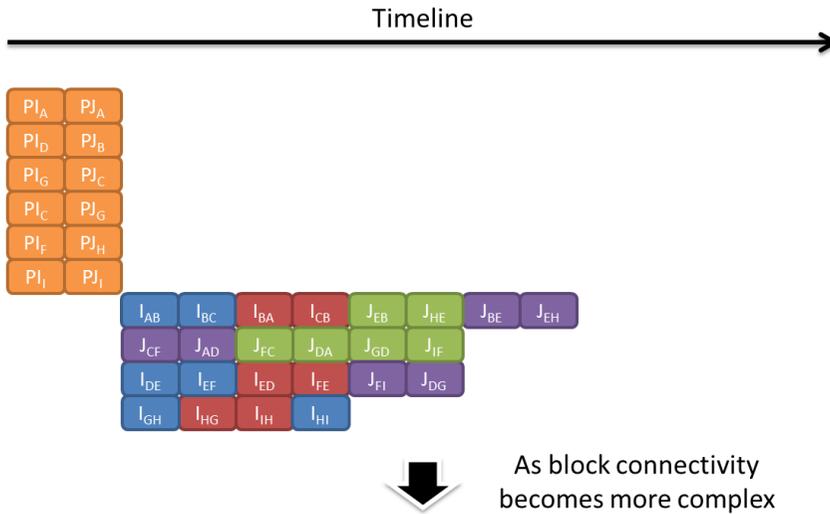


Figure A-4 Timeline of developed algorithm.

time.

This algorithm is based on the MPImap constructed in the pre-process. By providing more flexibility, this algorithm can treat a twisted interface, a separated interface, wall-interface combined boundary condition, and so forth. This map is composed of 6 parameters of the hither-side related for receiving and 8 parameters of the opposite-side for sending in an interface. The parameters related to the hither-side includes the process number, surface direction and surface location, start point of n -direction, end point of n -direction, start point of m -direction, and end point of m -direction when the interface has $m \times n$ dimensions. The opposite-side has sending information of the process number, opposite side surface, line information related to the n -direction, start point mated to the hither-side start point on n -direction, end point, line information related to the m -direction, start point, and end point of this direction. These parameters are illustrated in Fig. A-5.

The algorithm is performed as follows:

- 1) Make MPImap for every interface if it is twisted, separated, or includes wall-interface boundary condition.
- 2) Stand all of the MPImaps in order, and make MPImap-list.

- 3) Sort the MPImap-list to avoid the interface next to the attached block.
- 4) Do the sending-receiving procedure according the turns on the MPImap-list.
If the processor is related to the turn, the communication routine is activated although the dis-related processor passes a turn. So all the processor can find its turn at a time, the sending-receiving process performed simultaneously.

In the case if one boundary in a block having a wall-interface combined condition, the wall boundary first adopts to all cells on the boundary. Then, the interfaces start to transfer the data including properties of next block. After this procedure, the partial cells related to the wall surface have wall boundary condition and the other cells have interface boundary condition.

The developed algorithm is extremely useful in a problem of a complex geometry, and it can be used in both of structured multi-block, structured overset, and unstructured grid topologies.

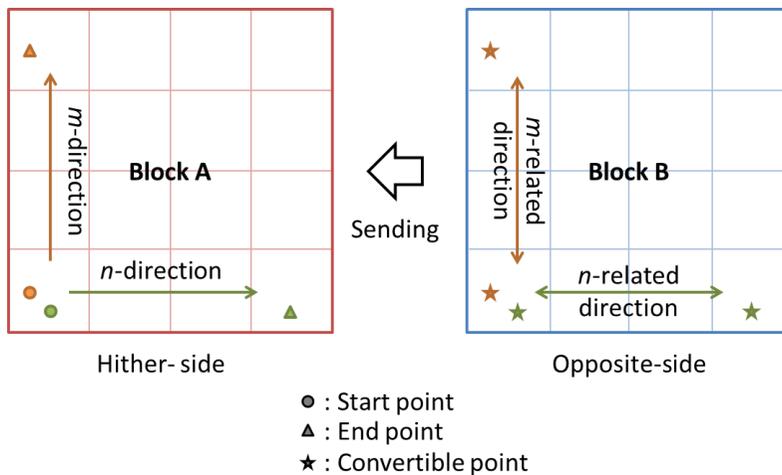


Figure A-5 Parameters related to the MPImap.

Appendix B

Verification of BAY type model

To check the available angle of incidence of the vortex generator (VG) that can be described by BAY type models, the computed result using the differentiable BAY model was compared to the results of the fully gridded analysis. A rectangular shaped VG was installed on a flat plate, and the case applied the geometric size information and the flow conditions of the RAE M2129 S-duct. The geometric schematic is illustrated in Fig. B-1.

The chord length and the height of the single VG is the same as the VG used for the S-duct mentioned in Chapter V. The chord length was 0.280 and the blade height was 0.07, and the VG had zero thickness. The flow analysis at incidence angles of 15°, 30°, 45°, and 60° were conducted. Free stream Mach number is 0.794, and Reynolds number is 0.924 million. The grid for VG source term model has 1 million cells and the grid for gridded VG has 2 million cells. Both of grids were generated

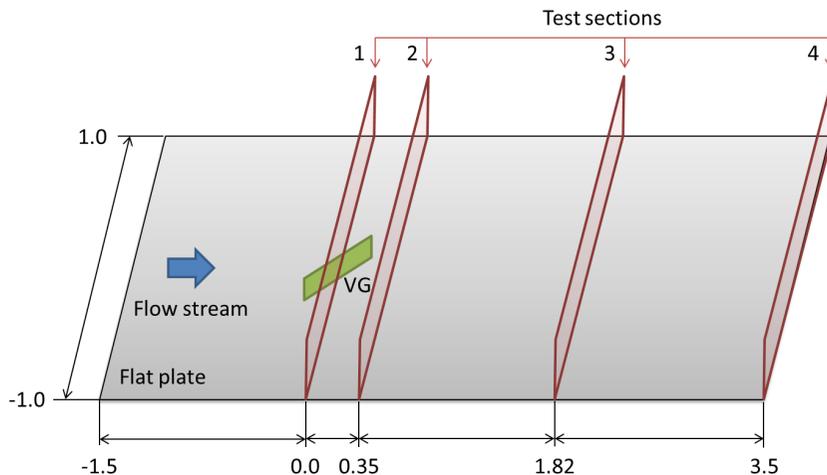


Figure B-1 Test geometry.

for viscous calculation using $k-\omega$ SST turbulent model; thus the first cell y^+ value was set to 1. Figure B-2 shows the grid for source term model, and Fig. B-3 shows the sample grid for the fully gridded analysis.

Comparisons of Mach number contour and vorticity contour are shown in Figs.

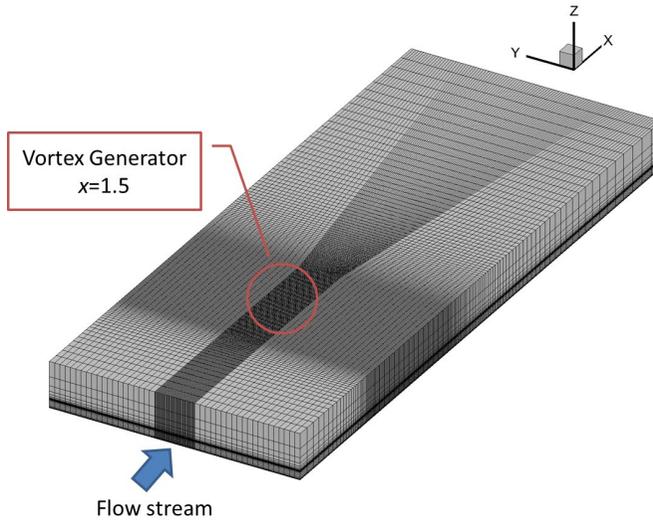


Figure B-2 Grid topology for VG source term model.

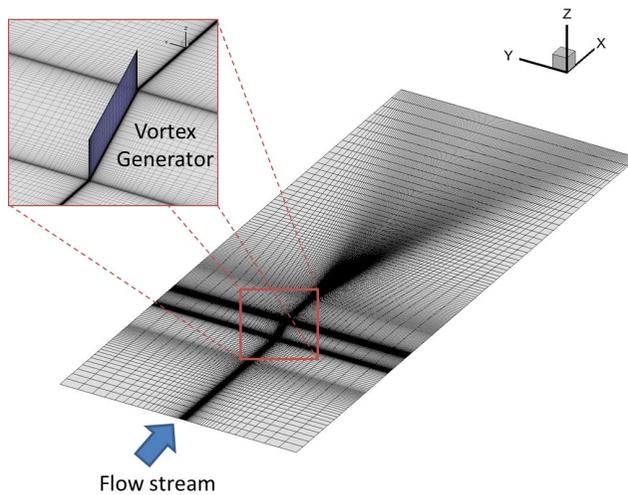


Figure B-3 Grid topology for fully gridded analysis ($\alpha_{VG}=15^\circ$).

B-4 and B-5. Four axial sections measured from the VG center point are shown. From -30° to 30° , the flow analysis using the VG source term model well agreed with the result of the fully gridded analysis. However, the outer regions, from -60° to -30° and from 30° to 60° , show a similar result in primary flow pattern, such as curved flows to avoid the VG and upstream flows to jump over the VG, in both of model and gridded analysis. Some detail flow pattern near the VG, such as bounced flows and wakes originated from the low pressure behind the VG, were not described well by the mathematical model, which phenomena are started to observe at the incidence angle of 45° . By using the BAY type models, the quality of the physical properties, such as the vorticity and the Mach number, can be described well in all range of test conditions, but the quantity of these properties were lower than that of gridded analysis. The local flow patterns near the VGs are compared in Figs. B-6 and B-7, which illustrated with Mach number contour.

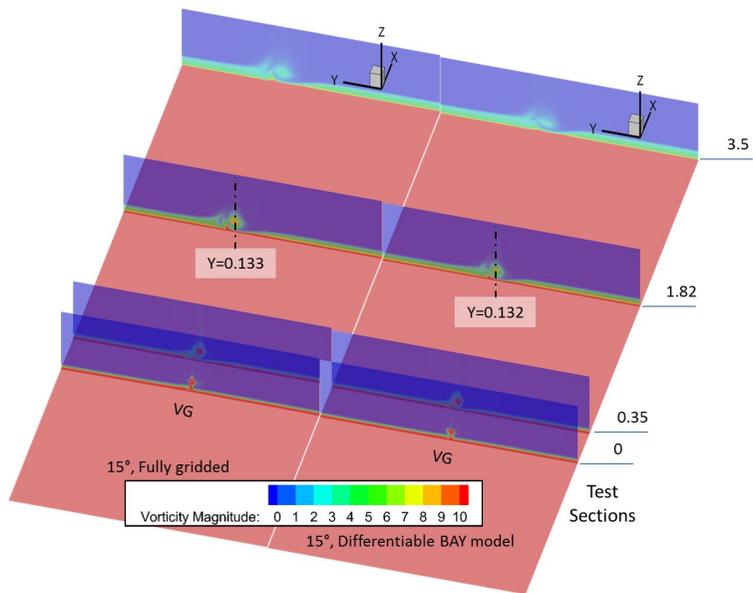


Figure B-4 (a) Vorticity contour ($\alpha_{VG}=15^\circ$).

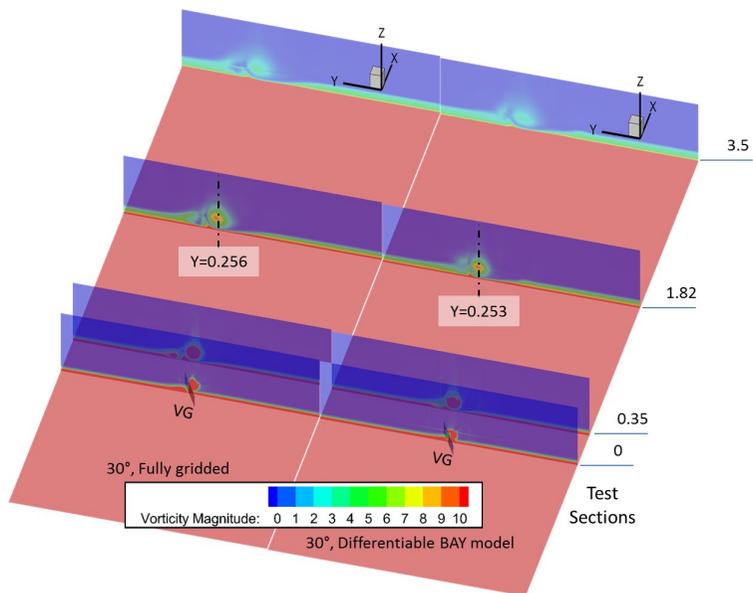


Figure B-4 (b) Vorticity contour ($\alpha_{VG}=30^\circ$).

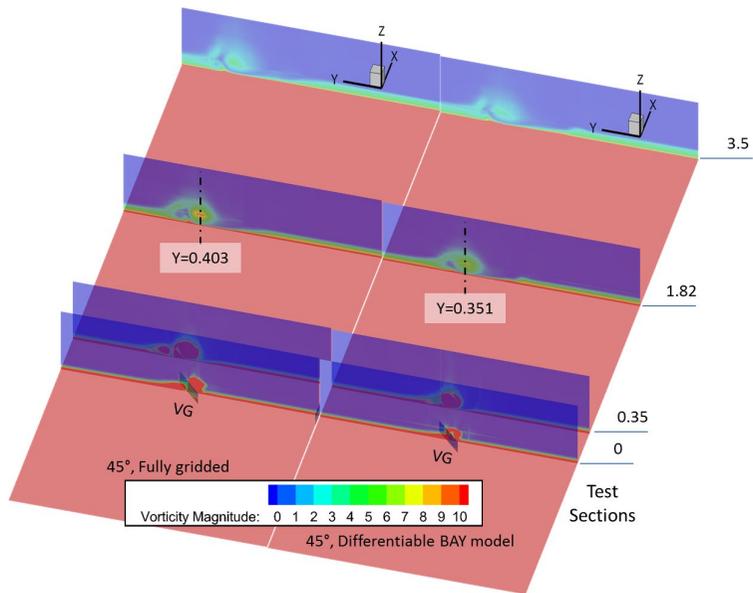


Figure B-4 (c) Vorticity contour ($\alpha_{VG}=45^\circ$).

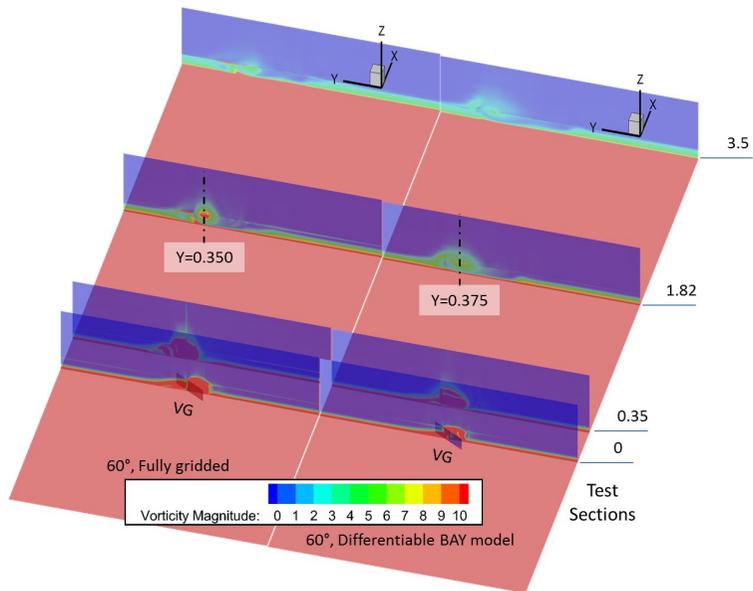


Figure B-4 (d) Vorticity contour ($\alpha_{VG}=60^\circ$).

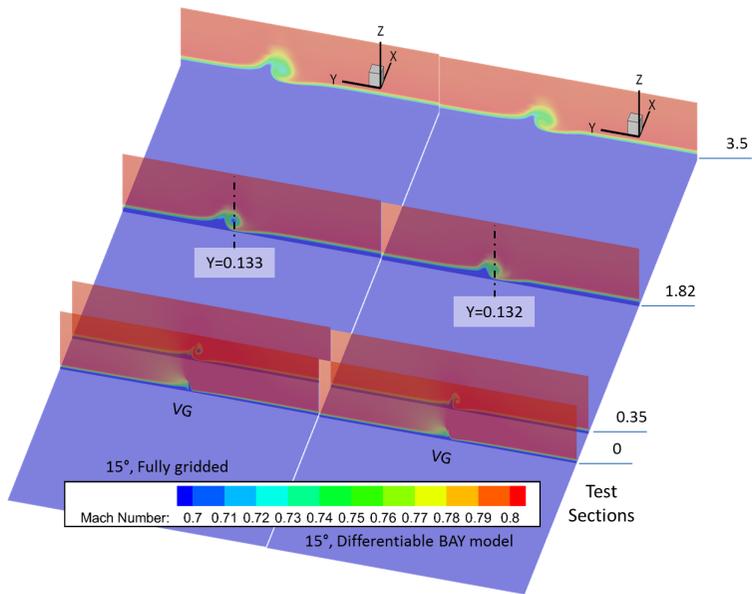


Figure B-5 (a) Mach number contour ($\alpha_{VG}=15^\circ$).

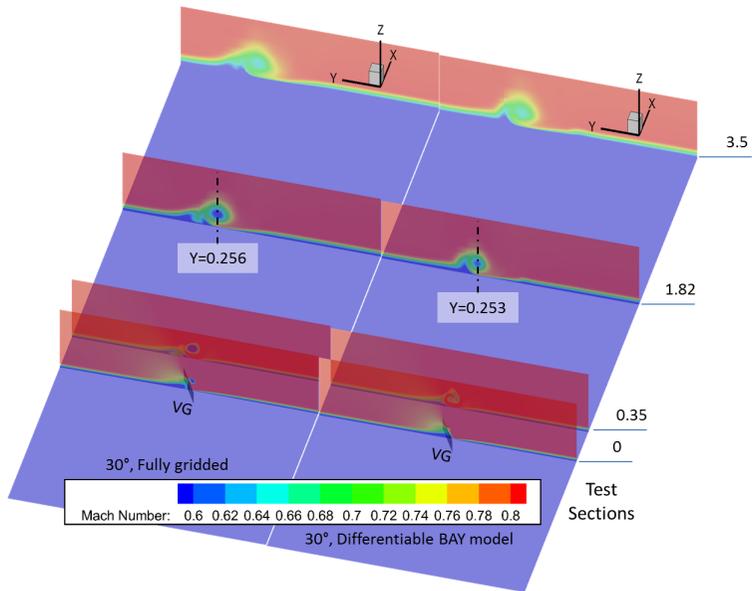


Figure B-5 (b) Mach number contour ($\alpha_{VG}=30^\circ$).

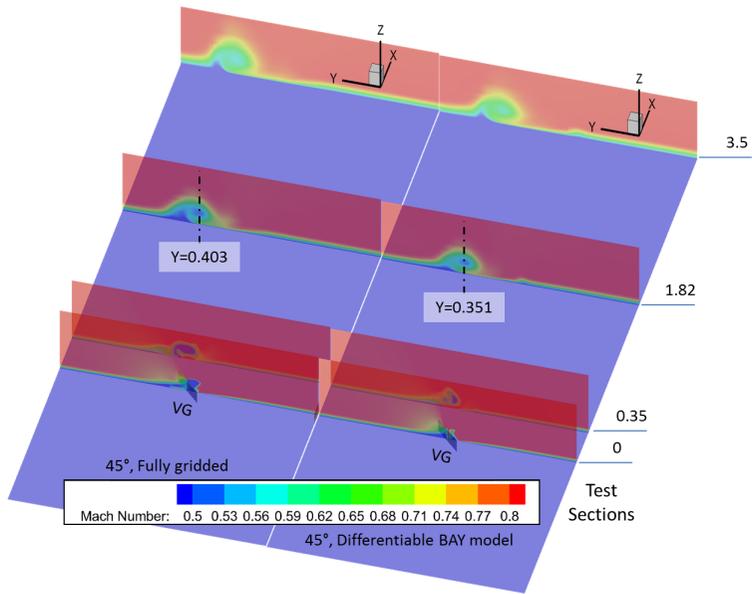


Figure B-5 (c) Mach number contour ($\alpha_{VG}=45^\circ$).

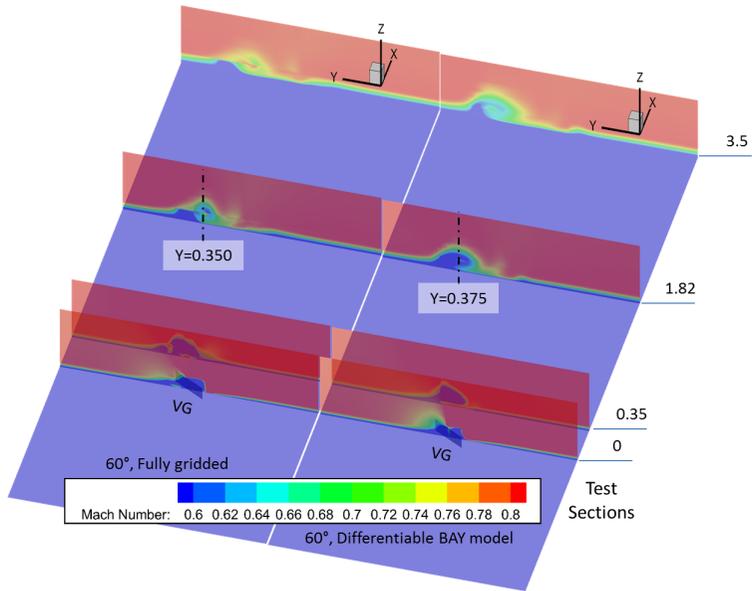
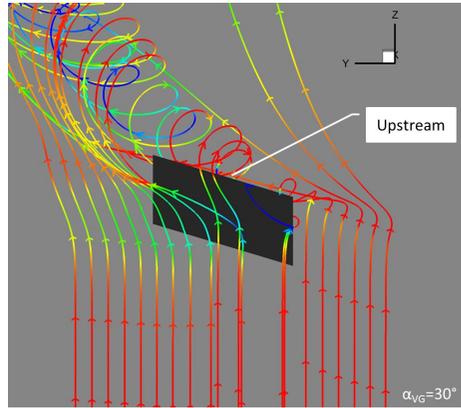
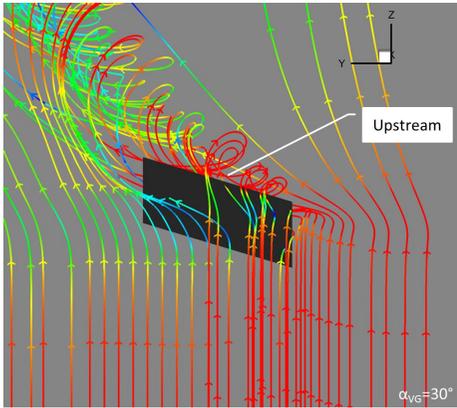


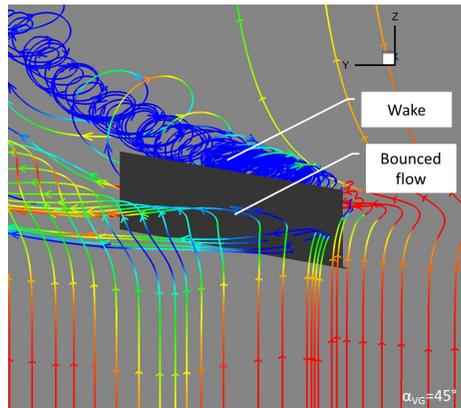
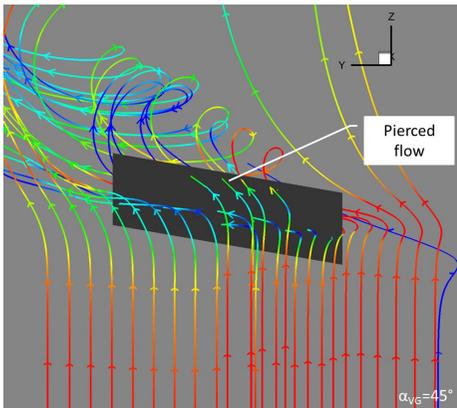
Figure B-5 (d) Mach number contour ($\alpha_{VG}=60^\circ$).



(a) Fully gridded

(b) Differentiable BAY model

Figure B-6 Local flow pattern ($\alpha_{VG}=30^\circ$).



(a) Fully gridded

(b) Differentiable BAY model

Figure B-7 Local flow pattern ($\alpha_{VG}=45^\circ$).

This page is blank

국문 초록

본 논문에서는 항공기의 성능을 향상시키기 위하여 매개변수법 기반의 와류 발생 장치 설계 연구를 수행하였다. 항공기의 많은 요소 중 S-형태의 흡입구인 RAE M2129 S-덕트와 동체-날개를 포함하는 항공기 외부 형상인 DLR-F6를 주요 고려 대상으로 선택하였다. S-덕트의 경우 내부 유동을, DLR-F6의 경우 외부유동을 각각 고려해야 하며, 이는 서로 간에 다른 특성을 보이므로, 두 경우에 대한 설계를 각각 수행하여 본 연구에서 제안하는 설계 연구의 강건성을 확인하였다. 고려 부품들의 성능을 향상시키기 위하여 S-덕트 내부에 11개의 와류 발생 장치를 설치하였으며, 날개 윗면에 여러 개의 와류 발생 장치를 개별적으로 설치하였다. 이 때, 설치된 와류 발생 장치의 최적 위치 및 형상은 각각의 와류 발생 장치를 독립적으로 고려할 경우에만 선정 가능하다는 어려움이 존재한다.

유동 해석 및 설계 시 와류 발생 장치의 설치를 직접적으로 고려할 경우 많은 계산시간이 소요되므로, 본 연구에서는 소스팀 모델 중 하나인 BAY 모델을 선정 및 적용하였다. 하지만 BAY 모델은 와류 발생 장치가 극소량 이동하게 될 경우 그 모사에 어려움을 가지고 있으며, 이는 이후 설계에 적용될 민감도 해석에 어려움을 야기한다. 이를 극복하기 위하여 미분이 가능한 BAY 모델을 개발 및 설계 연구에 적용하였다.

위에서 언급한 바와 같이, 와류 발생 장치는 독립적으로 고려하여야만 하며, 이는 많은 설계 변수가 필요하다는 의미로 귀결된다. 이러한 제약을 고려하여, 본 연구에서는 설계 변수의 개수와 계산 소요 시간이 서로 독립적인 매개변수법을 활용하여 기울기 기반의 설계 방법을 적용하였다.

또한, 개발된 미분 가능한 BAY 모델을 매개변수법에 적용하여 민감도 해석을 수행하였으며, 이러한 방식은 본 연구에서 제안하는 새로운 설계 방법이다.

RAE M2129 설계 연구의 경우, 엔진 입구에서의 유동의 찌그러짐 정도(distortion)를 최소화 하는 것을 목적으로 하였으며, 설계중에 전 압력 손실량이 늘어나지 않도록 하였다. 총 다섯 케이스의 설계연구를 수행하였으며, 이를 통하여 제안된 설계 방법의 검증, 최적화된 와류 발생 장치 획득, 개선된 성능 확인이 가능하였다. 본 설계를 통하여 S-덕트 내부 유동이 대체로 균일해졌으며, distortion 계수가 70% 이상 감소하였다.

DLR-F6 설계 연구의 경우, 항공기의 양항비를 증가시키기 위하여 파라메트릭 연구와 설계 연구를 동시에 수행하였다. 총 아홉 케이스의 파라메트릭 연구를 통하여 와류 발생 장치와 junction 와류의 상관 관계 및 유동 특성을 파악하였으며, 설계 연구의 baseline을 마련하였다. 이러한 파라메트릭 연구를 통해 설치된 와류 발생 장치는 DLR-F6의 성능이 2~4% 증가하는 효과를 가져왔다. 또한, 와류 발생 장치의 설계 수행을 통하여 junction 와류의 크기와 세기가 감소하는 것을 확인하였으며, 최종적으로 5% 이상의 성능이 증가하는 것을 확인하였다. 이 결과는 특히 항공기의 무게를 증가시킬 가능성이 있는 추가 부품 없이 이끌어낸 결과이므로 더욱 의미가 크다.

주요어: 전산 유체 역학, 공력 최적 설계, 매개변수법, 와류 발생 장치,
BAY 모델, RAE M2129 S-형태의 아음속 흡입구, DLR-F6
동체-날개를 포함하는 항공기

학 번: 2006-20974

이 름: 이 준 석